Terahertz spectroscopy of HgCdTe - and InAs/GaSb - based heterostructures

Mikhail Fadeev

THÈSE POUR OBTENIR LE GRADE DE DOCTEUR DE L'UNIVERSITÉ DE MONTPELLIER

En Physique

École doctorale : Information Structure Système

Unité de recherche Laboratoire Charles Coulumb

En partenariat international avec [IPM RAS, Russie]

Spectroscopie Terahertz d'heterostructures a base de HgCdTe et de InAs/GaSb

Présentée par Mikhail FADEEV

Le 17 décembre 2020

Sous la direction de Frédéric TEPPE et Sergey MOROZOV

Devant le jury composé de

Jérôme TIGNON, Professeur, LP Ecole Normale Supérieure	Rappoteur
Alexander ANDRIANOV, Chercheur de premier plan, Institut physico-technique Ioffe	Rappoteur
Dmitry KHOKHLOV, Professeur, Universite d'Etat de Moscou	Examinateur
Isabelle PHILIP, Directeur de Recherche, L2C Université de Montpellier	Examinateur
Alexei BARANOV, Directeur de Recherche, IES Université de Montpellier	Examinateur
Benoit JOUAULT, Directeur de Recherche, L2C Université de Montpellier	Invité
Frédéric TEPPE, Directeur de Recherche, L2C Université Montpellier	Directeur
Sergey MOROZOV, Professeur, Institut de physique des microstructures N. Novgorod	CoDirecteur

UNIVERSITÉ DE MONTPELLIER

Acknowledgments

It would not have been possible to write this Ph.D. thesis without the support of the great community of friends and colleagues as well as number people without whos none of the scientific work would be possible.

First, I would like to thank my supervisors, Dr. Frederic Teppe and Dr. Sergey V. Morozov for accepting me as their student and dedicating their time to share a bit of their experience and knowledge. I am especially grateful to Sergey for his personal and caring attitude and honest and Frederic for his patience and deep involvement during the hardest times of my scholarship.

I am very thankful to fellowship of my colleagues both in Laboratoire Charles Coulomb: Dr. Christophe Consejo, Prof. Wojciech Knap, Dr. Benoit Jouault, Dr. Dominique Coquillat, Sebatian Gebert, Dr. Nina Dyakonova and Prof. Mikhail Dyakonov and Institute for Physics of Microstructures:, Dr. Alexander Dubinov, Dr. Maksim Zholudev, Dr. Kirill Maremyanin, Prof. Vladimir Aleshkin, Dr. Konstantin Kudryavtsev, Dr. Dmitriy Kozlov, Vladimir Utochkin, Dr Leonid Bovkun and Dr Alexander Kadykov for providing healthy and productive environment. My cordinal gratitude belongs to Prof. Vladimir Gavrilenko for his wisdom, Dr. Sandra Ruffenach for her patience, Dr. Vladimir Rumyantsev and Dr. Sergey Krishtopenko for the valuable discussion and friendly advices. I additionally acknowledge Dr. Sergey Krishtopenko and Prof. Vladimir Aleshkin who carried out the theoretical calculations of band structure of the studied samples.

As any other experimental work, my project would be hardly possible without the high-quality samples, so I am grateful to be able to work with the master-hands of growth technology from the groups of Dr. Nikolai Mikhailov and Prof. Sergey A. Dvoretskii from ISP SB RAS (Novosibirsk, Russia) and Eric Tournié from Institut d'Electronique et des Systèmes (Montpellier, France).

It is my pleasure to thank all jury members: Jérôme Tignon, Alexander Andrianov, Dmitry Khokhlov, Isabelle Philip, Alexei Baranov, Benoit Jouault, for the acceptance to review this thesis.

I would like to acknowledge the financial, academic and technical support of the Institute for Physics of Microstructures RAS and its staff in Department for physics of semiconductors. I am most grateful to Russian Academy of Sciences and Russian Foundation for Basic Research for the financial support in Russia. I am very thankful the French Embassy in Moscow and Campus France provided me with the necessary financial support for this research in Laboratoire Charles Coulomb as well as for their kind and valuable advices at every stages of my scholarship.

Finally, I would like to thank my family, friends and fellow students for their support and encouragement.

Annotation

This thesis presents the studies of the band structure and optical properties of narrow-gap heterostructures with HgTe/HgCdTe and broken-gap AIb/InAs/GaSb/AlSb quantum wells (QWs). A unique property of these solid-state systems is high sensitivity of their band structure to internal parameters, such as thickness and composition of the QWs. It allows changing the band structure from normal to inverted inducing topological phase transition from trivial band insulator to quantum spin Hall insulator (QSHI). One of the most remarkable features of QSHI is its unique transport properties, expressed by the current being transmitted via spin-polarized one-dimensional edge channels with quantized conductance.

Transport properties of QSHI are of great scientific interest regarding fundamental effects as well as practical applications. Edge channels can be used for the dissipationless current transfer, resistance standards, in spintronics and quantum computing. Topological insulator states have been observed both in HgTe/HgCdTe and InAs/GaSb quantum wells structures. However, in both cases, further application of the amazing physical properties of these systems is limited by their low bandgap energy.

In the first part of this Ph.D. project, we present experimental studies of innovative QW geometry on the basis of trilayer InAs/GaSb/InAs structures. The results of magnetoabsorption and photoluminescence spectroscopy show that new geometry increases the bandgap compared to bilayer InAs/GaSb QWs. We also confirm the theoretical prediction that trilayer design can be combined with strained QW layers to amplify the value of inverted bandgap. Presented results prove that InAs/GaSb/InAs can be a basis for QSHI with a large bulk band-gap and pave the way towards ultimately plausible high-temperature topological conductivity.

We also investigate trilayer HgTe/CdHgTe/HgTe heterostructures with double QWs. In this system interaction between the states in two QWs results in rich topological behaviour. We show that the band structure of double HgTe QWs experiences multiple topological phase transitions driven by temperature. The first transition is similar to the one observed previously in single HgTe QWs. However, the second transition can lead to a formation of a novel phase, high order topological insulator.

Another property of HgTe/HgCdTe and AIb/InAs/GaSb/InAs/AlSb heterostructures which is realized in narrow gap structures is carrier dispersion mimicking that of relativistic particles. Energy-momentum conservation laws within quasirelativistic dispersion prohibit non-radiative Auger recombination, the main fundamental factor limiting the operation of interband radiation sources. Thus, the structures with quasirelativistic dispersion can be used for the development of solid-state sources of infrared radiation.

They are especially appealing in the wavelength range from 24 to 60 microns where A3B5–based unipolar quantum cascade lasers cannot operate due to high lattice absorption.

The goal of the second part of this Ph.D. project is to study the band structure and radiative properties of HgTe/CdTe based heterostructures with QWs and develop the physical foundation for the far-infrared semiconductor lasers. We present the results of emission from samples with Hg1-yCdyTe/Hg1-xCdxTe QWs and analyze their band structure in order to determine the most efficient designs for the amplification of long-wavelength radiation. We demonstrate that maximum suppression of Auger recombination is achieved in structures with thin HgTe QWs with zero cadmium concentration surrounded by HgCdTe barriers with 70% CdTe. Finally, we investigate the pumping parameters and show that the increase of the wavelength of optical excitation improves the characteristics of stimulated emission. These results demonstrate the potential of HgTe/CdHgTe heterostructures as a basis for far-infrared and terahertz sources.

Résumé

Ce travail de thèse concerne l'étude de la structure de bandes et des propriétés optiques d'hétérostructures à faibles gaps, à base de puits quantiques (QWs) de HgTe/HgCdTe et de AlSb/InAs/GaSb/AlSb. Leur structure de bandes peut passer d'un ordre normal à un ordre inversé, induisant une transition de phase topologique d'un isolant trivial à un isolant topologique. L'une des caractéristiques les plus remarquables de ces isolants topologiques est leurs propriétés de transport uniques, dues à des canaux de bord unidimensionnels polarisés en spin ayant une conductance quantifiée. Ces propriétés de transport sont d'un grand intérêt autant du point de vue fondamental qu'appliqué. Or, la phase isolant topologique a été observée à la fois dans des puits quantiques de HgTe/HgCdTe et dans InAs/GaSb. Cependant, dans les deux cas, l'utilisation des propriétés physiques étonnantes de ces systèmes est limitée par leur faible énergie de bande interdite.

Nous présentons l'étude expérimentale de puits quantiques de géométrie innovante, à base de triples couches InAs/GaSb/InAs. Les résultats de spectroscopie par magnéto-absorption et par photoluminescence montrent que la nouvelle géométrie de puits accroît la bande interdite comparativement aux bicouches InAs/GaSb. Nous confirmons également la prédiction théorique selon laquelle la conception de ces triples couches peut être combinée avec un effet de contrainte pour amplifier la valeur du gap inversé. Les résultats présentés prouvent que InAs/GaSb/InAs a en effet un grand gap inversé, ce qui rend plausible l'observation à terme de l'effet Hall quantique de spin à haute température.

Des hétérostructures tri-couches HgTe/CdHgTe/HgTe formant un double puits quantique sont ensuite présentées. Dans cet autre système, l'interaction entre les états de deux puits se traduit par un riche diagramme de phase topologique. Nous montrons spécifiquement que la structure de bandes des puits doubles de HgTe subit plusieurs transitions de phase topologiques induites par la température. La première transition est similaire à celle observée auparavant dans des puits simples. La seconde transition pourrait conduire à la formation d'un nouvel état topologique d'ordre plus élevé.

Une autre propriété des hétérostructures HgTe/HgCdTe et Alb/InAs/GaSb/InAs/AlSb de faibles gaps repose sur la dispersion des porteurs de charges imitant celle des particules relativistes. La loi de conservation de la quantité d'énergie dans les systèmes relativistes interdit la recombinaison Auger non radiative, c'est-à-dire le facteur fondamental limitant le fonctionnement des sources de rayonnement inter-bandes. Ainsi, les hétérostructures à dispersions relativistes peuvent être utilisées pour le développement de sources pour l'infrarouge moyen et lointain à base de semi-conducteurs. Ils sont particulièrement intéressants dans la gamme 24-60 microns où les lasers à cascades quantiques unipolaires à base de semi-conducteurs A3B5 ne peuvent pas fonctionner en raison de l'absorption élevée du réseau cristallin.

L'objectif de la deuxième partie de ce travail de doctorat est donc d'étudier la structure de bandes et les propriétés radiatives des hétérostructures à base de HgTe/CdTe et de développer les bases physiques des lasers à semi-conducteurs pour le THz. Des résultats d'émission de plusieurs échantillons sont présentés et leur structure de bandes est analysée dans le but de déterminer la structure optimale permettant l'amplification du rayonnement THz. Nous démontrons que la suppression de la recombinaison Auger est obtenue dans des puits minces de HgTe ayant une concentration de cadmium nulle, entourés de barrières HgCdTe avec 70% de CdTe. Enfin, les paramètres de pompage optique sont étudiés et nous affirmons que l'augmentation de la longueur d'onde d'excitation améliore les caractéristiques de l'émission stimulée. Ces résultats démontrent le potentiel des hétérostructures HgTe/CdHgTe entant que sources infrarouge lointain et THz.

Table of contents

Acronyms and glossary

ADC	Analog-to-digital converter
AR	Auger recombination
BG	Bilayer graphene
BI	Band insulator
CQW	Composite quantum well
CR	Cyclotron resonance
CT	Critical temperature
DI	Double inverted (phase)
IR	Infrared
LL	Landau level
MA	Magnetoabsorption
MBE	Molecular beam epitaxy
MCT	Mercury-cadmium telluride
MF	Magnetic field
ML	Monolayer
PC	Photoconductivity
PL	Photoluminescence
QCL	Quantum cascade laser
QHE	Quantum Hall effect
QI	Quenching intensity
QSHE	Quantum Spin Hall Effect
QSHI	Quantum spin Hall insulator
QW	Quantum well

SE	Stimulated emission
SQUID	Superconducting Quantum Interference Device
TI	Topological insulator
TQW	Triple quantum well
Tr	Transmission
VTI	Variable temperature inset

List of figures

List of Tables

Introduction

1.1 Topology and physics

Topology is a field of mathematics studying the properties that are preserved through deformations, twisting, and stretching of objects. It is dealing with the most general properties of shapes, such as continuityand connectedness. Topology is based on the general concepts of neighbourhood, open sets and does not require metric space, which means that the distance between the points is not relevant. This domain of geometry seems to be quite far from the physics which deals with material objects; however, it did not prevent the emerging and expansion of the field of topological physics. The importance of this field of science is justified by the unique properties possessed by topologically non-trivial states of matter, as well as their prospects in both the applied technology and fundamental physics.

At this point we are going forward too fast. In fact, the physicists had been dealing with the topological phenomena long before the discovery of the topological insulators and even the semiconductors at all. One of the good examples is the Gauss's flux theorem:

$$\Phi = q/\varepsilon$$

The basic idea of the flux theorem is that the net electric flux Φ through any hypothetical closed surface is determined byelectric charge within that closed surface.

$$\oint \vec{D} d\vec{s} = \int \rho dV$$

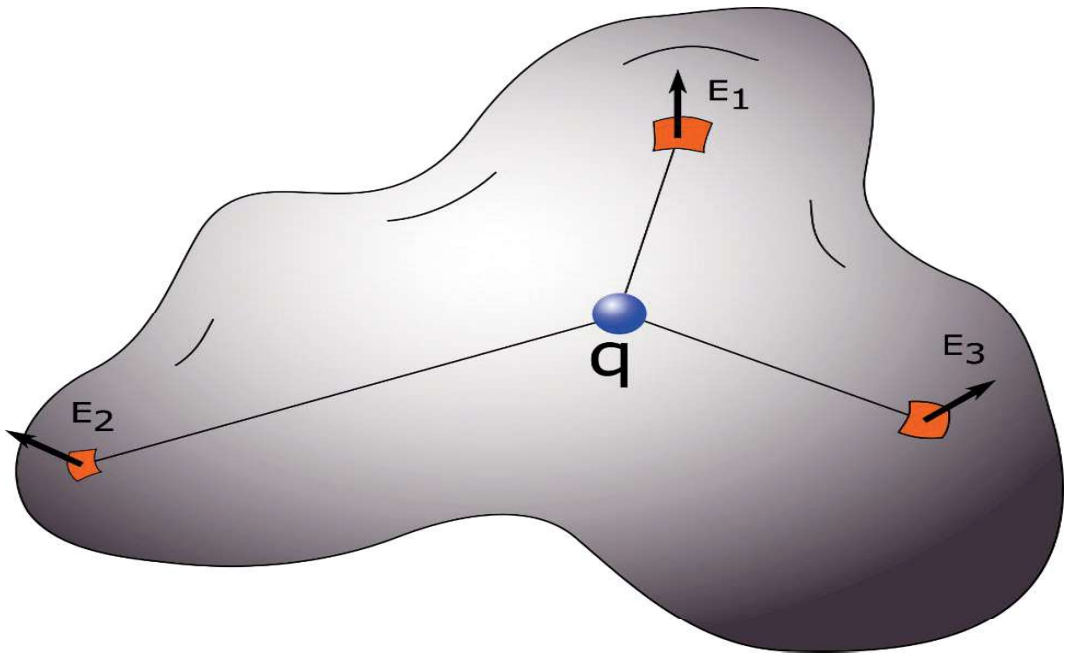

Fig. 1. Schematic illustration of Gauss flux theorem

Putting aside the relation of the theorem to the electromagnetism, it becomes clear that the Gauss theorem is essentially topological. If we attribute the flux to the properties of the surface, the only required condition is the “closeness” in its topological meaning. Considering the flux through the surface, its value will not change upon any continuous deformations of the surface itself, unless the charge inside the volume covered by the surface is changed. Moreover, in such a familiar model one can pick out another important topological phenomenon: bulk-boundary correspondence. It yields that a certain property of the surface is determined by the volume limited by such surface.

Similar effects are present in all the areas of modern physics in a form of continuity equation or flux theorem, starting from the dynamics of liquids to quantum physics and general relativity. And as we can see, topology in physics is not an uncommon thing. And because scientists had in fact been tackling topological effects since times immemorial, one may ask what is so special about the relation of topology and condensed matter systems.

1.2 Topology in condensed matter systems

Condensed matter physics deals with the behaviour of particles at finite density and at low temperatures, where, depending on factors such as applied pressure, doping, spin of the particles, etc., matter can reorganize itself in different phases. Classically, we learn of phases such as liquid, crystal, or vapour, but the quantum world holds many more fascinating mysteries. Quantum theory predicts the existence of myriad states of matter, such as superconductors, charge density waves, Bose-Einstein condensates, ferromagnets and antiferromagnets, and many others .In all these states, the underlying principle for characterizing the state is that of symmetry breaking, which is described within the Landau theory.

1.2.1. Landau phase transition theory

Landau phase transition theory introduced in 1937 by L. Landau[1] is a general phenomenological tool for classification and description of phases and transitions between them. A solid state body can be characterized by a general function of probability density ($\rho(x,y,z)$), which denotes the probability of finding an atom in location with coordinates {x,y,z}. For amorphous bodies and liquids the distribution of atoms is isotropic and homogenous (ρ = const). This property separates them from the crystals for which atoms are arranged in a highly ordered periodic structure, crystal lattice. The symmetry of the crystal lattice determines the physical properties of the crystal.

One of the basic properties of phase transitions in condensed matter systems is that such phase transition cannot occur continuously. Each state of the body can be attributed to one of the phases based on its symmetry (compare that to phase transition between gas and liquid, which become indistinguishable above the critical point in pressure-temperature diagram).

Landau theory is based on the general assumptions that the free energy of a system (F) is an analytic function of the internal parameters of the body (order parameter) and obeys the symmetry of the Hamiltonian. The latter means that even small continuous deformation of the function $\rho(x,y,z)$ causes abrupt changes in thermodynamic properties of the body

$$\rho \to \rho_0 + \delta\rho$$

Where ρ and ρ_0 are the probability density functions below and above the point of phase transition respectively. The small increase can have lower symmetry than the initial function and as the sum of two functions has the symmetry equal to the lowest of two, the changes in thermodynamic potentials such as F are experiencing abrupt changes.

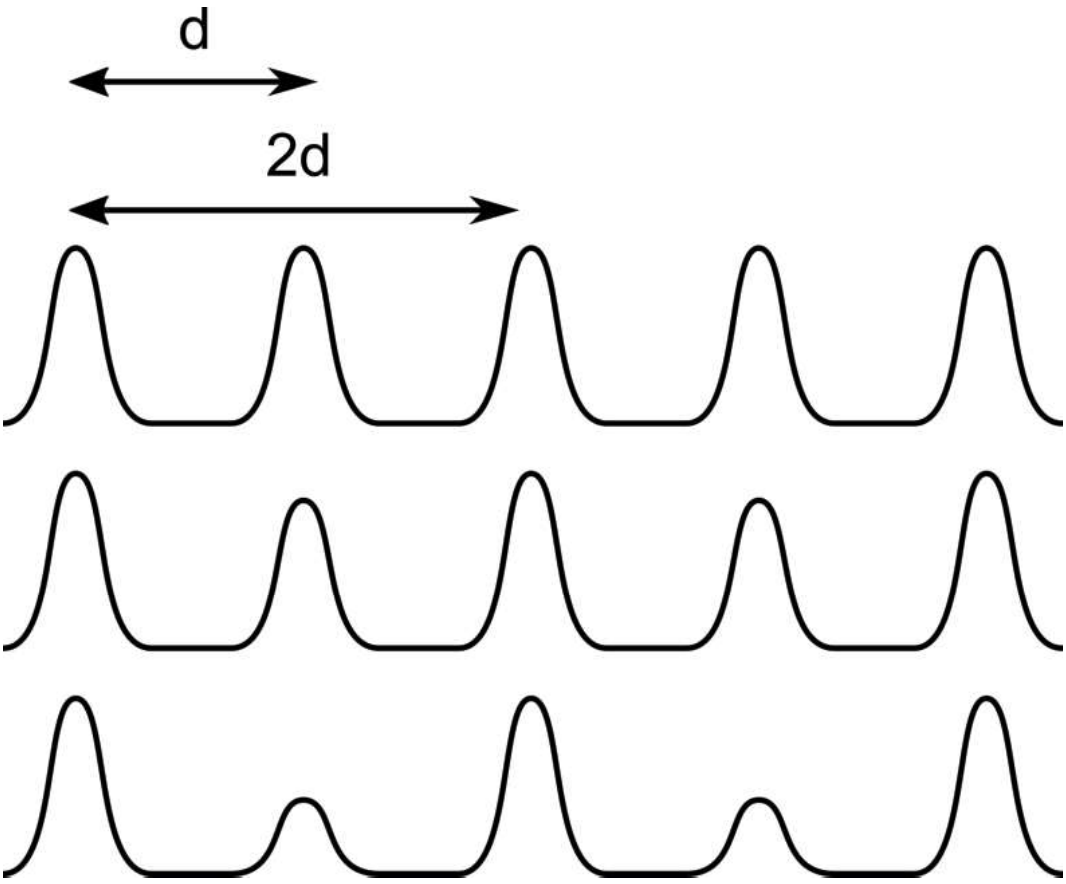

Fig. 2. The changes in symmetry of the probability density ρ by the small variation $\delta\rho$

Quantitative characterization of structural changes of a body when passing through the point of phase transition can be performed by introducing the order parameter, the variable that has nonzero value in one (unsymmetrical) phase and zero in the other (symmetrical) phase.

An order parameter with observable consequences acquires an expectation finite value in the state of matter studied and differentiates it from others. In this theory, a high-temperature symmetric phase experiences a phase transition to a low-temperature, less-symmetric, symmetry-broken state (It should be noted that this is not the universal law and there are examples of the opposite situation).

The theory has very general premises, such as the possibility of expansion of the free energy in the order parameter when close to a phase transition, this is likely to be possible because the order parameter is small. The transition can be first, second, or higher order, depending on the vanishing of the coefficient of the second, third, or higher coefficient of the expansion of the free energy in the order parameter.

At the same time, symmetry breaking is not limited to the position of the atoms in the crystal lattice and can be caused by the internal currents. For example, a ferromagnet has an overall magnetization, which breaks the rotational symmetry of the spin and picks a particular direction of the north pole. An antiferromagnet does not have an overall magnetization but develops a staggered-order parameter at some finite wavevector. Landau's theory of phase transitions provides the phenomenological footing on which all of different symmetry-broken states can be explained.

However, the major limitation of Landau's theory of phase transitions is that it is related to a *local* order parameter whereas in the past few decades it became clear that a series of phases of matter with so-called topological order cannot be described by the local order parameter.

1.2.2. Topological phase transitions

Topologically non-trivial systems appear when for the ensemble of the particles (usually one- or two dimensional) the interaction between them decays with distance slower than the number of interacting particles. As a result, in certain conditions one deals with a special state of matter which is regulated by the long-range quantum entanglement [2] meaning that the system is not sensitive to the local pertubations. For such systems Landau theory is not applicable because different phases have the same symmetry, suggesting that they are regulated by the new type of topological order. To properly classify such systems one needs to consider the topological invariants which describe different ground states. Connection to topology here is determined by the underlying physics and its corresponding energetic while a phase transition can be thought of as a transition between topological sectors defined by the topological invariants [3].

Topology and phase transitions in condensed matter physics were first linked by the works of Berezinski [4], and Kosterlitz and Thouless [5] for the study of topological phases of matter. It is worth highlighting that a Nobel Prize in Physics in the year 2016 was divided - one half was awarded to David J. Thouless, the other half jointly to F. Duncan, M. Haldane, and J. M. Kosterlitz for theoretical discoveries of topological phase transitions and topological phases of matter.

Recently, topological phases have been pursued because of their potential practical applications: it has been proposed that a topological quantum computer could employ the 2-D quasi-particles of non-Abelian FQH states (called non-Abelian anyons), whose world lines cross over one another to form braids[6]. These braids form the logic gates that make up the computer. A major advantage of a

topological quantum computer over one using trapped quantum particles is that the former encodes information non locally and hence is less susceptible to local decoherence processes [6,7]

To understand a little more this notion of topological phase transitions in solids, let us go back to some basic ideas. First of all, topology is a part of mathematics that classifies objects not as a function of their symmetry properties but as a function of their intrinsic properties. These properties can be their number of holes, or the number of windings needed to get back to the initial point of the surface (Ex. The Mobius strip). During a smooth and continuous transformation of the object (as long as the object isn't broken or torn), this number is therefore conserved. This number is in fact connected to the total curvature of its surface, as described in the Gauss-Bonnet theorem. On a non-trivial topological surface, due to its total curvature, it exists indeed a geometrical phase or an angular mismatch in the parallel transport, which is linked to the topological invariant of the object (Considering the total curvature of the Earth, a traveller will face an angular mismatch in the parallel transport when looping from the north pole to the equator). These notions of total curvature and angular mismatch or geometrical phase can be extended to many different physical systems.

In quantum mechanics for instance, just like in the Mobius strip example or in the Foucault pendulum experiment, the wave function of a quantum system may not return to its original phase after its parameters cycle around a closed loop in the parameter space. This geometrical phase is in this case known as the Berry phase. In condensed matter physics, the Bloch wave function of the occupied band in a crystal may not return to its original phase after its parameters cycle around the Brillouin zone. The physical property we are following in this case is not the position on a path around a curved surface in real space, but the evolution of the parity of the Bloch wave function around the Brillouin zone.

In first approximation, without considering crystalline symmetry arguments, in a non-trivial topological system there exists a singularity (just like the twist of a Mobius strip) of the parity of the Bloch wave function around the high symmetry points of the Brillouin zone. This angular mismatch in the parallel transport of the parity of the wave function is associated with the Berry curvature and the topological invariant of the system. The key point is that there is no other way to induce a singularity of the parity of the Bloch wave function around the Brillouin zone than to have a band inversion. That's the reason why materials with inverted band structures have been extremely sought after in recent years by chemists and condensed matter physicists.

1.3 Topological insulators

One of the reasons, why topological insulators (TIs) are attract the interest of the scientists is that contrary to other topologically classified states of matter they in principle do not require ultra-low temperatures and ultra-high magnetic fields for their formation. As a result, the properties of TIs can

be observed in rather common materials. The first proposal of a “Quantum Hall Effect without Landau Levels” in grapheme dates back to the paper by Haldane [8]. Further development this idea found in two papers by Kane and Mele [9,10] who generalized the scheme for identifying topological index (the Z_2 index), introduced the term “topological insulator” and predicted the emergence of topologically protected edge states in a model of graphene with spin-orbit interaction. This new type of quantum Hall edge states without magnetic fields was called the quantum spin Hall effect (QSHE) [11]. An alternative approach to topological insulators was simultaneously developed by Bernevig, Hughes and Zhang (BHZ) and presented in Ref.[12]. Their model was based on another material system – HgTe/CdHgTe QWs. HgTe is characterized by large spin-orbit coupling, leading to an inversion of Γ6 and Γ8-bands while the band structure of narrow HgTe/CdHgTe QWs can be described by simplified model similar to graphene. It turned out that proposed system was not only convenient for the modeling, but also lead to fruitful experimental results. Shortly after, the Molenkamp group in Würzburg indeed observed quantized edge-state conduction without magnetic field in a CdTe/HgTe/CdTe quantum well [13] as predicted for a 2D TI. In a subsequent experiment, the spin-polarization of these edge states was measured confirming their topological character [14].

After these initial findings, the hunt for other topological materials started. In particular, the prediction of 3D TIs – 3D bulk insulators with conductive topological surface states cf. Kane, Fu and Mele, Ref. [15], led to considerable research effort in this direction, see Ref. [16] for a review. In this context, $Bi_{1-x}Sb_x$, Bi_2Se_3, Bi_2Te_3 and Sb_2Te_3 were proposed by Zhang et al. [17] and confirmed in several ARPES measurements. In 2011, the Würzburg group demonstrated that thicker (~ 100 nm) layers of (strained) HgTe are also 3D TIs [18].

The essential consequence of a nontrivial topology of valence bands in an insulator is the appearance of metallic edge states at its surface, with a linear relativistic dispersion relation. It is these surface states that are probed experimentally when testing the topological nature of a semiconductor, and which give rise to all physical properties of these materials. The continuous description of the interface between two insulators amounts to continuously deform the bulk eigenstates of one into the other. If one of the two insulators is topological this is not possible for the ensemble of valence band eigenstates by definition of the topological nature of the twist. Extrapolation of wave functions from both sides requires closing the gap: a smooth connection is then always possible as a consequence of the triviality of the Bloch bundle. Another more practical point of view consists in recalling that the Z_2 topological order can be identified with the band inversion at one of the λ_i TRIM point of the Brillouin zone with respect to the “standard ordering" of atomic orbitals constituting bands in a standard insulator. Hence at the interface between two such insulators, the two corresponding bands have to be flipped back from the inverted to the normal ordering. When doing so, they necessarily give rise to energy bands within the gap and located at the interface, corresponding to edge or surface states.

Moreover, the crossing of two such bands can be described at low energy by a linear dispersion relation, associated with a relativistic Dirac equation of electron propagation.

1.3.1 Concept of quantum spin Hall insulator state

The discovery of a quantum spin Hall insulator (QSHI) state in Hg/HgCdTe quantum wells [19] was the first experimental demonstration of topological insulator state. It manifested the emergence of new field of physics devoted to topological properties of the matter. One of the most remarkable features of QSHI is its unusual transport properties, arising because the current is transmitted via spin-polarized one-dimensional edge channels. From this perspective, QSHI resembles to the quantum Hall effect (QHE).

In order to observe QHE a strong magnetic field is applied to semiconductor structure which hosts 2-dimentional electron gas (i.e. a QW or a field-effect transistor) which leads to quantisation of the electron spectrum and formation of the insulating gap in a bulk of the crystal [20]. At the same time, magnetic field leads to formation of one-dimensional metallic channels on the edges of the sample. Thus, when the voltage is applied the current can flow only through the edges of the sample. Analogously, in QSHI the bulk of the structure is insulating and the current flows through one-dimensional edge channels, one of the differences being that these channels are an intrinsic property of the material and do not require magnetic field for their formation.

In both cases edge channels have quantized conductance, which is the consequence of the finite number of states each one-dimensional channel can support. In the QHE regime the edge channels are chiral which means that the flow of the current is governed by the direction of the magnetic field. Time-reversal-invariant nature of the edge channels in QSHI makes a formation of a single chiral channel impossible, thus the edge channels of QSHI come in pairs and are helical, which means that the electrons of opposite spins propagate in the opposite directions. This property of topological edge channels, also called helicity prevents the electrons from elastic backscattering on non magnetic impurities, as it was shown in Ref. [9,12,21].

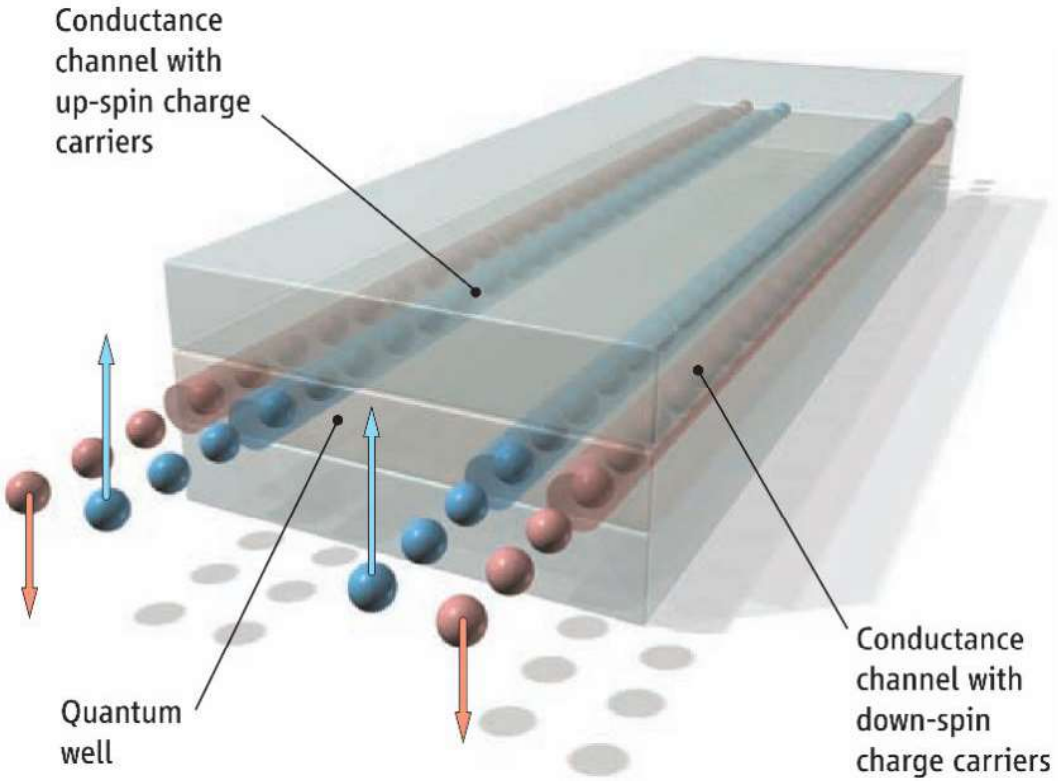

Fig. 3. Schematic representation of spin-polarised edge channels in two-dimensional topological insulator. The picture is taken from [19].

In order to detect and study the edge channels in QSHI one needs to separate their conductivity from the conductivity of the bulk material. This is challenging task as it requires the bulk to be fully resistant, or at least have much smaller conductivity than the edge channels. In fact, when semiconductor is in the QSHI regime it has a gap in the bulk band spectrum, however, this alone does not ensure the insulating properties of the material. This is a noteworthy difference from QHE for which high resistivity of the bulk material is ensured by geometrical quantization of carriers in magnetic field.

1.3.2 Materials for quantum spin Hall effect

Despite the numerous theoretical papers on the topic of two-dimensional topological insulators, experimental properties of such systems remain very little studied. So far, even the existence of the edge channels was demonstrated in fact only in two non-exotic systems: HgTe/HgCdTe quantum wells (QWs) [19] and composite quantum wells (CQWs) InAs/GaSb/AlSb [22]. This is due to the fact that for experimental studies of the edge channels, their contribution to the total conductivity of the system should be dominant (much higher than the conductivity of the two-dimensional electron gas). In reality, the systems with inverted band structure required for the realisation of the QSHE have relatively small bandgap (up to 16 meV in HgTe QWs and up to 5 meV in InAs/GaSb CQWs). Small bandgap inevitably leads to high concentration of the charge carriers and significant fluctuations in their concentration. Consequently bulk of the structure has high conductivity and is split into so-called “charge puddles” – the areas of the sample with lower bandgap that trap the carriers and have higher

conductivity than the rest of the sample. As a result, the transport of the edge channels manifests itself only at cryogenic temperatures, lower than 1 K and in devices shorter than the spatial extent of fluctuations (distance between charge puddles) and length of the free path of the electron in respect to non-elastic phonon scattering. This hinders the possibility both of the experimental studies and practical applications of QSHIs that were demonstrated up to date.

Currently scientists search for new materials with larger bandgap which would allow the investigation of QSHIs at higher temperatures. As an example, the studies of compressively strained HgTe/CdTe QWs show that in such structures the bandgap can be increased up to 55 meV [23]. It is also worth mentioning the actively developing area of monolayer structures, one of the most remarkable results in this field is demonstration of edge transport in 1-T-WTe_2 monolayers at temperatures up to 100 K [24] and as it has been recently reported even at room temperature [25]. At the same time monolayer structures are unstable in the atmosphere due to oxidation and mechanical deformation and are yet weakly integrated in the modern semiconductor technology.

1.3.3 HgTe/HgCdTe QWs

As it was discussed in the introduction, the necessary condition for the formation of QSHI is the inverted band ordering. In the aforementioned HgTe/HgCdTe and InAs/GaSb heterostructures band inversion has different origins.

As single HgTe QWs will not be the aim of this PhD work, their description is briefly given in this chapter and more attention is paid to III-V-based QWs in the next sub-chapter.In HgTe QWs non-trivial band ordering directly results from the band inversion in HgTe, where strong spin-orbit coupling “pushes” the electronic band with P-symmetry above the band with S-symmetry. However, in spite of the inverted band order thick non-strained HgTe layers do not form QSHI state because the hole and electron subbands have equal energy at zero quasimomentum forming semi-metallic band spectrum (more accurate term to describe HgTe is zero gap semiconductor, as the valence and conduction bands do not overlap). In HgTe/HgCdTe QWs quantum confinement opens an inverted gap in the spectrum since CdTe is topologically trivial semiconductor. As a result, the mutual position of the first electron E1 and hole H1 subbands, which determines the nature of the topological phase, is regulated by the QW width. QWs wider than a critical value feature a band inversion and are in the QSHI state (**Fig. 4c**), while narrower QWs have band ordering similar to the CdTe and therefore are from the topological perspective, in the trivial band insulator state (**Fig. 4a**). The highest inverted bandgap, which can be achieved in non-strained HgCdTe QWs is limited by the side maxima of the valence band. This dispersion feature origins from the heavy hole subband of HgTe, therefore when the width of the QW increases, so does the energy of the side maxima and the band structure approaches that of bulk HgTe.

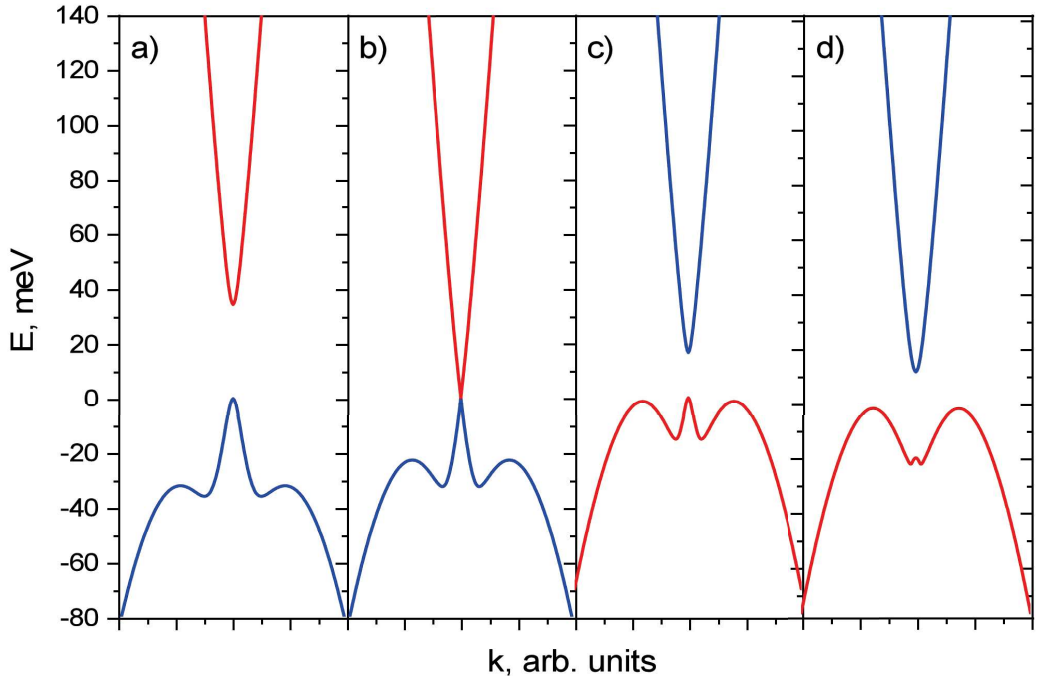

Fig. 4. First electron E_1 (red) and hole H_1 (blue) subbands of HgTe/$Hg_{0.35}Cd_{0.65}Te$ QWs of different widths. Panels a) - d) correspond to a) trivial band insulator, b) zero-gap Dirac semimetal, c) topological insulator with maximum inverted gap, d) topological insulator with indirect inverted gap.

For wide enough QWs the top of the valence band is determined by these maxima rather than the local maximum at Γ point (**Fig. 4d**). As a result, after a certain point increasing the QW width only shrinks the bandgap. Consequently, there is a maximal inverted bandgap achievable in classical tensile-strained HgTe QWs grown on CdTe amounting 16 meV (**Fig. 4c**), with a remark that it can reach 55 meV in compressively strained HgTe QWs [23] because compressive strain opens the gap in band spectrum of HgTe, and therefore lowers the energy of valence band side maxima. Additional factor which obstructs the observation of the QSHE in HgTe/CdHgTe QWs at high temperatures is a fast (≈0.3 meV/K) decrease of the inverted bandgap with temperature [26], which closes the bandgap of any structure at a certain temperature.

1.3.4 InAs/GaSb QWs

QSHI state was also predicted in InAs/GaSb CQW heterostructures soon after its experimental observation in HgTe QWs by Liu et.al. [27], but it took another three years before this prediction was experimentally demonstrated [22]. This delay can be attributed to the experimental difficulties originating from the properties of the InAs/GaSb CQWs. The subband inversion in InAs/GaSb bilayer QWs is caused by specific band-edge alignment of InAs and GaSb semiconductors arising at their interface [28,29]. InAs and GaSb form a broken gap (type II) heterostructure, where both electron and hole bands of InAs lie below those of GaSb. For thin InAs and GaSb layers, the dimensional quantization prevails over the band ordering of the bulk materials. In this case first electron-like subband of the CQW lies

above the hole like subband and structure has a trivial band ordering. With the increase of layer thickness, electron-like (E1) electron-like level shifts downwards while hole-like (H1) level rises in energy which can eventually lead to band structure inversion. Hereinafter, the electronic subbands have been classified as electron-like or hole-like levels by comparing the relative contribution to a level from the basis states of different bands at zero quasimomentum. The wave function in E_1 subband is mostly localized in the InAs layer, while that in the H_1 subband is mostly localized in the GaSb layer. In non-interacting QWs, when the mixing between the bands is absent, E_1 and H_1 levels are fully determined by the parameters of InAs and GaSb layers correspondingly.

During the first studies of InAs/GaSb superlattices the inverted regime was considered semimetalic with the subbands crossing at a certain quasimomentum [30]. Later studies showed that mixing between the levels in the different layers opens a small hybridisation gap [31]. The presence of the gap was then demonstrated experimentally by the groups of Yang et al. and Lakrimi et al. [29,32]. Considering the inverted-band gap in pure InAs/GaSb bilayers is just 3–4 meV [27], which makes the observation of the QSHI a much harder task compared to HgTe QWs.

Although the quantized edge conductance was indeed observed in InAs/GaSb heterostructures [33], there is the evidence that in the inverted regime residual carrier density in the bulk does not disappear even at the temperatures as low as 20 mK (see [34]). In the same paper [34], the authors showed that contribution of the edge channels to the total conductivity can be extracted from the experimental data even at considerable concentration of bulk carriers, but their evidence of QSHE state was unequivocal.

The origin of the non-zero current in the bulk material had been explained in a theoretical paper by Naveh and Laikhtman [35]. They concluded, that even a finite-level broadening due to the carrier scattering could result in non-zero conductivity, even when the temperature is effectively zero. The presence of the occupied states in a bulk spectrum not only complicates the experimental observation of the edge channels, but also leads to the coupling of the edge states from two sides of the sample, which creates the gap in the edge spectrum and allows backscattering of the electrons, introducing dissipation to the system [36].

Nevertheless, in 2011 I.Knez and R.R. Du managed to demonstrate the QSHI state by studying a set of InAs/GaSb samples with various dimensions and length/width ratios [22]. They were able to identify a contribution of the edge channel transport, and debated that edge modes in InAs/GaSb can persist alongside the conductive bulk because the scattering between different sates (edge and bulk) is suppressed due to strong decoupling between them. Decoupling is a natural result of the difference in the Fermi wavevectors between the edge states and the bulk carriers. Carriers occupying the edge states have zero Fermi vector, while carriers in the bulk of the structure which have dispersion similar

to non-hybridised case and their Fermi vector is close to crossing point of the bands. As a result, the scattering of the edge states is reduced and they still can be detected.

Summing up, the first experimental studies of InAs/GaSb CQWs showed that separation of the conductance of the edge states is a difficult task in this system because the resistance of the bulk tends to a finite value when lowering the temperature of the structure. This is a consequence of two factors. First, the bandgap on its own is small, so the thermal activation is present below cryogenic temperatures. Second, the hybridization of the bands responsible for the formation of the gap results from the non-locality of electron states in the growth direction of the wells, which can be destroyed by finite, but negligibly low scattering of the carriers[35]. This effect not only complicates the experiment, but has a negative impact on the transport properties of the edge channels.

In the following studies the problem of bulk conductivity was addressed in several ways. There are different approaches to lowering the conductivity of the bulk: either by decreasing the mobility of the carriers, or by decreasing the carrier concentration through increasing the bandgap or decreasing the .

The last approach was implemented in InAs/GaSb CQW heterostructures by Suzuki et al [37]. They studied a set of specially designed 6-terminal Hall bars. A distinguishing feature of thestructures was a δ-layer of beryllium placed inside the AlSb barrier in order to tune the position of the Fermi level in CQW closer to the bandgap. It was shown that the resistance of the sample demonstrated strong dependence on the thickness of the InAs layer, reaching 12 kOhm in samples with intermediate thickness, which corresponds to the theoretical prediction for the resistance of the edge channels in QSHI. At the same time, it is worth mentioning that such value was reached only in a part of the samples, which makes these results ambiguous.

Up to date, reduction of the mobility has proved to be the most effective tool to make the bulk of the structure fully resistant. An important property of the edge states is that the backscattering of the “edge” electrons on non-magnetic impurities is prohibited. Thus, the mobility of the two-dimensional electron gas can be reduced by introducing the disorder in the structure through doping, without affecting transport properties of the edge states. This idea was realised in the work by Charpentier et al. [38], who used Ga doping. It was shown that depending on the type of the gallium source, the concentration of the impurities can be varied in GaSb layer, which results in resistivity of the bulk material changing from 2 KOhm in pure samples up to more than 1.5 MOhm in the sample which was produced using “low-mobility” Ga source.

A similar concept to suppress the bulk conductivity was implemented by the team of I. Knez [33,39]. The studied structures had the same design as in their pioneering works [22], except for a δ-layer of silicon placed between the InAs and GaSb layers. Silicon atoms serve as donors in InAs and acceptors in GaSb creating a localization gap in bulk energy spectrum. This makes the CQWfully insulating at low

temperatures, allowing observation of the conductance quantization, as the current flows through the edge channels. This result up to the moment is considered the most reliable demonstration of the QSHI in InAs/GaSb CQWs via transport measurements.

Although in low-mobility samples the conductance of the bulk material is much lower than that of the edge channels, so far conductivity quantization was observed only at temperatures below 1 K. In order to observe QSHE at higher temperatures, it becomes necessary to increase the bandgap of the structure. In pure InAs/GaSb CQWs increasing the bandgap above several meV is impossible. Higher hybridization gap requires better overlap between the wavefunctions in different layers, thus thinner InAs and GaSb layers. At the same time, as it was mentioned before, CQWs with too thin layers have non-inverted band structure thus cannot be used as a basis for QSHI.Larger value of the bandgap was obtained in heterostructures which have GaSb layer replaced by trinary compound - InGaSb [40,41]. The mechanism enabling such an increase is the strain of the active region of the structure which is imposed by the lattice mismatch between the InGaSb and AlSb constituting the barrier layer. The strain breaks the degeneracy of the subbands, and, as a result, hole band of the strained InGaSb at zero quasimomentum is split into heavy hole and light hole subbands, the latter being shifted higher in energy that in the non-strained structure. Meanwhile, the bottom of the conduction band in InAs is shifted lower in energy. As a result, the energy gap between these bands is increased. This allows using thinner QWs while keeping the band order inverted, which results in a better wavefunction overlap and higher hybridization bandgap. Moreover, the strain-enhanced heavy-hole and light-hole splitting prevents the undesirable interaction between these levels, which reduces the bandgap of the CQW [40].

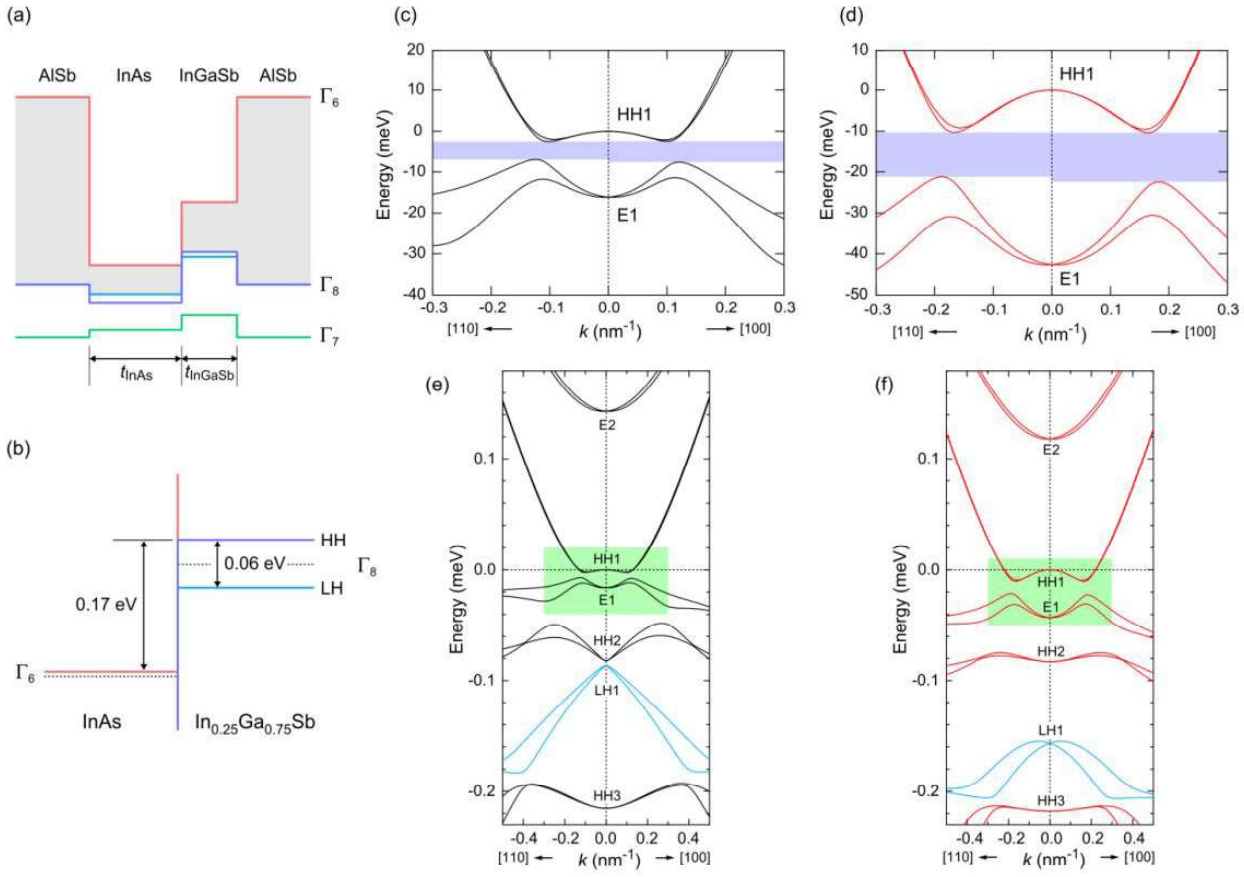

Fig. 5. (a) The band edge profile of InAs/$In_{0.25}Ga_{0.75}Sb$ quantum wells (QWs) with AlSb barriers, assuming pseudomorphic growth on AlSb. (b) Close-up of the band alignment at the InAs/$In_{0.25}Ga_{0.75}Sb$ interface. The dotted lines represent the position of the energy levels in the absence of strain. The valence band offset between InGaSb and InAs was defined for the "center of mass" of the HH and LH bands (i.e., without the shear strain term) and was taken to be 0.56 eV, equal to that between GaSb and InAs. (c)–(f) In-plane energy dispersions of unstrained InAs/GaSb QWs [(c) and (e)] and strained InAs/$In_{0.25}Ga_{0.75}Sb$ QWs [(d) and (f)], obtained from 8-band kp calculations. (c) [(d)] A close-up of the region marked by the green rectangle in (e) [(f)]. The shaded regions in (c) and (d) represent the energy gap for each k direction. Picture is taken from [40]

As far as the values of the bandgap are concerned, it was experimentally demonstrated that utilisation of strained structures allows to increase the bandgap at least up to 20 meV. Akiho et al. [40], carried out magnetotransport studied on a set of CQWs with 5.9-nm $In_{0.25}Ga_{0.75}Sb$ layer and InAs layers of different thicknesses. The highest bandgap value was obtained in a structure with 10 nm InAs layer and was equal to 10.8 meV. Similar designs were studied by Du et al. [41]. In their experiments, a set of strained structures with different In content x in the $In_xGa_{1-x}Sb$ layer were studied. It was shown that depending on x, the bandgap rises from 5 meV for structures with x = 0 up to 20 meV in structures with x = 0.32. As a consequence, the resistance of the bulk material in a strained structure reaches 100 MOhm, making a truly insulating hybridization gap at low temperature.

In the next chapter, it will be discussed that there is another way to increase the temperature operation of the future QSHI-devices, based on a new architecture proposed in Montpellier. InAs/GaSb/InAs triple quantum well (TQW)-based heterostructures introduced in [42] allow wide bandgap tuning by changing the parameters of the TQW. Calculations performed in [42] suggest that in such system the bandgap can reach 60 meV, which is comparable to monolayer films and strained HgTe/CdHgTe QWs.

Chapter 2. InAs/Ga(In)Sb heterostructures as a basis for wide-gap topological insulators

2.1 InAs/GaSb/InAs heterostructures with triple quantum wells

Recently, an elegant solution to the problem of increasing the bandgap in InAs/GaSb-based heterostructures was proposed by Krishtopenko et.al. [42]. In that work the structure asymmetry in the growth direction was addressed, which is the main factor for hybridization gap opening at finite quasimomentum. It was proposed to attach an additional layer of InAs to the structure, which restores the inversion symmetry in the growth direction, thus forming a W-shaped "trilayer" structure. GaSb layer in the middle of the structure serves as a QW for the holes, while the potential for the electrons is formed by two InAs QWs separated by tunnel transparent GaSb barrier (**Fig. 6 (a)**). In this case, the electronic subband is formed by two levels, *E1* and *E2*, which can be interpreted as even-odd state splitting, arising from the tunnel-coupling of the QWs. Here electronic subbands have been classified as electron-like or hole-like levels analogously to the bilayer InAs/GaSb CQWs; the difference being that we are comparing the relative contribution to a level at zero quasimomentum from the basis states of electrons and light hole ($|6,\pm1/2\rangle$, $|7,\pm1/2\rangle$, and $|8,\pm1/2\rangle$) bands with the contribution from the heavy-hole band $|8,\pm3/2\rangle$ [42].

Figure 6 (a) schematically shows the band-edge diagram for InAs/GaSb/InAs three-layer QWs (TQWs) confined by outer AlSb barriers grown on (001) GaSb buffer layers. As mentioned above, the broken-gap alignment at InAs/GaSb interface leads to the possibility of the band inversion in InAs/GaSb CQWs realized at certain thickness of InAs and GaSb layers. Inverted band ordering in TQW heterostructures is based on the same principle, but quantitatively the band structure of three-layer system is different from two-layer CQWs. Whereas the picture for *H1* state is roughly similar to the bilayer case, for the *E1* state the penetration of the barrier layer between the QWs is much higher. The hybridization gap opens in the spectrum owing to the interaction between electron and hole subbands and has the same energy scale. Better overlap between the wavefunctions in different layers also suggests the increase in bandgap due to stronger hybridization between the states. Calculations suggest over a three-fold increase of the gap value compared to bilayer CQWs (up to E_g=16 meV in pure InAs/GaSb/InAs structure [42]).

Another effect, that has significant impact on the band structure of the sample is its symmetry [43]. In asymmetrical structures the Bychkov-Rashba effect is present and according to Kramers theorem the spin degeneracy is preserved only at high symmetry points of the Brillouin zone. Thus, an inverted gap opens at finite value of the *k* vector. If one breaks time reversal symmetry (with magnetic field for

example) the spin degeneracy is lifted even at k = 0. But in symmetrical structures inversion symmetry is restored and the Bychkov-Rashba effect is switched off so the inverted gap can be open at k = 0. In bilayer CQWs the interaction is weak and significantly modifies spectrum only in the vicinity of the anticrossing point, thus the gap arises at non-zero k. In TQWs the better overlap between wavefunctions in different layers results into spectrum being affected by hybridization in the whole range of the wave vectors away from k = 0. Thus, the inverted bandgap arises almost at Γ point and the band structure becomes similar to HgTe/HgCdTe quantum wells. The top of the valence and conduction bands are both located at Γ-point with the valence band (formed either by hole–like states for non-inverted regime or electron-like states for inverted regime) having additional side-maxima (See **Fig. 6 (d-f)**).

Figure 6 (b) presents the position of electron-like ($E1$, $E2$) and hole-like ($H1$) subbands at k = 0 as a function of InAs-layer thickness, d_{InAs} for a fixed thickness of GaSb-layer (d_{GaSb} = 14 ML). The thicknesses are given in monolayers (ML), which correspond to the half of a lattice constant in the bulk material and is approximately 0.26 nm. (See Ref [42]). The calculations have been performed using an eight-band k · p Hamiltonian [42] with the parameters taken from [44], taking into account the strain effect arising because of the mismatch of lattice constants in the buffer, QW layers, and AlSb barriers. Details of theoretical calculations can be found in [45,46].

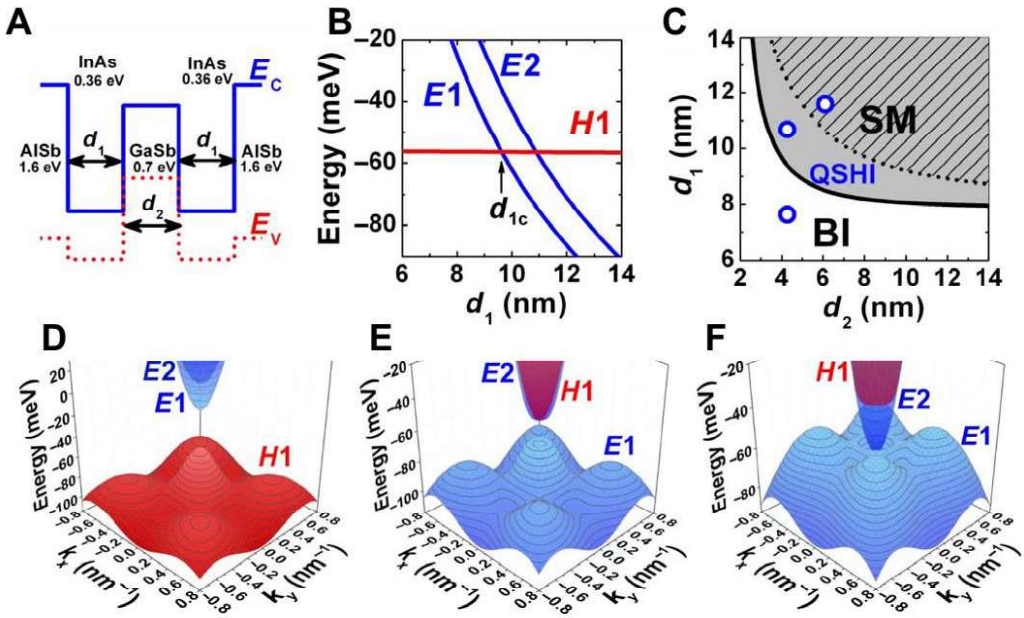

Fig. 6. a) Schematic representation of symmetrical three-layer InAs/GaSb/InAs QWs with be grown on (001) GaSb buffer. The numbers show the bandgap values in materials of the layers. Here, d1 and d2 are the thicknesses of InAs and GaSb layers, respectively. . (b) Energy of electron-like (blue curves) and heavy hole–like (red line) subbands at k = 0, as a function of d_1 at d_2 = 4 nm. Zero energy level corresponds to the top of the valence band in bulk GaSb. (c) Phase diagram for different d_1 and d_2.The white open region is a BI phase, whereas the

gray-striped region defines a SM phase. The gray open region corresponds to the QSHI state. (d to f) 3D plot of the band structure at BI (d), QSHI (e), and SM (F) phases. The x and y axes are oriented along (100) and (010) crystallographic directions, respectively. The thicknesses of the layers for each phase, used in the calculations, are marked in (c) by blue open symbols. Picture is taken from [42]

Figure 6(c) shows phase diagram of the InAs/GaSb/InAs heterostructure. The axes represent different thicknesses of the InAs(d_1) and GaSb (d_2) layers. The diagram is divided into three regions which correspond to trivial band insulator (white region), QSHI (open grey region) and semimetal (stripped grey region) phases. The solid curve dividing the plane into a white region with normal band order, and a gray region with inverted band order corresponds to the crossing between *E1* and *H1* subbands and gapless band structure. At this critical thickness of phase transition, the structure hosts single-valley 2D massless Dirac fermions, similarly to HgTe/CdHgTe QWs [47,48].

As can be seen from **Fig. 6 (c)**, at thick enough GaSb layer the structure can be tuned into any of three phases by varying the thickness of InAs layers. In structure with thin InAs layers, *E1* subband lies above the hole-like subband, and the three-layer QW has a trivial band ordering. Increasing d_{InAs} induces the mutual inversion between *E1* and *H1* subbands, resulting in band inversion of the QW. Further increase of d_{InAs} widens the gap between the *E1* and *H1* subbands and increases the bandgap of the structure. At large d_{InAs}, although the distance between *E1* and *H1* subbands at zero quasimomentum still grows with d_{InAs}, the bandgap of the structure first becomes indirect and, then, closes due to nonlocal overlapping between conduction and valence bands (**Fig. 6(f)**). Thus, by varying the layer thicknesses in three-layer QW, one can realize BI, QSHI, or SM phases. Panels (d-f) illustrate characteristic band structure for each of the phases, thicknesses of InAs and GaSb layers for each case are marked in the phase diagram by circles.

Experimental studies of three-layer InAs/GaSb/InAs quantum wells (with non-trivial band allignment) were previously focused on a specific band structure corresponding to the gapless state with a Dirac cone at the center of the Brillouin zone [47,48]. In the first work [48] the existence of massless Dirac fermions in InAs/GaSb/InAs quantum wells of specific design was confirmed by the measurements of the cyclotron resonance for different electron concentrations. It was shown that the measured dependence of the cyclotron mass on carrier concentration agrees well with the conical dispersion law obtained by calculations. This result was later confirmed [47] by magnetospectroscopy in higher magnetic fields up to 34 T. In strong quantizing magnetic fields, an absorption line associated with transitions from the lower Landau levels of electrons in a subband with a “conical” dispersion relation has been detected.

Thus, so far only gapless three-layer InAs/GaSb/InAs heterostructures with topologically non-trivial band ordering have been experimentally studied. Current work is devoted to further experimental probation of the ideas proposed in Ref. [42]. Its main focus is aimed at the investigation of inverted InAs/GaSb/InAs heterostructures and main features of their band structure. The goal of the experimental measurements is to demonstrate the possibility of achieving the inverted bandgap in three-layer CQWs comparable to that of competing systems (HgTe, WTe_2), making a step towards realization of high-temperature QSHIs. The studies in the original part of the work are organized around three following key-points:

- In optimised InAs/GaSb/InAs system it is possible to tune the inverted bandgap up to at least 16 meV.

- The further increase of the bandgap in a pure structure is impossible due to transition in semimetal state, which is analogous to the HgTe QWs.

- In strained structures with InAs/InGaSb/InAs layers this restriction is lifted and the gap of the structure can be raised at least up to 35 meV.

2.2 Magnetoabsorption spectroscopy

The main experimental technique used for sample characterization and their band-structure probing is magnetoabsorption (MA) spectroscopy. It is based on the spectral measurements of relative absorption of planar semiconductor structures in external magnetic field.

Fundamental effect of high magnetic field on the electronic system can be generally described as the restriction of the electron movement in a plane perpendicular to the magnetic field, which collapses of the density of states of the electrons and leads to Landau quantization. In other words, magnetic field introduces a structure of allowed and forbidden bands in otherwise continuous spectrum, forming a set of the energy levels, known as Landau levels.

From the experimental point of view magnetic field modifies the structure of the absorption spectrum of electron gas, by morphing the continuous spectrum into a set of allowed and forbidden bands. At the same time, magnetic field weakly affects the crystal lattice formed by mostly static ions. As a result, MA measurements allow isolating the optical response of the electronic system from the effects related to the absorption in the lattice and impurities as well as any external influence, such as transmission of the optical tract, sensitivity of the detector and emission spectrum of the source. In order to do that, the spectrum measured at each magnetic field was normalized by the reference spectrum measured without magnetic field. This allows compensating most of the spectral features not related to the absorption lines formed by inter-LL transitions.

At the same time such method has its limitations. First, it requires stabilisation of the external parameters - temperature of the sample, detector and the source. Second, using spectrum taken at zero field as a reference, some of the information is lost, because the electron gas retains the absorption lines, related to interband transitions without the magnetic field. As a result, at low fields, the transitions between LLs starting from different subbands (interband transitions) are weakly pronounced, because the reference spectrum has fundamental absorption lines with close energies.

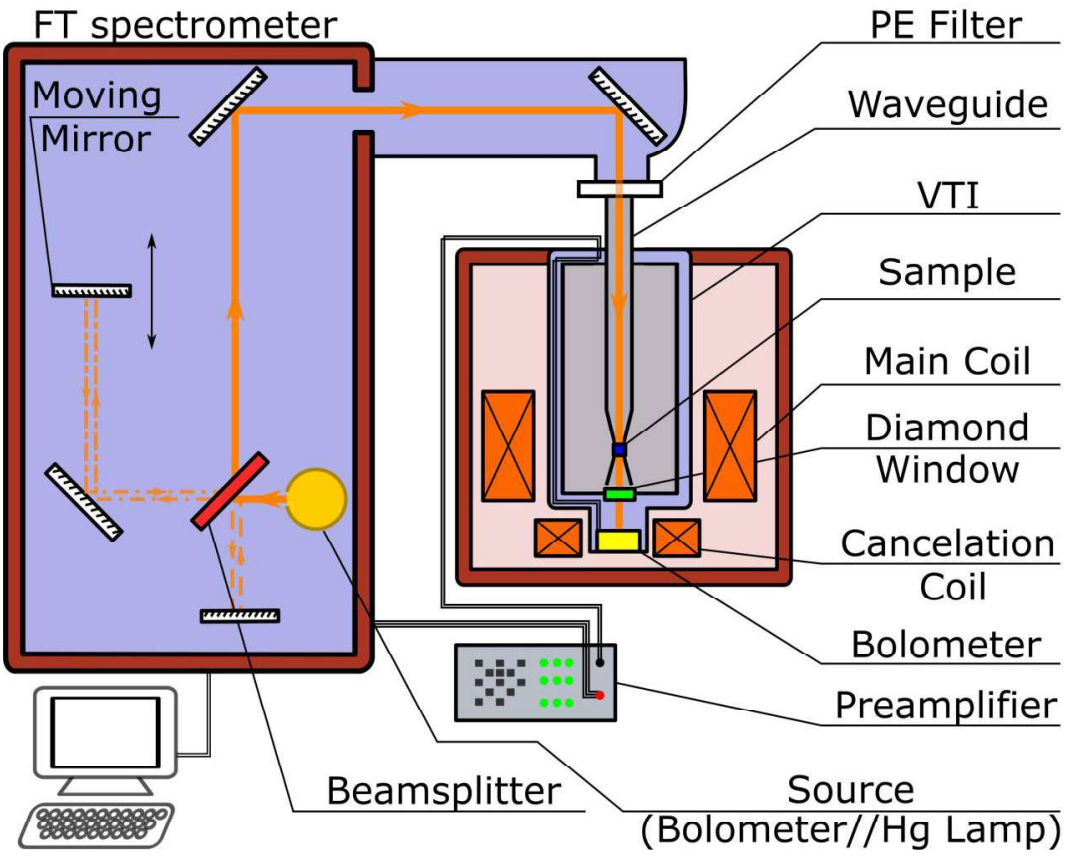

Fig. 7. Schematic representation of the setup for measuring magnetoabsorption spectra

The experiments were carried out using dedicated magneto-spectroscopic system. It consists of a custom liquid helium cryostat coupled to IR Fourier spectrometer (Bruker IFs 66v/S). An important feature of the spectrometer is the ability to evacuate the optical tract up to pressures below 10 mBar. Vacuum is necessary for the measurements in Far IR region because of the high absorption of the atmosphere (water vapour). The part of the waveguide, inserted in the cryostat is separated from the vacuum inside the spectrometer by an airtight Polyethylene filter.

The cryostat has two separate chambers. The outer reservoir is permanently filled with liquid helium, thus it has a constant temperature of 4.2 K. Cryogenic temperature is required for proper operation of the two main components of the system: bolometer and superconductive coil. The coil is immersed into liquid helium and positioned on the same level as the sample. It provides up to 16 T of continuous

magnetic field at its core. For the experiments in this work we used Faraday configuration when the magnetic field is parallel to the radiation wave-vector and perpendicular to the sample plane.

The sample is put into a separate chamber (variable temperature inset, VTI). VTI is a smaller coaxial anti-cryostat placed inside of the main reservoir. The main purpose of the VTI is the control the temperature of the sample, without interfering in the operation of the components requiring cryogenic cooling. The control of the temperature is achieved by the adjustable ohmic heater placed inside the VTI, the heating of which is compensated by introducing helium flow from the main reservoir through the side part of the inset.

At the bottom of the inset there is a diamond window, which is optically transparent in the IR region. The chamber below the window is designated to provide specific environment for the detector (composite QGEB/X bolometer). It is kept at constant temperature of 4.2 K as the chamber is surrounded by liquid helium. Additional superconductive coil is used to screen it from the magnetic field provided by the main coil.

The sample holder is equipped with a brass cone to focus incident radiation, and is optically coupled to the spectrometer by a system of mirrors and an oversized waveguide, which is a polished tube of non-magnetic stainless steel 10 mm in diameter. The optical path is screened from the outer space so that the sample receives only the radiation from the source and a small fraction of the thermal background from the waveguide and spectrometer walls. We also ensure that the sample was fully blocking the optical path; otherwise the light going around the sample would cause the parasitic signal which does not depend on the magnetic field and effectively reduces the amplitude of the observed absorption lines.

During MA experiments radiation from the spectrometer (Globar lamp or high pressure Hg lamp) is guided through the sample and detected by the bolometer. The signal is then recollected from preamplifier (Amatec 5113) and passed back to the Analog-to-digital converter of the spectrometer, where Fourier transform is performed and the final spectra are calculated.

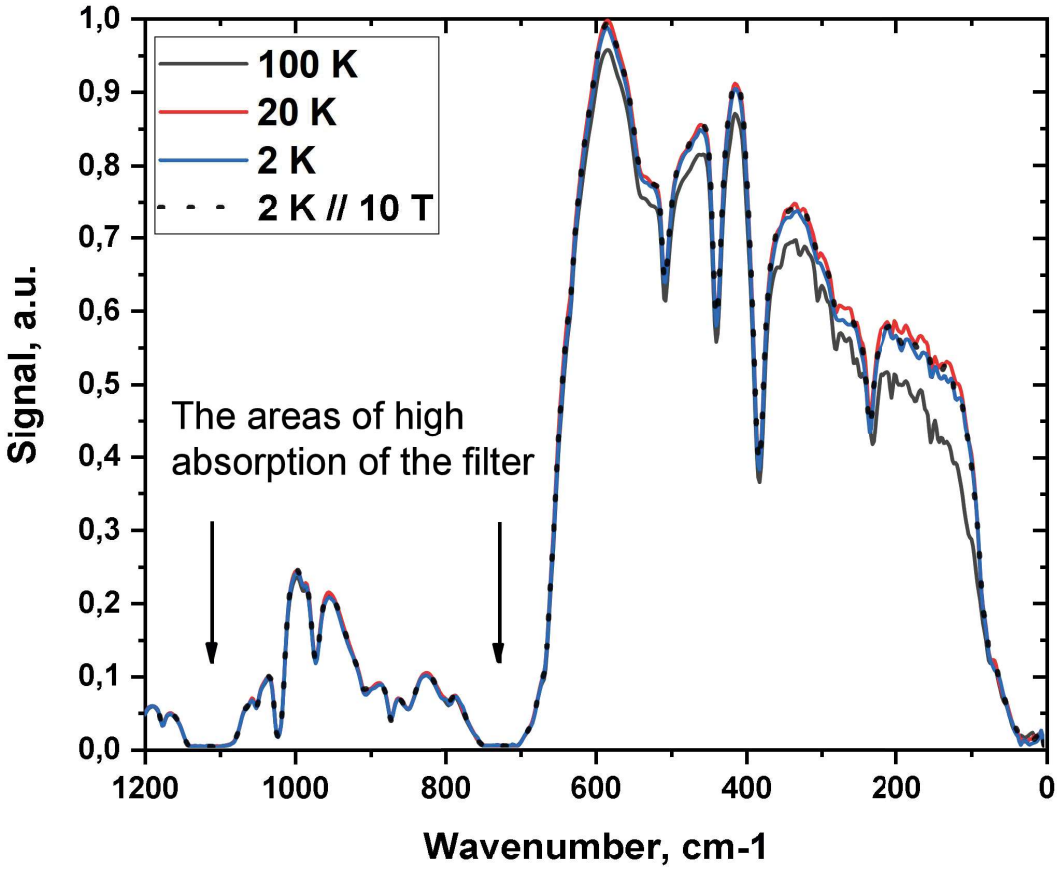

Fig. 8. Transmission spectra of the optical path measured at different temperatures without the sample. Dotted line represents the transmission spectrum measured at B = 10 T. KBr beam-splitter and Globar source are used to provide the highest signal tin the range from 100 to 700 cm-1. These conditions of the experiment are similar to the ones used for all magnetoabsorption measurements.

The transmission spectra of the optical path without the sample at different temperatures are presented in **Fig. 8**. Generally, the available spectral range is limited by the filter and sensitivity of the bolometer, while the beam-splitter and radiation source can be selected depending on the range of interest.

Spectral range used in this work lies between 30 and 1100 cm-1, thus the Globar source and KBr-based beam-splitter were used. As one can see in **Fig. 8**, the sensitivity of the system demonstrates weak dependence on the temperature. Significant reduction of the signal caused by the heating of the bolometer is seen only above 100 K. Another important result illustrated in Fig.8 is independence of the transmission of the optical path on magnetic field, which conditions the normalization by transmission at zero magnetic field used in this technique.

Important note is that although the transmission dependence on the wavenumber is not flat, it does not affect the final absorption spectra as it is compensated by the normalisation procedure. The only parameter affected by the transmission is the level of noise which is higher in the areas of the high

absorption. In the spectral ranges, where transmission tends to zero, the noise is too high to extract the signal. Without the sample these regions are caused by the polyethylene filter and lie from 700 to 750 cm^{-1} and from 1080 to 1150 cm^{-1}. As the sample fully covers the optical path, it causes other “blind spots” which are usually related to high absorption of the lattice (*Reststrahlen* bands). These regions are sample- and temperature- dependent so they will be specifically marked for each spectrum.

Small values of effective masses of charge carriers in dimensional quantization subbands of InAs/GaSb/InAs TQW [47] lead to the fact that cyclotron energy is comparable to the bandgap energy in moderate magnetic fields. Therefore, in the magnetoabsorption spectra in the far- and mid- IR ranges in such structures there are both intraband transitions (also referred as cyclotron resonance, CR-like) and interband transition lines [49]. Comparison of the dependence of transition energies as a function of magnetic field with the results of theoretical calculations lets us identify the observed transitions and reconstruct the band structure of the investigated samples.

The band structure of the samples was probed by Landau-level MA spectroscopy in magnetic fields from 0 to 16 T at different temperatures ranging from 2 K up to 100 Ktracing the energy of inter-LL transitions depending on the magnetic field and temperature. Comparison of experimental data with the calculated energies of the same transitions allows extracting both the bandgap and the topological phase of the structure.

The bandgap of the structure was derived from the low-field trend of observed interband LL transitions. As the magnetic field approaches zero, the energy of such transitions reaches the value of the band gap [50–54]. Insofar as for the studied samples the interband LL transitions are observed only at strong (>7T) magnetic fields, the results obtained by magneto-optics were then verified by THz photoluminescence (PL) measurements at zero magnetic field. PL spectroscopy allows direct observation of the optical transitions between size quantisation levels of the TQW and thus, extracting the optical bandgap of the structure. PL results will be discussed in more detail in **Section 2.7**.

It should be considered, that a specific range of bandgap values can be obtained both in topologically trivial and QSHI phases, so for complete description of the structure we need to obtain the information on the band ordering. Historically topological phase of the structures was determined on the basis of behaviour of a specific pair of the LLs, which start from the bottom of the conduction band and top of the valence band and then either diverge or cross at some magnetic field [19,55,56]. The crossing of these levels is a typical signature of the inverted-band ordering under quantizing magnetic field.

The origin of such a pair, also called zero-mode LLs, becomes clear from an effective Dirac-type Hamiltonian [12] written for the states in E_1 and H_1 subbands. For the structure in the inverted regime, below the critical magnetic field B_c, at which the zero-mode LLs cross, both levels are formed by the states of the "opposite" band. In particular, the energy of the first zero-mode LL approaches the

energy of a valence subband as magnetic field goes to zero but it grows with magnetic field similarly to the levels starting in the conduction band. The second level, starting from the conduction band, in low magnetic fields $B < B_c$, is formed by the heavy hole basis states and its energy decreases with magnetic field. At magnetic fields above the critical ($B > B_c$) there is a mutual inversion between zero-mode LLs is and the system transitions into topologically trivial phase. In a QW with normal band order, electronic and heavy hole levels occur at $B = 0$ in the conductivity and valence bands, respectively, and zero mode LL do not cross. [49] (See Figure 8).

2.3 Studied structures

The studied structures were grown by solid-source molecular beam epitaxy (MBE) on a semi-insulating (001) GaAs substrate. After deoxidation at around 600°C a thick undoped GaAs buffer layer was grown. The large lattice-mismatch between GaAs, GaSb, and AlSb (~ 8%) was accommodated through a thick (more than 1 μm) GaSb buffer layer followed by a ten-period 2.5-nm-GaSb/2.5-nm-AlSb superlattice, all grown at 500°C. Subsequently, the substrate temperature was decreased down to 420°C to grow the active part of the structures, which consists of three-layer InAs/GaSb/InAs QWs confined by 50-nm-thick AlSb barrier layers. A 6-nm GaSb cap layer was grown on top of the structure to prevent oxidation of the AlSb barrier layers [49]. Relatively small concentration of the electrons in the sample allowed us to observe transitions between states of the valence subband and two bottom conductivity subbands, both in MA and photoluminescence spectra.

For sample v2561, we used a buffer layer of GaSb, while samples v2554 and v2808 were grown on the AlSb buffer. In addition to changing the buffer layer, the samples differ in the design of the active region. In structures v2561 and v2554 TQW was formed by InAs and GaSb layers, while for structure v2808 we used GaInSb layer with 35% In content as a middle layer.

The difference in designs of active region and used buffer layers is conditioned by the required band structure. In particular, sample v2561 was designed to obtain the maximum inverted bandgap in unstrained InAs/GaSb/InAs structures grown on GaSb buffer. Sample v2554 has a band structure corresponding to the transition between the states of 2D TI and semimetal. Structure v2808, having the narrowest wells (24 ML and 10 ML for InAs and GaSb layers correspondingly), is designed to obtain a bandgap of more than 20 meV, which is currently the maximum value of demonstrated in $A_{III}B_V$ materials. TQW thicknesses are given in the number of MLs analogously to Ref. [42].

Table 1. Growth scheme of the studied trilayer structures.

V2561		V2554		V2808	
GaSb	6 nm	GaSb	6 nm	GaSb	6 nm
AlSb	50 nm	AlSb	50 nm	AlSb	50 nm
InAs	**34 ML**	InAs	**37 ML**	InAs	**24 ML**
GaSb	**14 ML**	GaSb	**14 ML**	GaInSb 35 %	**10 ML**
InAs	**34 ML**	InAs	**37 ML**	InAs	**24 ML**
AlSb	50 nm	AlSb	50 nm	AlSb	50 nm
GaSb 2.5 nm	}x 10	GaSb 2.5 nm	}x 10	GaSb 2.5 nm	}x 10
AlSb 2.5 nm		AlSb 2.5 nm		AlSb 2.5 nm	
GaSb	1.5 μm	AlSb	1,5 μm	AlSb	1 μm
GaAs SI		GaAs SI		GaAs SI	

2.4 Magnetospectroscopy of heterostructure with InAs/GaSb/InAs TQW in the inverted regime

The first part of the studies is devoted to band structure of inverted InAs/GaSb/InAs TQW heterostructure which shares growth technology with previously studied zero-gap structures [48]. This helps to keep the consistency between the studies and allows us to rely on the previous results for the interpretation of experimental data.

Active region of the sample was designed with the help of band structure calculations performed using an eight-band Kane Hamiltonian [42] with the parameters taken from Ref. [44]. These calculations are used to link the growth parameters with band structure of the TQWs and are pivotal for the interpretation of experimental data. As long as we want to construct a structure which can demonstrate QSHI regime at the highest possible temperature, the local goal of the studies was to maximize the band-gap for a given buffer and QW strain. According to calculations, for GaSb buffer the inverted band-gap reaches its maximum at thicknesses of InAs and GaSb layers equal to 34 and 14 MLs respectively. These values were used for the fabrication of the sample. It needs to be pointed that for other buffer materials, the maximum gap is achieved at different thickness of InAs and GaSb layers [42].

The sample was not intentionally doped. Its characterisation performed by magnetotransport measurements at 2 K gives electron concentration and mobility equal to 6.2×10^{11} cm^{-2} and 2×10^{4}

cm^{-2}V*s, respectively. The band structure and Fermi-level position obtained from the electron concentration are shown in **Fig. 9** [49].

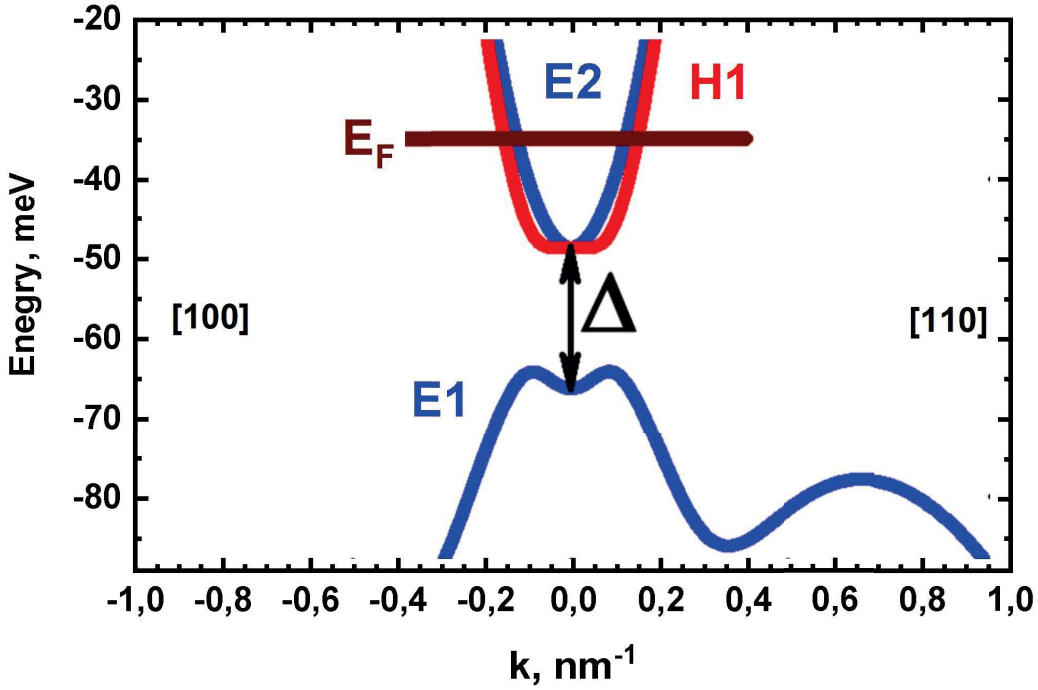

Fig. 9. Band structure of sample v2561 calculated by S. Krishtopenko. Numbers in brackets denote crystal directions. The brown line indicates the position of the Fermi level E_F found from magnetotransport measurements. Courtesy of S. Krishtopenko et al. [49]

Figure 10 shows the calculations of LLs for structure v2651, performed by S.S. Krishtopenko. To calculate the energy of LLs we used axial approximation, assuming the rotation symmetry of the system in the plane of the QW [46], which allows us to simplify the calculations. For further details of theoretical model, one can see Refs. [42,46].

Within the framework of axial approximation, the wave function of a given LL with the index $n > 0$ is determined by eight components describing the contributions to a certain LL from different bands of bulk material with Γ6, Γ7 and Γ8 symmetry. It is important to note that for indexes $n = 0$, -1 and -2 only seven-, four- and one-component wave functions were obtained. A single LL ($n = -2$) contains only the contribution from the heavy-hole band |Γ8, -3/2> [45] and its energy decreases almost linearly with magnetic field. This level, together with one of the characteristic solutions for $n = 0$, forms a pair of zero mode LLs [26,50,57] described above. For comparison, **Fig. 10b** shows the calculation of LL energies for a TQW with $d_{InAs} = 34$ ML and $d_{InAs} = 27$ ML which has a comparable gap at $k = 0$, but different band ordering.

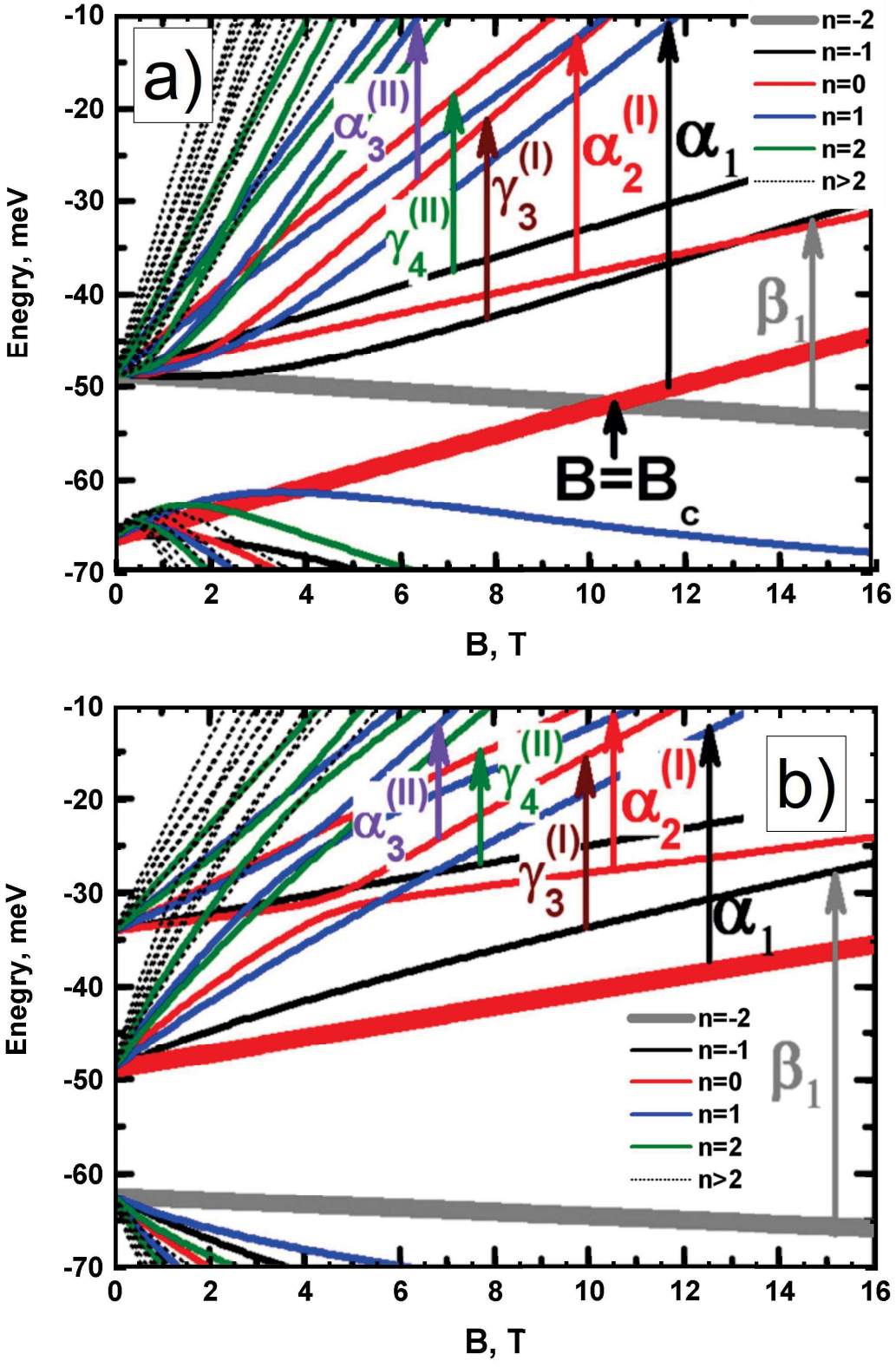

Fig. 10. Results of Landau level energy calculations for indices from n=-2 to n=2 for InAs/GaSb/InAs QWs with (a) inverted band structure, d_{InAs} = 34 ML, d_{GaSb} = 14 ML (investigated structure), and (b) non-inverted band structure, d_{InAs} = 27 ML and d_{GaSb} = 14 ML; Figures in the right part denote LL indices. The supposed most intense absorption transitions are indicated by arrows and Greek letters. The pair of zero mode LLs with indexes -2 and 0 is shown in bold curves. Courtesy of S. Krishtopenko et al.

The experimental results are presented in (**Fig. 11, 12, 14**). **Fig 11 (a)** shows the transmission spectra measured at temperature 100 K with magnetic field *B* ranging from 0 to 15.9 T in 0.5 T steps. The spectral resolution for all measured spectra was equal to 0.5 meV. After the measurement each spectrum was normalized for the transmission at *B* = 0, revealing the field-dependent spectral features. Absorption lines associated with optical transitions between LLs are reflected as a set of hollows in otherwise flat (transmission, *Tr(k)* ≡ 1) spectra. The position of the absorption lines is marked with coloured symbols in **Fig 11 (a)**, **Fig. 11(b)**.

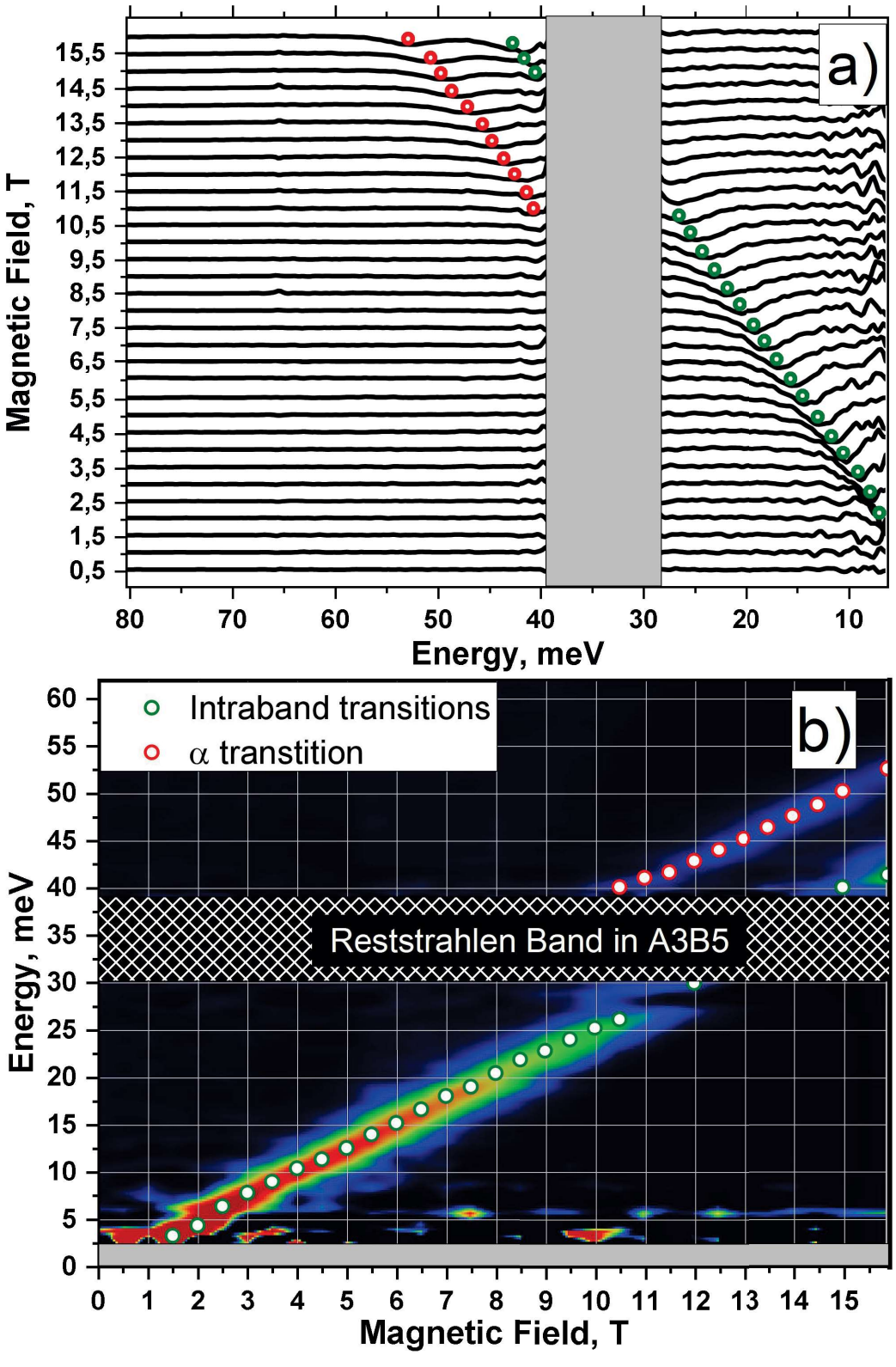

Fig. 11. Magnetoabsorption data of structure v2561 at 100 K. (a) waterfall plot of the absorption spectra in the range of magnetic fields from 0 to 15.9 T, (b) "Coloured map" of the observed transitions

Figure 11 (b) is a colour map. It represents the same data set as in **Figure 11 (a)** in a form of two-dimensional surface graph, where the *x* and *y* axes, represent the magnetic field and transition energy, respectively, while the transition amplitude is encoded with the colour of the corresponding point on the graph. Dark blue colour represents maximum relative transmission ($Tr(k_0)$ = 1), and dark red colour corresponds to the lowest transmission outside the non-transparent areas, which varies from sample to sample and has a typical value of 0.95 - 0.98.

The lower boundary of the displayed spectral range is determined by the transmission of the optical path, while the upper boundary is selected according to the highest observed transition energy and can be extended up to 80 meV (See **Fig. 6**). In addition to general limitation of the system, the spectra contain a region of low transmission caused by *Reststrahlen* band in InAs, GaSb and AlSb layers which is covered with grey stripes and hatching on the transmission spectra and colour maps respectively.

At 100 K, two absorption lines are clearly visible. The first line corresponds to the intraband transition and in small fields its energy tends to 0. This line corresponds to “CR-like” transitions in E2 and H1 subbands, which in low fields transform into classical cyclotron resonance. The transitions have close energies due to the close values of cyclotron mass in m_c in E2 and H1 subbands at the observed electron concentration [49]. The cyclotron mass in the direction of structure growth at Fermi level at 2 K is about 0.0434 and 0.0426 of free electron mass, m_0. The analysis of experimental data gives values m_c = (0.044 ± 0.004) m_0, which agrees well with theoretical values.

At frequency above the *Reststrahlen* band the second line appears. It lies higher in energy than the CR-like line and is observed only in high (over 10 T) fields. We link this line to the interband transition between LLs. Unfortunately high concentration of electrons in our samples does not allow us to trace the transition energy of a second transition in low magnetic fields. Therefore, we cannot directly extract the bandgap at B = 0 from the MA data. However, we can estimate the difference between the energies for a CR-like and interband transition. The value of this difference at B = 0 determines the gap, because the first line starts from zero energy and the second one from the energy equal to the distance between the bands. At high fields the energy difference tends to a constant valuewhich according to our experimental data, is equal to ≈ 8 meV for B > 10 T. Direct extrapolation of this value to zero magnetic field not possible due to strong non-linear behaviour of LL energy at low fields, but it can be found by accurate calculations for the gap at zero magnetic field give a value of 16 meV.

When the energy tends to the energy of LO-phonons in AlSb barriers (ω_{LO} = 40.9 meV), both transitions bend away from the phonon energy, thus, deviating from linear behaviour. The latter is clearly visible for measurements at 2 K and 20 K (see also **Fig. 12, Fig. 14**). This effect can be associated with electron-phonon interaction (polaron effect), as it also manifests itself in the vicinity of phonon energies in the InAs layers (ω_{LO} = 30 meV and ω_{TO} = 27 meV) and GaSb (ω_{LO} = 29.8 meV and ω_{TO} = 28.6 meV). This is confirmed by the fact that bending of the lines is less pronounced at higher temperature (See **Fig. 14**), as the coupling between electrons and phonons weakens.

At the same time similar bending of the lines can be of purely optical origin. In our case, the optical response of the system is determined by two highly resonant processes: the resonant dielectric function of the material at the phonon frequency (both TO and LO) and the absorption of a two-dimensional electronic system in magnetic field. Thus, the profile of absorption lines can be strongly distorted by the singularities of the dielectric function at phonon frequencies in QW and barrier materials. At the moment, the evidence for any of these mechanisms is not sufficient to make a confident conclusion.

An important property of InAs/GaSb-based structures predicted by the theory is that the bandgap value does not change with temperature. That is an important advantage over HgTe/CdHgTe QWs, for which it decreases as the temperature grows. In order to verify this assumption, we performed MA measurements at other temperatures. **Figure 12** shows the transmission spectra with the same configuration of the system but at temperature of 20 K.

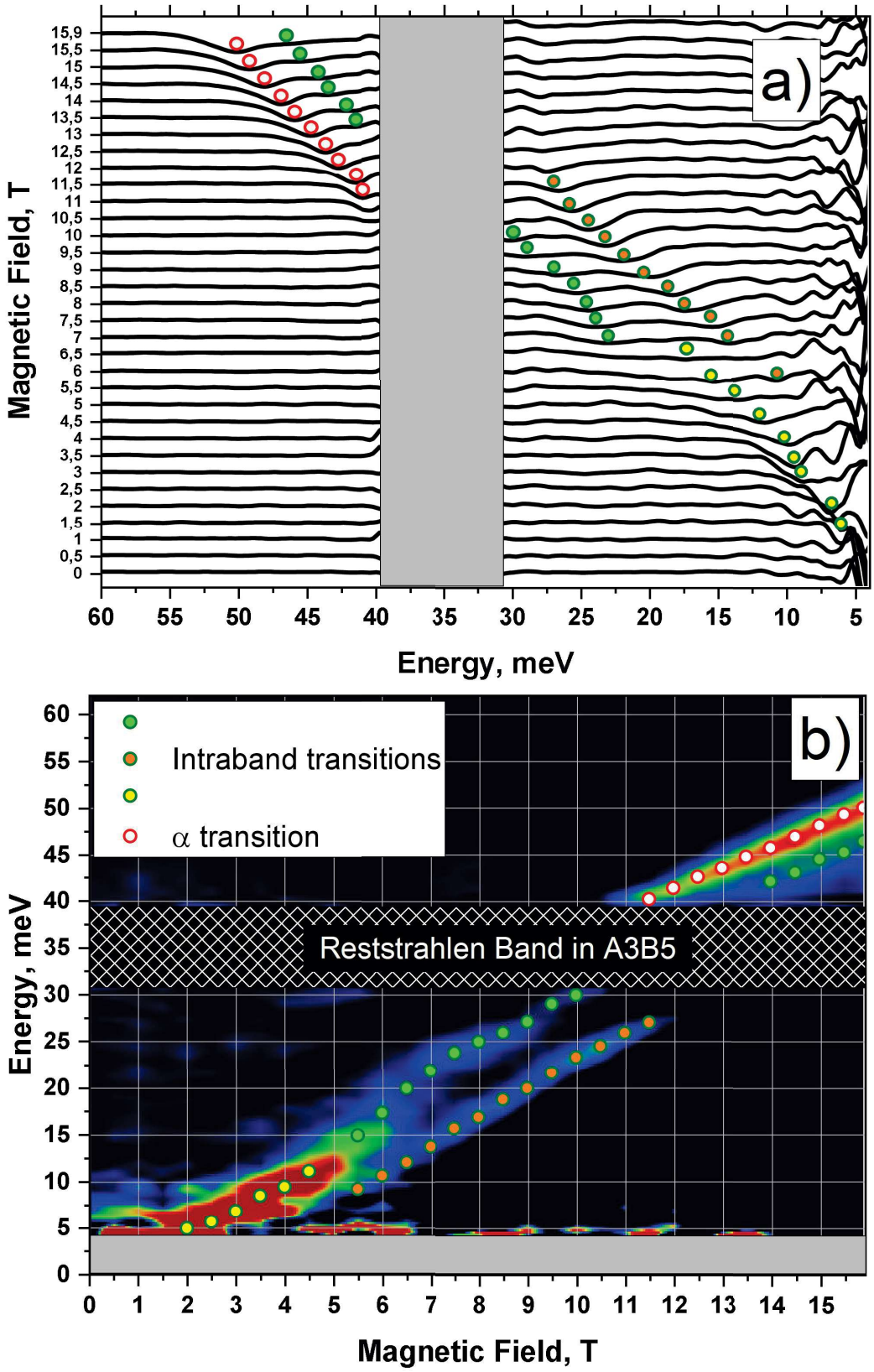

Fig. 12. Magnetoabsorption data of structure v2561 at 20 K. (a) waterfall plot of the absorption spectra in the range of magnetic fields from 0 to 15.9 T, (b) "Colour map" of the observed transitions

Overall the results at 20 K are different from the spectra we have obtained at 100 K. At low magnetic fields the absorption line is formed by multiple transitions making its width is larger than at 100 K. The

most noticeable feature is splitting of this line in two which occurs at 5 T. This effect arises due to the shift of the position of Fermi energy with temperature. In common wide-gap semiconductors the valence and conduction bands are not interacting and their dispersion is described well by effective mass approximation. However, the studied system features strongly interacting electron and hole subbands, and energy momentum relation for the electrons is not quadratic (See **Fig. 9**). In magnetic field this effect manifests itself in non-linear dependence of LL energy on magnetic field as well as differemt transition energy between different pairs of LLs with indices $n = \pm 1$ (compare transitions $\gamma_3^{(I)}$, $\gamma_4^{(II)}$ in **Fig. 10**). Thus, as long as the position of the Fermi level allows us to observe multiple intraband transitions the measured spectra may contain multiple absorption lines. In classical interpretation this splitting reflects the difference in the cyclotron masses of conduction subbands (*E2* and *H1*) at different values of quasimomentum.

The interband transition is observed at magnetic fields higher than 11.5 T, when its energy surpasses *Reststrahlen* band. Comparison of the data, measured at 100 K and 20 K shows that the energy of interband transition is temperature independent. At the same time, the position of CR-like transition cannot be directly compared for two cases. In order to extract the bandgap value we require additional calculations for proper definition of the intraband transitions.

Since the magneto-absorption spectra were measured in the Faraday configuration, the optically active transitions between LLs are subject to the common selection rules $n = \pm 1$ (for non-polarized radiation) under dipole approximation. However, the proximity of the H1 and E2 subbands, as well as the position of the Fermi energy (see **Fig. 9, 10**) suggest that there are many possible transitions that satisfy this rule. Therefore, to identify the absorption lines observed in the experimental spectra, it is necessary to refer not only to the calculations of the LL energies but also to the calculations of the matrix elements. For the allowed optical transition between the states indexed *l* and *m* matrix elementcan be written as (Following Ref. [58])

$$M = (2m_0)^{1/2} \langle \Psi_m \mid e \cdot \hat{v} \mid \Psi_l \rangle \qquad (3)$$

Where m_0 – free electron mass, Ψ_i is the eight-component envelope function of the eight-band **k · p** Hamiltonian $\hat{H}k^{8\times8}$, **e** is the unit vector of light polarization, and ***v̂ is the velocity operator, determined*** as

$$\hbar\hat{v} = \frac{\partial H_k^{8\times8}}{\partial k} \qquad (4)$$

In Eq. (3), *l* and *m* are assumed to be the complex symbols, including subband, “spin” indices and LL number *n* [or quasimomentum $k_{||} = (k_x, k_y)$ in the QW plane in the absence of magnetic field]. For

analysis of the absorption or emission spectra caused by dynamical conductivity [58], instead of optical matrix elements M, it is more convenient to operate with the oscillator strength of the given transition $f_{osc}(m,l)$, defined as

$$f_{osc}(m,l) = \frac{2m_0 \mid \langle \Psi_m \mid e \cdot \hat{v} \mid \Psi_l \rangle \mid^2}{\mid E_m - E_l \mid} \qquad (5)$$

Since the orientation of the light polarization projection on the QW plane was not controlled during the experiments, it is necessary to average $f_{osc}(m,l)$ over all orientations of the component of the electric field lying in the QW plane. In this work we have analyzed all possible transitions with $n = \pm 1$ involving LLs with indices -2, -1, 0, 1, which can be observed in our structure.

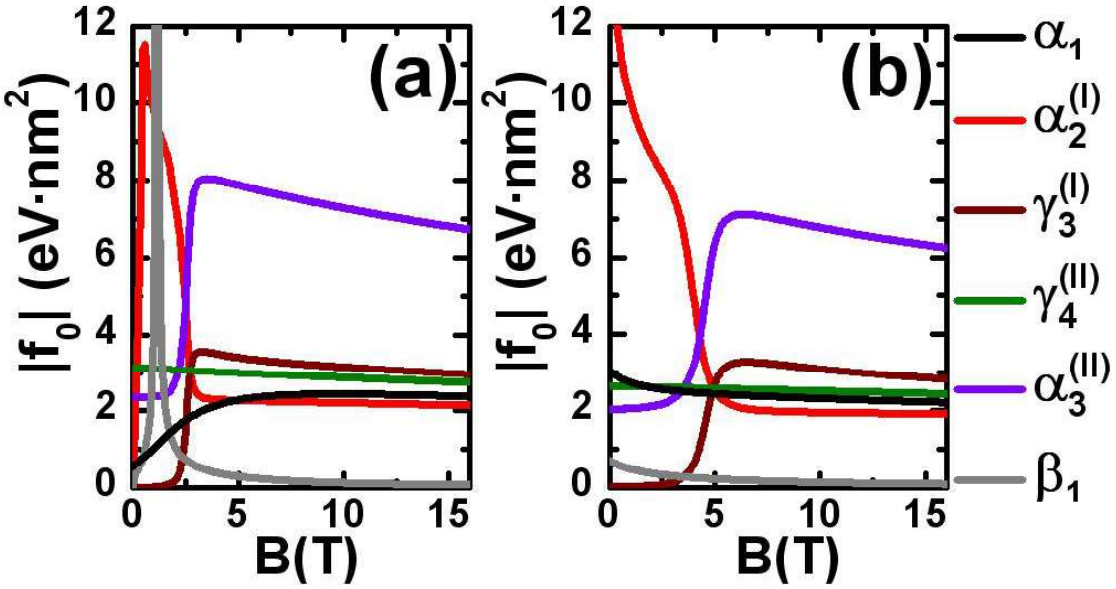

Fig. 13. Oscillator strength $f_0 = \hbar^2 \overline{f_{osc}} / 2m_0$ for Landau-level orientation of the light polarization lying in the QW plane. The (a) and (b) panels are connected with those in Fig. 8. Courtesy of S. Krishtopenko et al.

Fig. 13 shows the oscillator strength for the brightest transitions between LLs shown in **Fig. 10 (a,b)**. As it was expected, the most intensive transitions are intraband transitions in E2 (transitions $\alpha_2^{(I)}$ and $\gamma_4^{(II)}$) and H1 (transitions $\alpha_3^{(II)}$ and $\gamma_3^{(I)}$) subbands, which develop in quantizing magnetic fields from classical cyclotron resonance and interband transition α_1. Oscillator strengths of the other transitions are several times smaller than of these levels. The non-monotonic oscillator strength behaviour in low magnetic fields is caused by multiple intersections between LLs with the same indices from subbands E2 and E1. The latter leads to a non-monotonic dependence of the transition energy and the optical matrix element *M* on the magnetic field for a given transition in the proximity of the intersections. As can be seen from **Figure 13**, the oscillator strength for transitions α_1, $\alpha_2^{(I)}$, $\gamma_3^{(I)}$, $\gamma_4^{(II)}$, $\alpha_3^{(II)}$, in high

magnetic fields has comparable values and similar behaviour for QW with trivial and inverted band structure. It is noteworthy that in the Faraday configuration, interband transitions between LLs starting from E2 and E1 subbands are practically prohibited for all indices. Prohibition of the interband transitions comes from the fact that they are non direct in the in the real space, as the wavefunctions of electron and hole levels are localized in different layers. The only interband transition in the studied structure that has oscillator strength comparable with those of the intraband transitions is α_1, which involves zero mode LL with index $n = 0$ characterized by high contribution from the from electron subband. The opposite argument is valid for the intraband transition β_1.As long as zero mode LL with index $n = 2$ is formed by the hole-like states the matrix element of β_1 is much smaller compared to other intraband transitions which is also shown in **Fig. 13**. Interband transitions from the second zero-mode LL are not presented in spectra because of the high position of the Fermi level. Thus, the second absorption line appearing in spectra in high magnetic fields is attributed to α_1 transition (**Fig. 10(a)**).

Fig 14 summarizes the experimental results obtained at temperatures of 2 K (**Fig. 14(a)**) and 100 K (**Fig. 14(b)**). Comparison of experimental and theoretical transition energies is shown on the bottom panel. Theoretical dependencies obtained using structure parameters at 2 K are represented by coloured curves. The solid part of each curve reflects the range of magnetic fields in which concentration of electrons (using the value was obtained at 2 K) allows the transition to be observed. The dotted line corresponding to the transition β_1 places emphasis on the smallest oscillator strength of this transition.

As can be seen from **Figure 14(c)**, the experimental data at both temperatures is in good agreement with the theoretical prediction. The splitting of the absorption line occurring at 2 K and 20 K in the spectra at B = 7 - 11 T is also qualitatively described by the used model. The low-energy absorption is formed by the group of four intraband transitions, two of which ($\alpha_2^{(I)}$ and $\gamma_3^{(I)}$) are related to the E2 subband and two ($\gamma_4^{(II)}$ and $\alpha_3^{(II)}$) to the H1 subband. In low fields the energies between the corresponding LLs are almost equal, however, as the field grows, the discrepancy increases, which is a consequence of the non-parabolicity of the subbands. The stronger splitting of the absorption lines observed in the experiment may be a consequence of the lack of bulk inversion symmetry and the influence of low-symmetric interfaces, which were not considered in our calculations

Interestingly, in the range B = 7 - 11 T, the temperature increase does not affect the absorption lines corresponding to low energy peaks while the high-energy component of the split lines disappears completely at 100 K. The latter is directly indicates a change in the concentration of electrons with temperature, which determines the LL filling factor. Although the position of the low-energy line, which can be attributed to different CR-like transitions at different carrier concentrations, changes slightly with temperature, the position of the high-energy line identified as the interband transition α_1 remains

unchanged at temperatures between 2 and 100 K which is clearly visible in high magnetic fields at energies above the *Reststrahlen* band. This also indicates that the resonant energy caused by this transition is temperature independent.

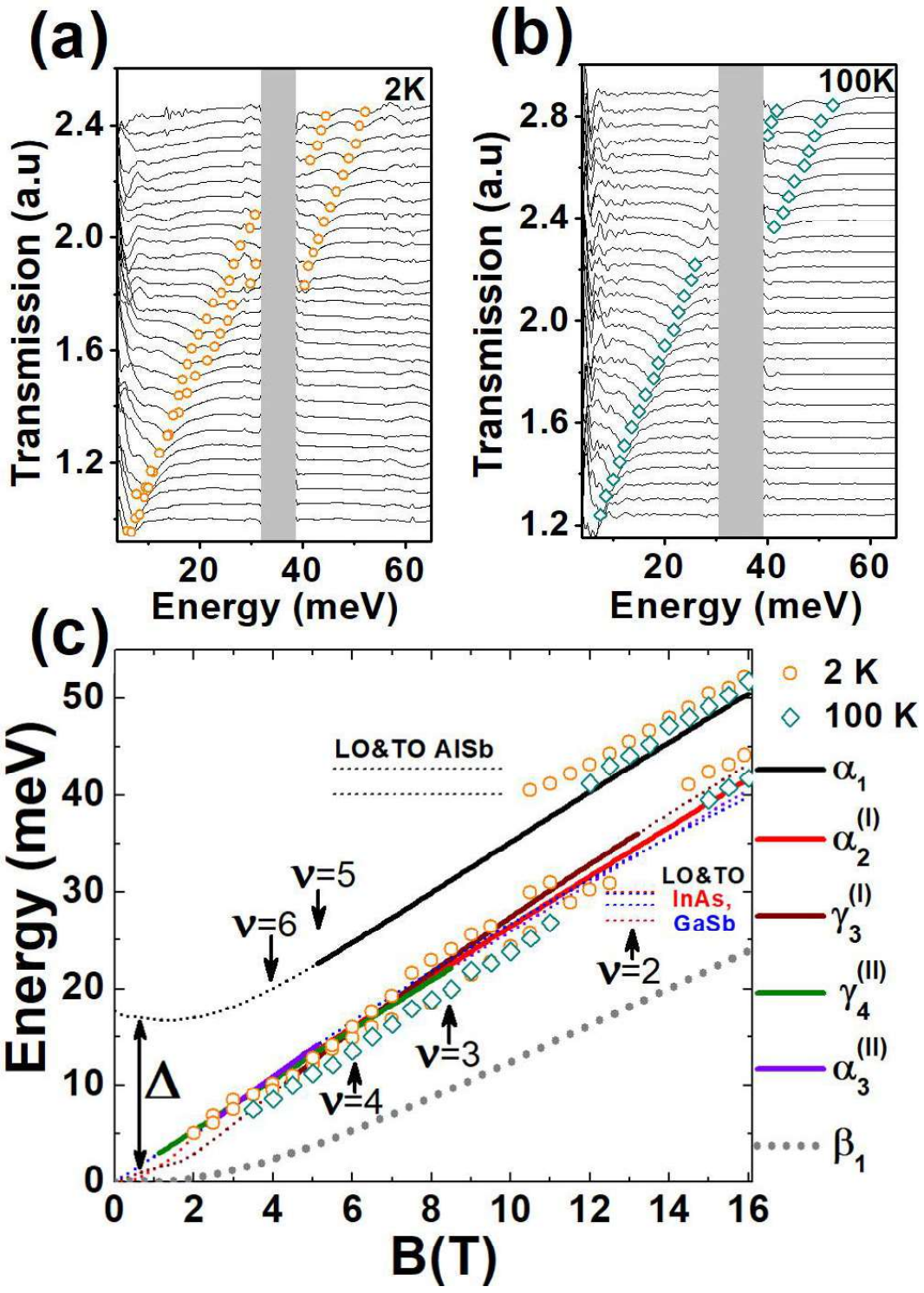

Fig. 14. Transmission spectra a) at 2 K and b) 100 K from 1 T (the first plot at the bottom) to 16 T (the last plot on the top) with a step for the magnetic field of 0.5 T. Shaded areas indicate the *Reststrahlen* band of GaAs substrate. The symbols mark positions of absorption lines. (c) Fan chart of the most intense LL transitions, marked in Fig. 8(a) by arrows. Experimental data at different temperatures are represented by symbols. The arrows indicate the magnetic fields,

corresponding to integer LL filling factors v at 2 K. Horizontal dashed lines correspond to the energies of TO and LO phonons in AlSb (in black, ω_{LO} = 42.7 meV and ω_{TO} = 40.1 meV), InAs ω_{LO} = 29.8 meV and ωTO = 28.6 meV) Courtesy of S. Krishtopenko et al.

An important feature of InAs/GaSb/InAs TQWs is that the absorption line associated with the transition β_1, in which the second of the zero-mode LLs is involved, is not observed (see B > 13 T, corresponding to v < 2) due to the small values of oscillator strength (see **Fig. 13**). The absence of absorption line associated with one of the zero-mode LLs does not allow to determine the topological phase of the structure based on the crossing of these levels, as it is done for HgTe QWs [59]. However, the absence of the absorption line associated with β_1 transition in the spectra makes it possible to indicate the band ordering of InAs/GaSb/InAs TQW in a different way. As can be seen from **Figure 10**, when the band structure is inverted, the transition α_1 has the largest energy in high magnetic field, which at diminishing B tends to the energy of the gap at k = 0. For the normal band ordering, this behaviour is characteristic of the transition β_1 (see **Fig. 10b**). However, since the oscillator strength is weakly dependent on the band ordering, the transition β_1 is weakly expressed in a TQW with the normal band ordering as well. Moreover, in non-inverted case, all the interband transitions are going between the levels formed by the basis states localized in different layers and are weaker than the intraband transitions. Consequently, since all transitions between LLs in a TQW with normal band ordering are intraband, the observation of the high-energy line corresponding to the interband transition in our sample indicates the inversion of its band structure.

Thus, the results of magnetospectroscopy clearly demonstrate the inverted band structure of sample v2561. The bandgap at magnetic field, which is determined by the difference between the observed intraband and interband transitions, is 8 meV in the range of fields above 11 T. The results of the calculations suggest that this value increases up to 16 meV at the zero magnetic field. This result is confirmed by the terahertz PL studies presented in **Section 2.7**. The observed bandgap significantly exceeds the values that can be obtained in double InAs/GaSb CQWs (about 3-5 meV) and is comparable to the bandgap in non-strained HgTe/CdHgTe QWs. In addition, the results obtained in this paper show that the bandgap in the sample under study does not change with temperature, which together with high value implies an increase in temperature of edge transport observation.

2.5 Terahertz spectroscopy of two-dimensional semimetal in strained InAs/GaSb/InAs TQW

This paragraph presents the magnetoabsorption studies of in fields up to 16 T in symmetric InAs/GaSb/InAs TQWs grown on the AlSb buffer with a band structure corresponding to the transition between 2D TI and semimetal states. So far, the experimental studies of InAs/GaSb/InAs TQWs have been conducted only on the samples grown on a GaSb buffer. The same buffer was used in the first of

the structures studied in this thesis. In spite of the fact that the obtained bandgap value of 16 meV is record-breaking and maximum for heterostructures with binary TQWs, it is possible to achieve even greater bandgap in stressed structures [42]. At the same time, the growth of strained structures implies the use of other buffer layers to increase the mismatch between the lattice constants of the buffer and the active region. The measurements presented here serve as a basis for further studies of the TQWs with strained layers in order to increase the bandgap of the structure.

Studies of the structure v2554 demonstrate the ability to manipulate the energy spectrum of InAs/GaSb/InAs TQWs by changing the strain in the layers of the active region, which can be realized through the growth of heterostructures on buffers made of different materials. As one can see, from the **Table 1**, the thicknesses of the layers in the TQW of structures v2561 and 2554 are commensurable (14/34 ML and 14/37 ML for InAs and GaSb layers correspondingly). At the same time, the effect of the applied strain strongly modifies the band structure of the sample. **Figure 15** shows the dependence of the position of the bottom of hole-like conductivity subband (H1) and the side maxima of the electron-like valence subband (E1) depending on the strain in InAs layers (ε_{InAs}). The widths of the InAs and GaSb layers were chosen to be 37 and 14 ML, respectively The band structure of three-layer TQWs was calculated by S.S. Krishtopenko using an 8-band Kane Hamiltonian, taking into account the effects of embedded stress in the layers. It should be noted that the strain in the GaSb layer (ε_{GaSb}) is related to ε_{InAs} through a lattice constant of the buffer layer used for the growth of the heterostructure and was also taken into account in the calculations. The method and details of the calculation can be found in Ref. [42].

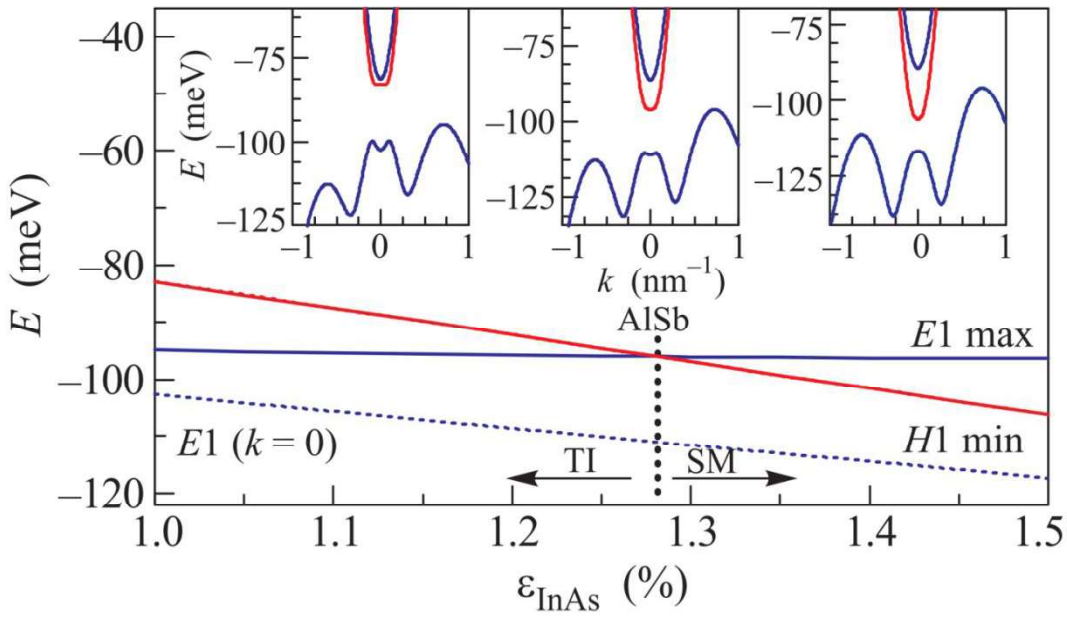

Fig. 15. Calculated position of the minimum of the hole-like conduction subband H1 and the side maximum of the electron-like valence subband E1 in the three-layer InAs/GaSb/InAs QW with the inverted band spectrum versus the strain ε_{InAs} in InAs layers. The width of the InAs and

GaSb layers reflect the studied sample and are equal to 37 and 14 monolayers, respectively. The critical strain corresponding to the phase transition between the 2D TI and SM phases is reached for the AlSb buffer. The insets show the typical band structure of three-layer QWs for values of ε_{InAs} 1% (left), 1.28 % (middle, corresponds to the AlSb buffer), and 1.5% (right). Courtesy of S. Krishtopenko et al.

With the increase of strain (ε_{InAs}) the energy of the side maxima located along the [110] directions increases relative to the energy of the valence subband at $k = 0$. At the critical value of the strain, the energy of the lateral maximum becomes equal to the energy of the bottom of the conduction subband and TQW becomes gapless. Further increase of ε_{InAs} results in a semimetallic band structure with nonlocal overlap between conductivity subband H1 and valence subband E1. According to the calculations, the critical strain value should be realised in the studied sample.

Experimental studies of magneto-absorption spectra were conducted using Fourier spectroscopy in Faraday geometry in magnetic fields up to 16 T at the temperature of 2 K. The concentration of 2D electrons for the same experimental conditions, determined from the analysis of magnetotransport, was equal to $5.6 \cdot 10^{11}$ cm^{-2}. Magnetotransport measurements (Shubnikov-de Haas oscillations and Hall effect in van der Pauw geometry) were carried out simultaneously with the recording of the MA spectra. This was achieved by soldering 4-point contacts along the edges of the sample outside of the optical path.

Figure 16 (a) shows the fanchart of calculated LLs for the studied sample in magnetic fields up to 16 T. Black broken curve illustrates the shift of Fermi level depending on magnetic field. In the course of MA experiments it is possible to observe only the transitions from LLs below the Fermi energy, determined by the value of electron concentration in the sample, to free LLs above the Fermi energy. In our sample because of the high concentration of electrons Fermi level lies deep in the conduction band and transitions from LLs belonging to H1 and E1 subbands are visible only in magnetic fields above 12 T.

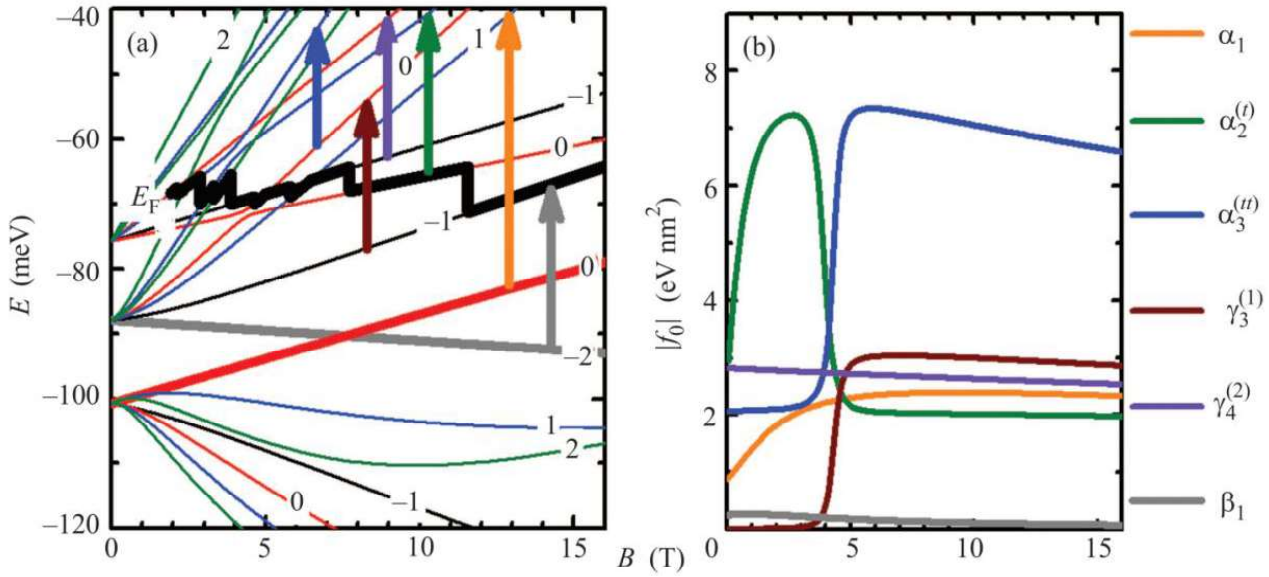

Fig. 16. (a) Calculated Landau levels in the E2, E1 and H1 subbands. The thick lines show the zero-mode Landau levels with level indices –2 and 0. The broken curve shows the position of the Fermi level. The vertical arrows show the most intense allowed transitions between Landau levels. (b) Oscillator strengths for transitions represented by coloured arrows in panel (a) versus the magnetic field. Courtesy of S. Krishtopenko et al.

In the situation of three tightly spaced subbands: E2, E1, H1 the number of transitions that meet the general selection rule for Faraday configuration (Δn = ± 1) is quite large. Therefore, to identify the observed lines, we have performed theoretical calculations of oscillator strengths f_{osc} (**Eq. 4**) for all transitions with Δn = ± 1 with the indices n = -2, -1, ..., 2, possible at given electron concentration (Fermi level).

The values of oscillator strengths as a function of the magnetic field for the most intense transitions between Landau levels are shown in **Figure 16 (b)**. The transitions themselves are represented by coloured arrows in **Fig. 16 (a)**. Other transitions correspond to significantly lower oscillator strengths (lower or comparable to the transition β_1). We can see that the most intense transitions between Landau levels correspond to the CR in E2 ($\alpha_2^{(t)}$ and $\gamma_4^{(2)}$) and H1 ($\alpha_3^{(t)}$ and $\gamma_3^{(1)}$ subbands), and interband transition α_1. In structure v2554, as in structure v2561, the interband transitions between Landau levels from E2 and H1 subbands are practically prohibited in Faraday configuration for all n.

The measured magnetoabsorption spectra in the investigated sample are presented as a colour map in **Fig. 17**. The coloured lines show theoretical dependences of the energies of "allowed" transitions vs. the magnetic field. The solid part of each curve represents a range of magnetic fields, in which the described transition should be observed at a given position of the Fermi level. The arrows mark the values of the magnetic fields corresponding to the integer LL filling factor ν.

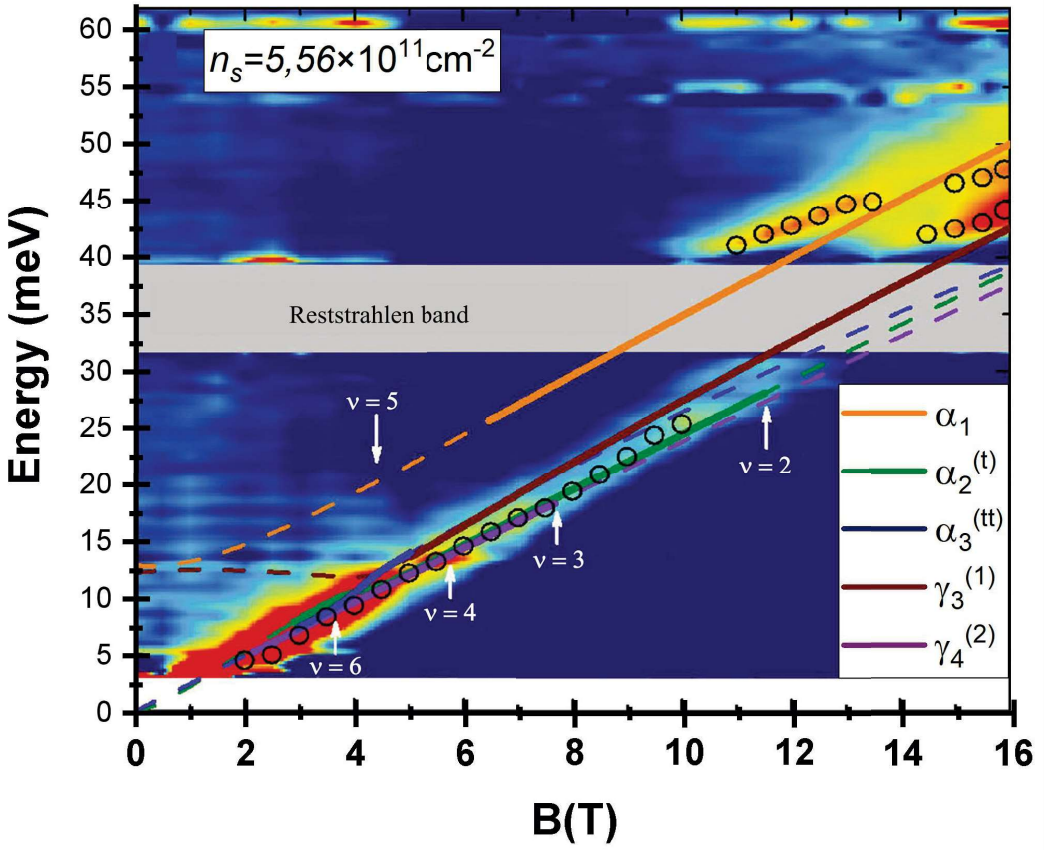

Fig. 17. Magnetoabsorption spectra presented as a colour map and the energy of allowed transitions versus the magnetic field. The gray region corresponds to the *Reststrahlen* band in the GaAs substrate. The white arrows indicate the magnetic fields corresponding to the integer filling factors (*v*) of Landau levels. Courtesy of S. Krishtopenko et al.

We can see that in the small fields in the magneto-absorption spectra, there is a single line associated with the CR-transitions in E2 and H1 subbands. The absence of splitting of this line indicates a small difference of cyclotron masses at the Fermi level in two conductivity subbands. In magnetic fields above 10 T in spectra, a second line of absorption appears higher in energy. It is associated with the interband transition α_1, and its energy also has a linear dependence on the magnetic field. As noted in **Section 2.3**, the high-energy line in the magneto-absorption spectra associated with transition α_1 is the evidence of the inverted band structure of three-layer InAs/GaSb/InAs TQW. The deviation from the linear dependence near the region of *Reststrahlen* band for both lines is due to the change in the profile of the absorption lines in the sample associated with resonance features in the GaAs substrate and is unrelated to the absorption in the TQW itself. The obtained agreement between experimental values of transition energies for both lines in the MA spectra and the results of theoretical calculations confirms the predicted critical parameters between TI and SM band structure of the sample under study.

2.6 Magnetooptical studies of strained InAs/GaInSb/InAs TQW with high bandgap

As the structure v2554, the third examined structure was grown on a buffer layer of AlSb, but in the centre of the TQW these was not a layer of GaSb, but GaInSb with 35% In content. As it was shown in the work of Akiho et al. [40], the use of stressed GaInSb layers enables significant increase of the bandgap of asymmetric CQWs achieved in structures with thinner QWs. Similarly, in TWQs the use of thinner layers (24 and 10 ML in the structure V2808 vs. 34 and 14 ML in the structure V2561 for the outer layers of InAs and the inner GaSb or GaInSb layer respectively) allows us to increase the bandgap without breaking the structure inversion. **Figure 18 (a)** shows calculated band structure and fan chart of LLs of Sample v2808. According to calculations, the bandgap of this sample is equal to 38 meV, while the distance between E1 and E2 subbands is 10 meV. Interestingly, higher bandgap of sample v2808 also leads to "more parabolic" carrier dispersion, which denotes that effective mass approximation describes the dispersion in wider range of wavevectors compared to sample V2561 (See **Fig. 9**). A related effect can be seen in the evolution of LLs with magnetic field (**Fig. 18(b)**) and they demonstrate almost linear behaviour away from the anticrossing points.

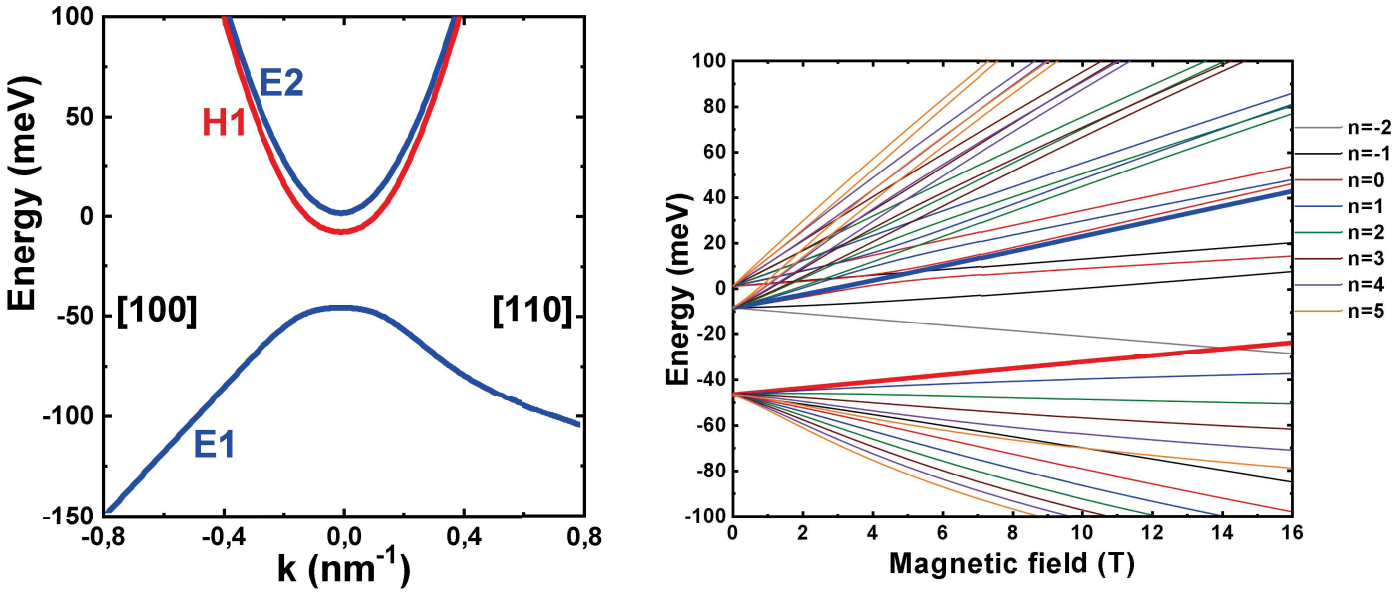

Fig. 18. a) Band structure of sample v2808 and b) of Landau level energy calculations for indices from *n* = -2 to *n* = 2 calculated by S. Krishtopenko. Numbers in brackets in panel (a) denote crystal directions. Figures in the right part of panel (b) denote LL indices. LLs supposed be involved in observed interband absorption transition are indicated by bold curves. Courtesy of S. Krishtopenko

Figure 19 (a) shows the magneto-absorption spectra of structure v2808 at T=10 K. The positions of transitions between LLs are marked by dots. As can be seen, the results are qualitatively similar to those of structure V2561 (See **Fig. 11, 12**). At low magnetic fields, we observe a single absorption line

corresponding to multiple intraband transitions. In magnetic fields above 7 T above the *Reststrahlen* band there appears in a line corresponding to inter-band transitions.

Since the oscillator strength for different transitions is weakly dependent on the presence of structure strain (Compare **Fig. 13** and **Fig. 15**), we associate the observed interband line with transition α_1. As discussed earlier, the presence of an intense interband transition on the spectra indicates the inverted order of the bands of the investigated structure. As in the case of sample V2561, due to the high concentration of electrons, we cannot trace the energy of the interband transitions to the point of zero magnetic field. On the other hand, contrary to sample v2561 for sample v2808 we are able to estimate the bandgap of the structure by extrapolating the energy of α_1 to zero magnetic field due to near-linear dependence of LL energy. It should be noted, however that although the energy of LLs is almost linear, the observed absorption line is not straight and has distinct features

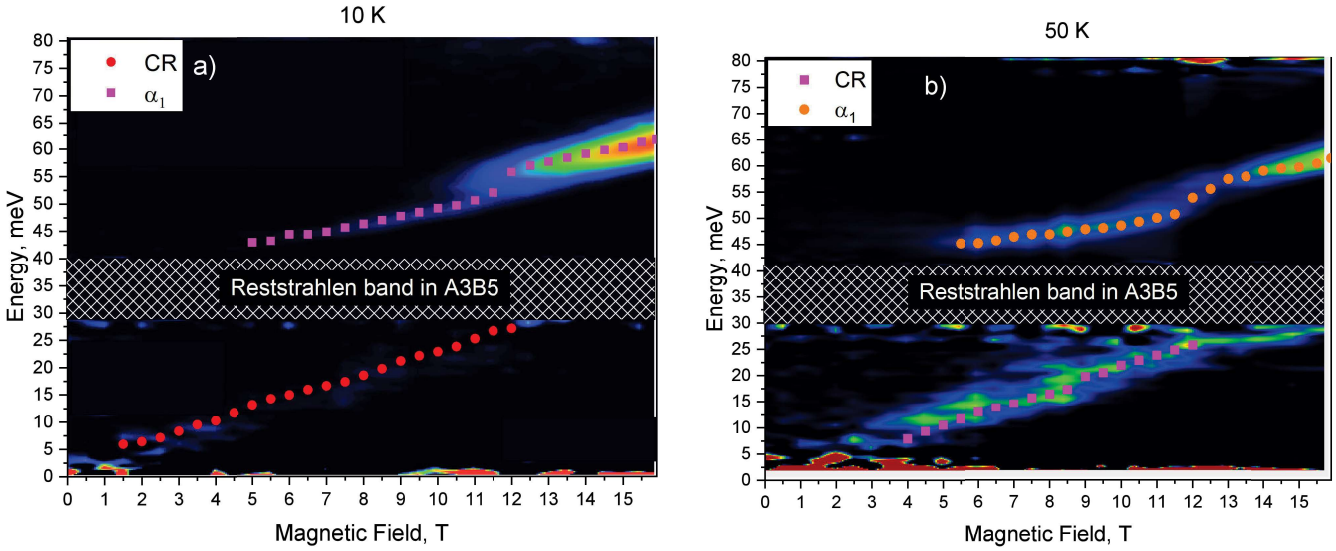

Fig. 19. Spectra of magneto-absorption of the structure V2808 at a) 10 K and b) 50 K presented as a colour map. The positions of absorption line maxima are marked with symbols.

As its energy of approaches the *Reststrahlen* band, the absorption line bends outwards to higher energies. As it was already discussed in **Section 2.1** bending of the line can be explained either by electron-phonon interaction or is an optical artefact coming from the singularity of dielectric function of the sample. The difference between two cases is that bending of the absorption line for sample is more pronounced at higher temperature, while in sample v2561 is virtually disappears at 100 K. It might be explained by the different changes in Fermi level position for these two samples which speaks in favour of the polaron hypothesis as dielectric function is more robust to the changes in band structure of the sample.

Secondly, in magnetic fields above 11 T the absorption line breaks and while its amplitude rapidly increases. The origin of first effect can be understood from the fanchart of LLs (**Fig. 18 (b)**). As one

can see, at magnetic field of 14 T the initial level of transition α_1 (n = 0) crosses LL (n = -2). At the same time, as in HgTe QWs these zero-mode LLs experience anticrossing instead of crossing [50,51,60]. For I $A_{III}B_V$ heterostructures LL anticrossing previously could not be observed, because due to smaller bandgap the point of anticrossing corresponded to lower magnetic fields, at which the transitions from zero-mode LLs were not visible.

Despite being intensively studied for over 8 years, the origin of anticrossing is still a subject of discussion. The most common hypothesis associates it with bulk inversion asymmetry of HgCdTe, but as a recent study reports [61] there is strong evidence that it is a fundamental multyparticle effect. The fact that similar anticrossing was observed in $A_{III}B_V$ heterostructures can have a significant impact on the ongoing discussion, but lies outside the scope of this work.

In order to minimize the impact of discussed effects the bandgap was determined by extrapolating the energy of the interband transition in the range from 7 to 11 T to zero magnetic field. Resulting value that we obtained at 10 K is equal to 35 meV and is in good agreement with theoretical value. The results at 50 K (See **Fig. 19(b)**) are less reliable due to smaller range between the polaron effect and anticrossing point, but at equal magnetic fields the energy of the maximum of interband transitions at two temperatures deviates by less than 2 meV, which suggests that for strained structures the bandgap is temperature independent analogously to non-strained TQWs.

Thus, the results of MA of strained TQWs show that such structures have larger bandgap compared to both the TQW without strain and strained DQWs. Obtained value is in good agreement with theory, hence it confirms the predicted dependence of the band structure on the parameters of heterostructure and suggests that in future experiments it would be possible to achieve the theoretical maximum of the bandgap equal to 60 meV [42].

2.7 Photoluminescence of InAs/GaSb/InAs heterostructures

2.7.1 Photoluminescence method

In the course of PL measurements, the sample is exposed to intensive external radiation, which is in our case provided by IR laser or mid IR parametric oscillator. If the photon energy is larger than the energy of allowed optical transitions in the structure, than as the radiation passes through the structure, some of the photons get absorbed generating non equilibrium electron-hole pairs. When non-equilibrium carriers recombine they emit radiation which is then registered by the detector.

Spectral analysis of PL signal allows extracting the energy of optically active states of semiconductor structure. Generally, PL spectroscopy can be performed in two configurations. For the first configuration the luminescence is registered at one or several selected frequencies, while the spectrum is recorded depending on the wavelength of excitation. This method is called

photoexcitation spectroscopy. The term PL spectroscopy usually denotes the other way of measurements, when the excitation is performed at fixed frequencies and the PL spectrum is measured.

In this work we carried out PL spectroscopy in the spectral window from 5 to 40 μm. In this range, in order to perform PL spectroscopy one needs to consider several fundamental limitations.

First, the probability of interband optical transitions decreases with decreasing the band-gap. This affects both the sensitivity of the detectors, and luminosity of the studied structures. Secondly, the peak of the background radiation lies in the mid-IR range. The highest intensity of black-body radiation at room-temperature is located at 10 μm, so the PL signal from the sample at a given frequency is often smaller than background illumination. Therefore, direct PL measurements under continuous wave excitation are possible only for exceptionally bright and narrow spectral lines, whereas for wider and less intensive spectra it is necessary to decrease the ratio between the signal and the background achieved through modulation techniques. In this work we used the method adapted from [62]. The efficiency of this method was demonstrated in the previous experiments on the bulk MCT structures and single wells [63–65]. The scheme of the PL set-up can be found in **Fig. 20**.

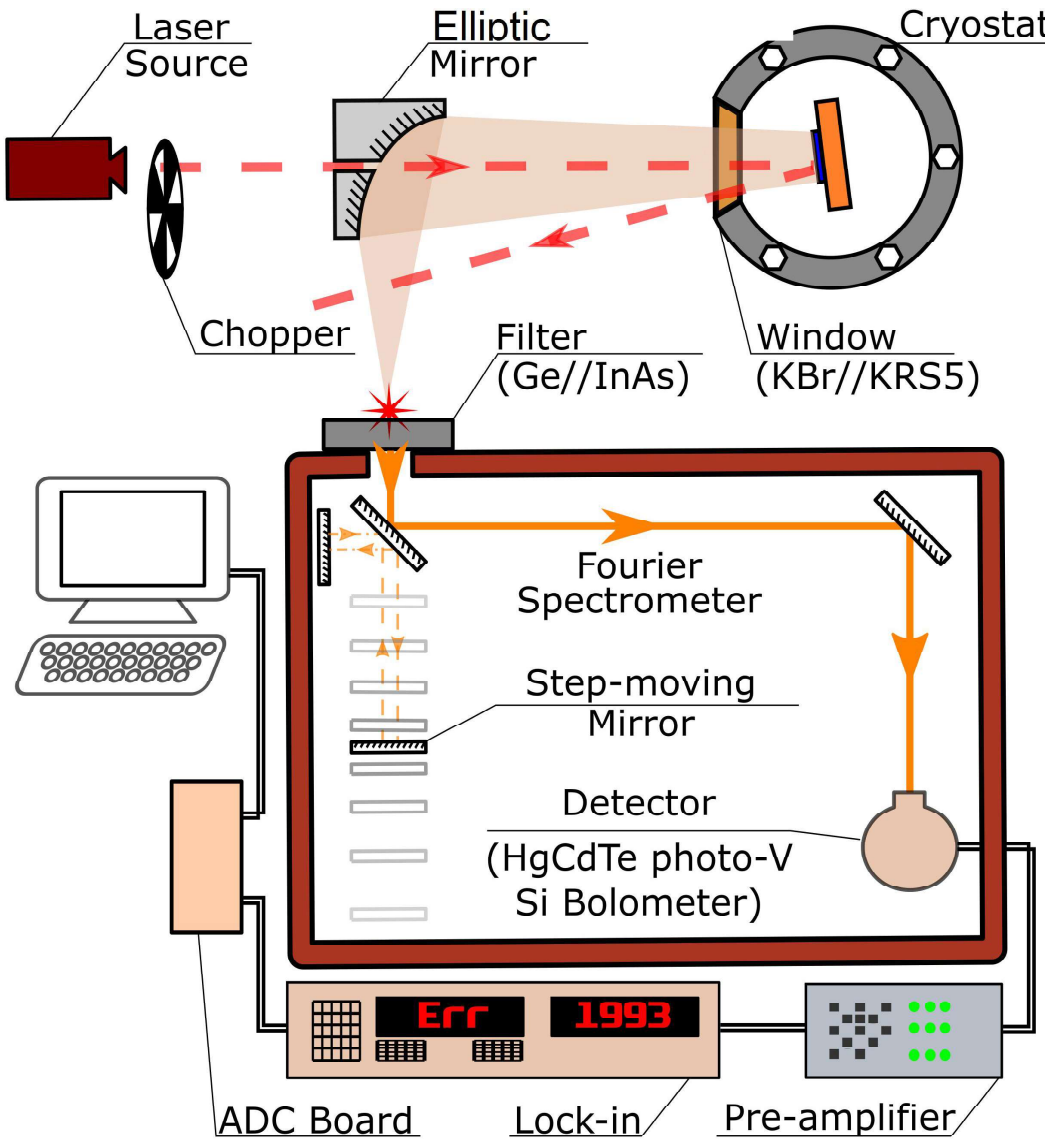

Fig. 20. Sketch of the experimental set-up for PL measurements.

During the PL measurements sample was mounted on a cold finger of a closed-cycle cryostat with the temperature range from 10 to 300 K. Excitation was performed from the top of the structure by either pulsed source or continuous wave laser with mechanical modulation. The beam spot of the pumping source was covering the whole sample.

For spontaneous PL, the sample was excited by a continuous-wave laser coupled to mechanical chopper. The laser beam was guided through the hole in a parabolic mirror, which was then used to collect the radiation from the surface of the structure. The second focal point of the mirror was aligned with the optical system of the spectrometer to provide good translation of the signal.

The angle between the sample and the incident beam was slightly offset from the normal to prevent directly reflected excitation beam from entering the spectrometer. The rest of the scattered pumping

radiation was cut-off by optical filter placed inside or in front of the window of the spectrometer. For the most of the PL experiments we used a bulk semiconductor plate of either InAs or Ge. These semiconductors have high absorption in near IR range and are almost transparent in the studied spectral region. More details on the combination of the used filters and beam-splitters can be found in **Table 2.**

Table 2. Combinations of beam-splitters and filters used for the PL spectroscopy measurements depending on the range under study.

Spectral range	Beam-splitter	Filter
600-5000 cm^{-1}	KBr	Ge
400-27000 cm^{-1}	KBr	InAs
180-600 cm^{-1}	Mylar multilayer	KRS-5
<180 cm^{-1}	Mylar multilayer	Polyethylene

The optical system of the spectrometer was adjusted so that the input window served as a radiation source. After that we directly measured the transmission of the empty optical path. As a result, we obtained the emission spectrum of the sample, modulated by function of the detector, filter and beam-splitter used. In order to separate emission features of from the response of the system, additional spectra were recorded with the same optical elements, but using a broadband source without sharp spectral features, for which purpose the built-in Globar lamp was used.

In order to minimize the noise, the signal from detector was output straight to the voltage amplifier ("Stanford Research Systems" SR-560). This amplifier also served as a filter to effectively cut off the powerful low-frequency noise generated by the electromagnetic and vibration of closed-cycle cryostat. The filters of the amplifier were set to isolate the modulation frequency e.g. for the modulation at 2 kHz the filters were set to 1-3 kHz. The signal from the amplifier was passed to Lock-in amplifier for the averaging. Post-amplification recording was performed by the high-speed ADC board. The final processing of the signal was done by dedicated Bruker software. The modulation frequency was determined by the response time of the detector of choice. For the silicon bolometer, the maximum operation frequency is about 1 kHz and in practice, a frequency of 300 Hz was generally used. For the "fast" detectors based on HgCdTe with a time constant of several μs, higher modulation frequency was chosen for better detuning from intense low frequency noise. If fact, it was limited by the mechanical chopper and was approximately 2 kHz.

2.7.2 Photoluminescence results on the InAs/GaSb/InAs heterostructures

As noted above, energy gaps between the subbands E2, E1 and H1 at B = 0 can be extracted by THz PL spectroscopy. In the case of inverted trilayer InAs/GaSb/InAs QWs, both interband PL between conduction and valence subbands (H1-E1, E2-E1) and intersubband PL between two conduction subbands (E2-H1) can be observed. Radiative transitions between the subbands are possible, because, contrary to bilayer InAs/GaSb QWs, trilayer structures have a direct bandgap. The bottom of the conduction band and the top of the valence band lie at the same point of momentum space, and the energy difference between them is lower than the energy of optical phonons in InAs and GaSb, which prevents intensive non-radiative recombination of the carriers.

When absorbing a high-energy photon, an electron from the valence band transits into the conduction band, leaving a vacant place in the valence band. In other words, an electron-hole pair is generated. Then the electron and the hole independently relax to their quasi-equilibrium state near the extremum of the corresponding subband. Reaching the top of the valence band, non-equilibrium hole can recombine with an electron close to the bottom of the conduction subband by either radiative or non-radiative recombination process.

During the experiments, the temperature in the cryostat was varied from 20 to 50 K. As long as the energies of the transitions in studied samples lie in the far-IR range, we used polyethylene filter and silicon bolometer as a detector. The experiment was carried out using quasi-continuous pumping. A continuous Ti:sapphire laser operating at 800 nm wavelength served for an optical excitation of the structure. The output power of the source could be varied from 10 mW to the maximum of 300 mW. However, the results showed that varying the pumping power does not lead to any spectral changes, therefore, for the most experiments we were using the maximum available excitation power in order to maximize the signal.

An important detail of the experiment is the use of "45 degrees" geometry - in this case, the sample is set at the angle close to 45° with respect to the incident radiation and the line connecting the sample with the focusing mirror. By using this geometry, the resulting PL spectrum contains emission lines averaged by the polarization of both the pumping and emitted radiation.

The PL spectra for temperatures 20 and 50 K, measured at an excitation power of 300 mW, are shown in **Figure 21**. The insert shows the oscillator strength of optical transitions between the subbands E2, E1 and H1 as a function of a quasimomentum in the direction (110).

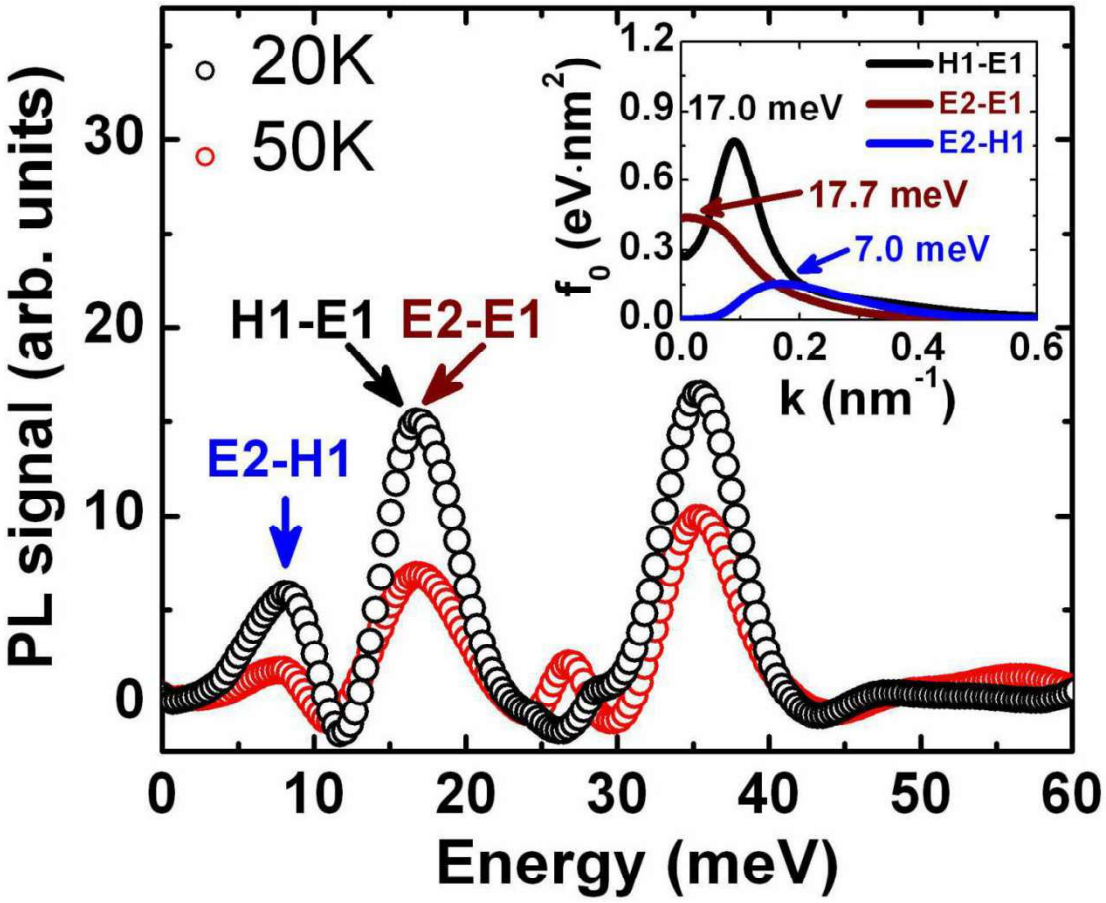

Fig. 21. THz photoluminescence spectra at different temperatures measured in "45 degree" geometry. The insets show calculated for the experimental conditions. oscillator strength $f_0 = \hbar^2 \overline{f_{osc}} / 2m_0$ for optical transitions between E2, E1, and H1 subbands. The overline denotes an averaging over orientation of the polarization component lying in the QW plane. The numbers correspond to the transition energies at maxima of f_0.

The spectra obtained under tilted pumping radiation show three well resolved emission lines. The high-energy line seen at about 35 meV corresponds to the luminescence of Ga antisite defects in the GaSb buffer [66,67]. The energy of the most long-wavelength line is 7.5 meV. Its position well matches the energy corresponding to the maximum value of the oscillator strength of transition from E2 to H1 subbands, thus we suppose that it can be attributed to such transition. At the same time it should be noted that the maximum of oscillator strength is reached at non-zero *k* when E2 and H1 subbands almost merge, thus it is probable that the line at 7.5 meV has a different nature, and can be caused by transitions involving impurity states. The middle PL line has the energy of 16.5 meV and is formed by the superposition of the interband transitions H1-E1 and E2-E1. Since the E2 and H1 bands lie very close in energy, the energy of the maximum oscillator strength for these transitions differs by less than 1 meV. Therefore, we cannot fully resolve them in PL spectra. Note that the observed transitions E2-H1 and E2-E1 are active when polarized along the growth axis, while the transitions E1-H1 are mainly active when polarized parallel to the QW plane.

The figure also demonstrates that the temperature increase up to 50 K does not change the position of the emission lines for transitions between subbands E2, E1 and H1. This means that the energy gaps between them do not depend on temperature, which is consistent with the results obtained using the MA spectroscopy.

PL spectrum of structure v2554, measured at 20 K is shown in **Figure 22 (b).** A weak high-energy line with the energy of 35 meV corresponds to the luminescence of structural defects in GaSb layers. The ratio of the amplitudes of impurity line and PL lines corresponding to the transitions between subbands in a QW is much smaller than for sample v2561. It results from two factors: first, the structure v2554 is grown on the AlSb buffer, thus the luminescence comes only from the thin layers, grown on top of the structure in the superlattice and in the TQW. Second, the low energy PL line in **Fig. 22 (b)** consists of two components whose parameters can be determined by adjusting the form of the experimental line (open symbols) with two Lorentz functions (solid and dot curves). To identify the transitions responsible for the formation of such a PL signal, we used the calculations of the oscillator strength f_{osc} for dipole transitions between E2, E1, and H1 subbands depending on the wave vector in the QW plane (**see Fig. 22(c)**).

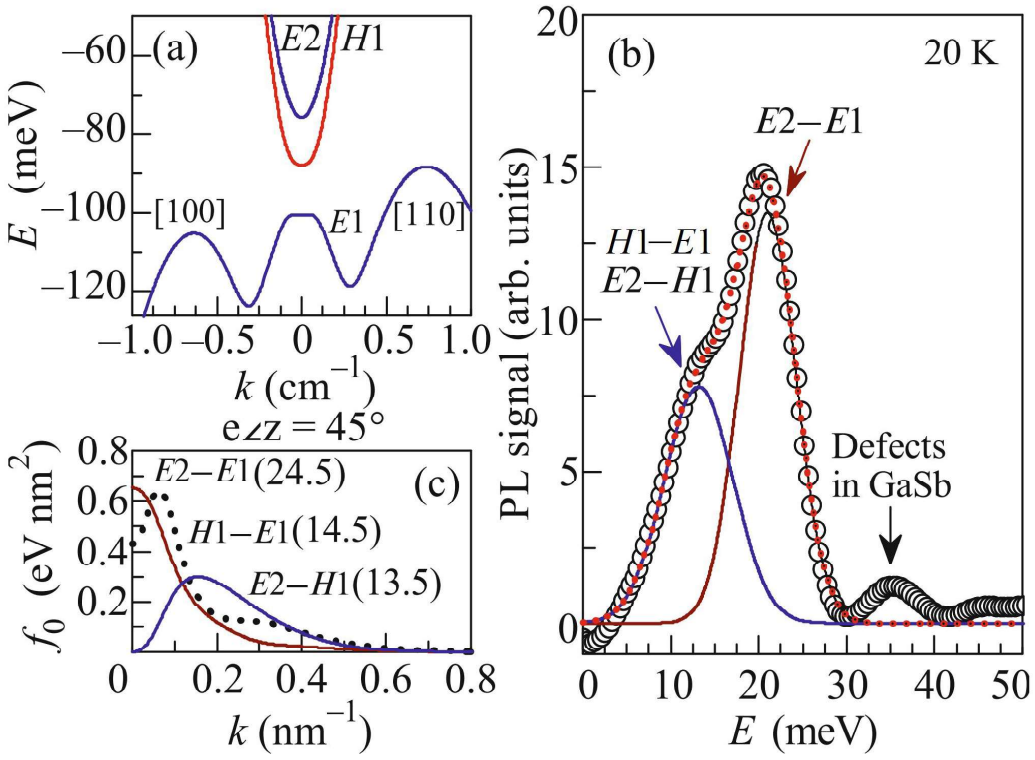

Fig. 22. (a) Band structure of the sample. Energy–momentum relations in electron-like (E1, E2) and hole-like (H1) subbands are presented by blue and red curves, respectively. (b) (Open symbols) Photoluminescence spectrum and (solid and dotted curves) two-Lorentzian fits to the line profile. (c) Oscillator strengths for electric dipole transitions between subbands versus the quasimomentum along the [110] crystallographic direction. The numbers in parentheses

are the energies of the maximum oscillator strength in meV. The dotted curve corresponds to the transition not observed in the PL spectrum of the sample under study.

The position of the right PL line (**brown curve, Fig. 22(b)**) agrees well with the energy corresponding to the maximum value of oscillator strength for the transition between the subbands E2 and E1. The position of the left PL line (**blue curve, Fig. 22(b))** matches the energy for two transitions (E2-H1 and H1-E1) at once.

Calculations of oscillator strengths f_{osc} for possible transitions (See **Fig. 22(c)**) suggests that the left PL line corresponds to transition E2-H1, while the PL line of transition H1-E1 is absent in the spectrum. It is due to the fact that the ratio of amplitudes of the PL lines corresponds to the ratio of oscillator strengths for transitions E2-E1 and E2-H1. The absence of H1-E1 PL line in the spectrum would mean the existence of a non-radiative recombination channel associated with the overlap of the conductivity band H1 and the valence band E1 in momentum space. The latter is correlates with the fact that PL lines corresponding to all three transitions E2-E1, E2-H1 and H1-E1 are observed in sample v2561 in which the overlap of bands H1 and E1 is absent.

At the same time it should be noted that the intensity of the PL is determined not only by the oscillator strength, but also by the energy distribution of non-equilibrium carriers in the subbands. Magnetotransport measurements indicate that for studied structure Fermi level lies deep in the conduction band, thus the states in H1 subband are occupied and intraband transition is prohibited. From this point of view H1-E1 transition is more plausible, but transport measurements are to be used cautiously as were done in different experimental conditions. Moreover, as in the case of sample v2561 the origin of the low-energy line can be related to the transitions involving impurity centres.

Thus, the definitive conclusion of the origin of the low-energy PL line on the basis of the PL studies performed in this work can not be made. On the other hand, the measurements of the THz PL spectra made it possible to observe the emission lines associated with the transitions E2-E1 between the size quantization subbands for both studied samples. Comparison of amplitude of the observed PL lines with theoretical calculations of oscillator strength for inter- and intra-band transitions suggests existence of a non-radiative recombination channel caused by the overlap of the conduction and valence bands for sample with semimetallic band structure.

In conclusion, we have measured THz PL and MA spectra in the InAs/GaSb/InAs heterostructure grown on AlSb substrate with a band structure corresponding to the transition point between the states of two-dimensional TI and a semimetal. Lines corresponding to the transitions between dimensional confinement levels were found in PL spectra. The results of the magneto-absorption spectra confirm the gapless band structure of the investigated quantum wells InAs/GaSb/InAs. These results are published in Ref. [68]

2.8 Summary

In conclusion, we have for the first time measured MA and PL spectra of heterostructures with triple quantum wells InAs/GaSb/InAs and InAs/$Ga_{0.65}In_{0.35}Sb$/InAs with inverted band structure.

Our results demonstrate that the study of combination of PL and MA spectra containing inter- and intra-band transitions between LLS provides a way to determine both the value of the bandgap and its sign (band ordering) of the heterostructure. The main difference between the normal band ordering and inverted one consists in the behavior of interband transitions in MA spectra which are absent in structures with normal band structure.

The study of magneto-absorption spectra in stressed InAs/Ga(In)Sb/InAs heterostructures grown on an AlSb substrate shows that changes in the composition and thickness of the layers make it possible to tune the band spectrum of the structure from the state of a gapless 2D semimetal to a topological insulator with such a bandgap that is unattainable in InAs/Ga(In)Sb double quantum wells

The measurements of InAs/GaSb/InAs and InAs/$Ga_{0.65}In_{0.35}Sb$/InAs TQWs designed for achieving high value of inverted band confirm the theoretically predicted values of the bandgap and are consistent with the calculations performed within the Kane Hamiltonian 8x8. In MA spectra lines corresponding to both intraband transitions in the conduction band and interband transitions were found, that indicates band inversion. The bandgap of InAs/GaSb/InAs structure determined from the obtained PL spectra is 16. Both PL and MA results confirm that in the temperature range from 2 to 100 K the bandgap of the studied structure remains unchanged. For InAs/$Ga_{0.65}In_{0.35}Sb$/InAs heterostructure the value of the bandgap determined from the MA spectra reaches 35 meV and does not change with temperature. Such structures are promising candidates for experimental demonstration of QSHI state at high temperatures by direct measurements of quantized conductance of the edge channels.

Chapter 3. Topological phase transitions in double HgTe quantum wells probed by magnetoabsorption spectroscopy

3.1 Double HgTe quantum wells: band structure and phase diagram

As already discussed, the band structure of the HgTe/CdHgTe quantum well is rearranged from the normal (CdTe-like) to the inverted as the HgTe width is increased. At the critical width of the QW $d_c \approx 6.3$ nm, the conduction band and the valence band are engaged and carriers have linear (conic) dispersion law similar to a single layer graphene [12].

One can expect similar connection to appear between the HgTe DQWs (two HgTe QWs separated by a tunnel-transparent CdHgTe barrier) and bilayer graphene (BG) [69,70] under certain conditions (See **Fig. 23**). An important feature of HgTe DQW heterostructures is that they allow tuning their band structure by variation of the thickness of the barrier, in the limiting case of infinite barrier reaching the dispersion of a single well.

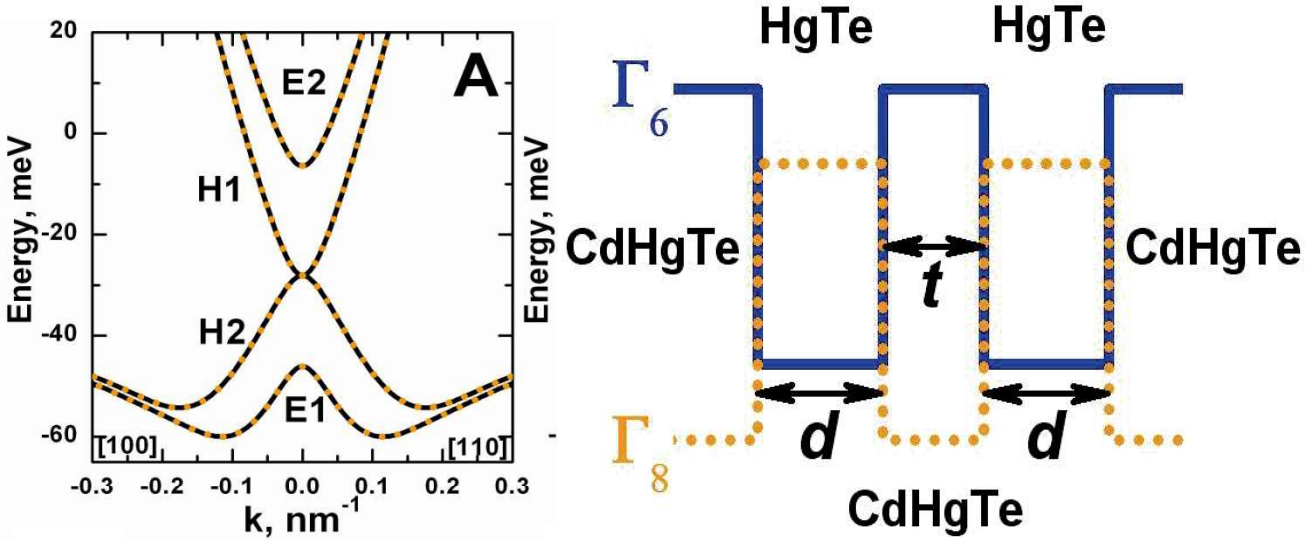

Fig. 23. a) Band structure of the first two electron and hole confinement levels in bilayer graphene phase of HgTe/CdHgTe DQW b) Scheme of mutual position of the bands in HgTe/CdHgTe DQWs

The first theoretical studies of the band-structure of HgTe DQWs were reported in a series of works by Michetti et.al. [71–73]. The first work [71] was focused on practically important feature of DQW, its sensitivity to the external electric field. The authors demonstrated that applying a sufficiently strong vertical electric field makes an inversion of the bands possible: a hole-like subband H1 "related" to one QW gets higher in energy than an electron-like subband E1 related to another QW, even if the individual quantum wells have normal band structure ($d_{QW} < d_c$), i.e. there is a topological phase transition. In subsequent works [72,73] they introduced the concept of a topological field-effect-transistor based on this

effect (See **Fig. 24**) and analyzed possible applications to a spin battery and formation of novel time reversal symmetric topological exciton condensate state, coined the helical topological exciton condensate.

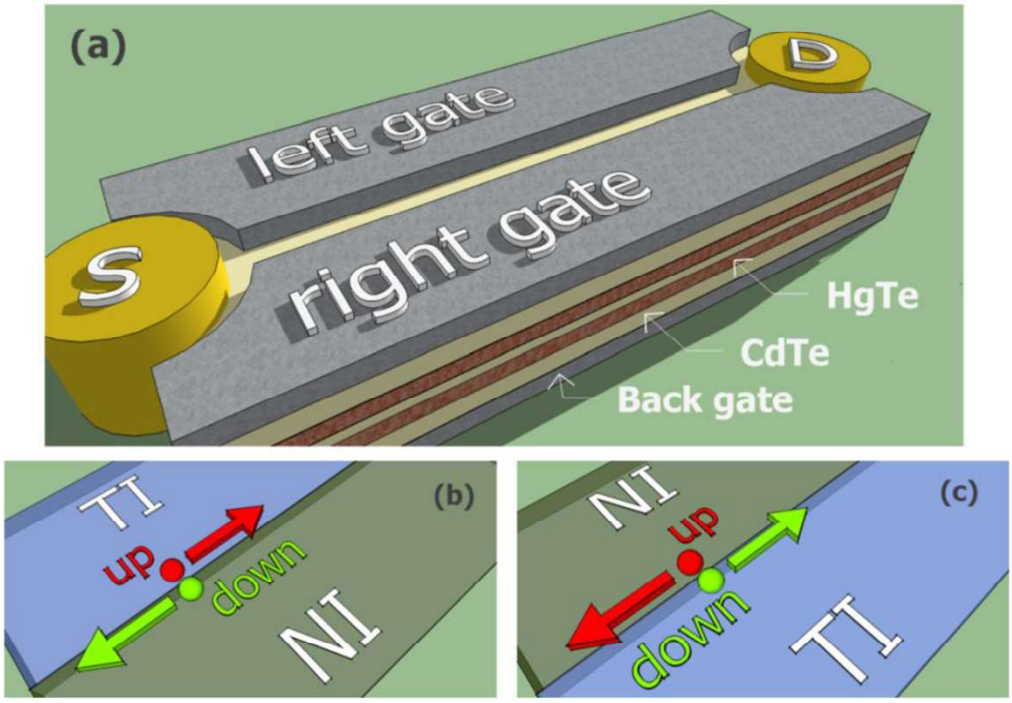

Fig. 24. Isometric sketch of a HgTe/CdTe DQW device with a back gate and two distinct top gates (left and right). In the ON state, top gates induce a gate-bias domain leading to a TI/NI interface (channel) where helical edge modes are found. Source (S) and drain (D) leads, placed along the interface between L and R top gates, collect charges from the edge modes. The lateral surface of the DQW is specifically treated to ensure negligible edge trans- port. (b) Schematic description of a TI/BI interface for direct gate polarization with indication of the helical spin transport of edge states. (c) Reverse gate polarization leading to opposite spin transport of the channel. Adapted from [72]

Another step in theoretical studies of the band structure of HgTe DQWs was made in our group [45]. Calculations of the band structure were performed on the basis of the eight-band Kane model similar to the one described in **Chapter 2** used for the InAs/GaSb/InAs TQWs. Interaction between the conduction band Γ6 and the valence bands Γ8 and Γ7 was considered exactly while the interaction with the other bands was taken into account by perturbation theory. Such an approach allows one to calculate correctly the nonparabolicity of the size-quantized subbands, the spin-orbit interaction, and the value of the built-in elastic deformations. The calculation of the wave functions was carried out by the method described in Ref [74]. Material parameters were taken from Ref [75]. The essence of the calculation method consists in considering a superlattice with a sufficiently long period instead of an

isolated DQW. In this case the tunnelling of the charge carriers can be neglected and the periodic boundary conditions with period $d_{SL} > d_{QW}$ can be used.

Qualitatively band structure of DQW can be understood from the two limiting cases: when the thickness of the separation barrier t tends to infinity and when it tends to 0. In the first case the QWs are not interacting and energy levels of the DQW are the same as in isolated QWs. In the opposite case when t is close to zero, the energies of the subbands tend to the corresponding values of a single QW of thickness $2d$. Consequently, in both cases the mutual position of electron-like (E1, E2) and hole-like (H1, H2) subbands is governed by the ratio between the thickness of the wells (d) and critical thickness of a single HgTe/CdTe QW. The transition from one case to another occurs due to the increase of the tunnel transparency of the barrier which causes splitting of each pair of subbands into even and odd states. Calculated dependence of the energy of the subbands versus the thickness of the separation barrier t is shown in the top panels in **Figure 25.** Each panel illustrates particular scenarios. **Figure 25 (a)** corresponds to $d_c/2 < d < d_c$ while **Figure 25 (b)** corresponds to $d > d_c$, where d_c is the critical thickness for a single QW.

In the first case shown in **Fig. 25 (a)** the thickness of a QW lies between d_c and $d_c/2$. This implies that at infinitely thick barrier the system has non-inverted band structure (subband E2 is located above the H2 and the subband E1 lies higher in energy than the subband H1). When the barrier between the wells gets thinner the energy of E1 subband decreases, while that of H1 practically does not change. It results from the fact that splitting of electron-like states is much greater than the splitting of hole-like states. This is associated with a significant difference in effective masses in electron- and hole-like subbands at $k = 0$, the values of which determine the tunnelling transparency of the barrier. At specific value of t the gap in the band spectrum collapses and new gapless state is formed that resembles a bilayer graphene. For this state valence and conduction bands are formed by two parabolic subbands H1 and H2 touching at the point $k = 0$. When the thickness of the separation barrier gets smaller, the splitting of the subbands H1 and H2 becomes apparent, i.e. the gap opens and system becomes QSHI, as is the case for single HgTe QWs.

The second case of non-trivial band ordering shown in **Fig. 25 (b)** is realized for $d_{QW} > d_c$. In this case, E1 subband always lies below H1 and phase of the system is regulated by the mutual position of E2 and H2 subbands At small thickness of the separation barrier E2 subband lies above H2 but as it increases they engage. This leads to the formation of a Dirac cone at **Γ** point (so does the intersection of E1 and H1) and topological phase transition.

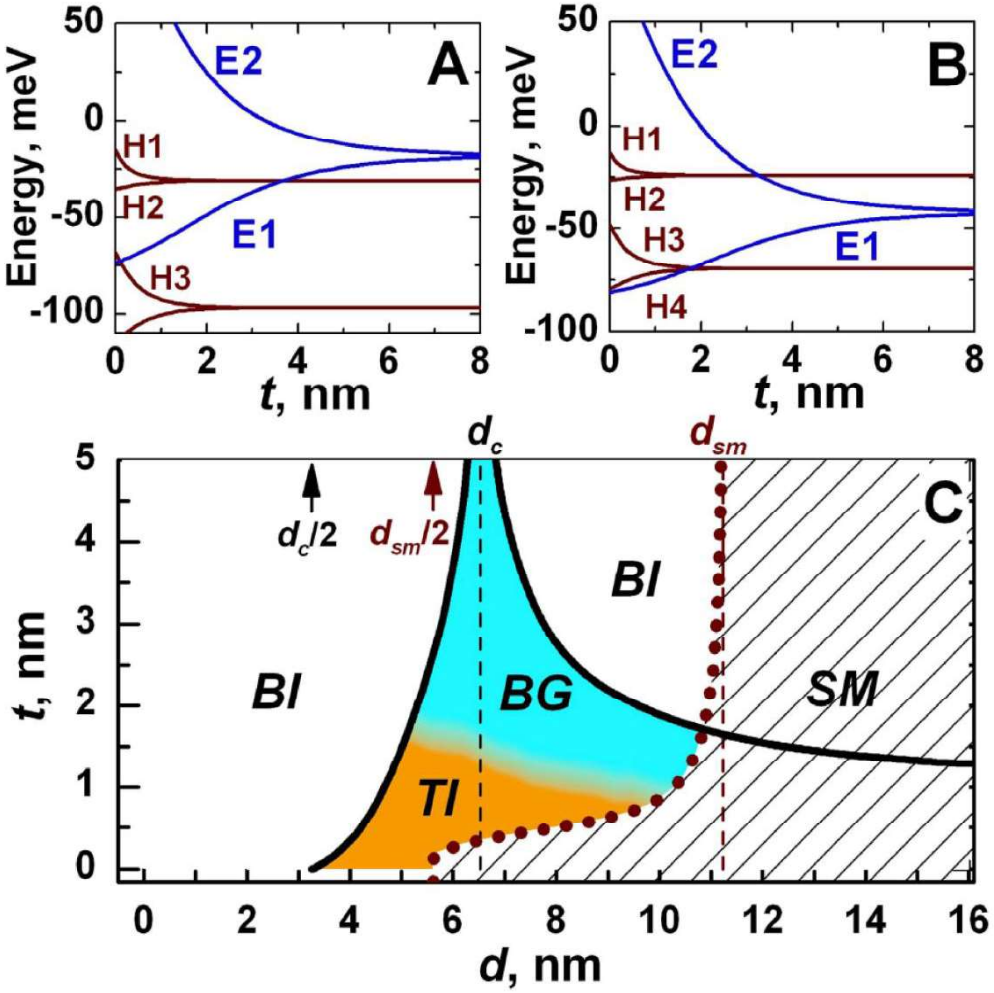

Fig. 25. (A,B) Energy of E1, E2 (both in blue) and H1, H2 (both in red) bands at k = 0 versus barrier thickness t at different quantum well thickness d: (A) $d_c/2 < d_{QW} < d_c$ and (B) $d_{QW} > d_c$. (C) Phase diagram of double HgTe QW. The values d_c and d_{SM} correspond to thickness of the single QW, at which Dirac cone and semimetal phase arise respectively. The white-open regions are the band insulator phase, while the white-striped region corresponds to the semimetal phase, when the side maxima of valence subband exceed the bottom of conduction subband. The orange and blue regions conform to topological insulator and BG phase, respectively. The bold black curves correspond to the arising of the Dirac cone at the Γ point. The scales of DQW and t in the phase diagram can be efficiently increased by changing x and y in the alloys of $Hg_yCd_{1-y}Te$ / $Cd_xHg_{1-x}Te$ DQWs. Picture taken from Ref [45]

A phase diagram of symmetric HgTe/CdHgTe DQWs constructed as a function of the thicknesses of the HgTe QWs (*d*) and tunnel-transparent barrier (*t*) made of CdHgTe is shown in **Figure 25 (c).** Thick black lines correspond to the appearance of Dirac cones at the Γ point. The left and right lines correspond to the intersection between the E1 and H1 and between E2 and H2 subbands respectively. If the thickness of the separation barrier is sufficiently small, then the subbands H1 and H2 are separated, and the inversion of the subbands E1 and H1 leads to a topological phase transition

between the states of the trivial insulator (band insulator, BI) and TI (orange area in **Figure 25 (c)**). For wide enough QWs, the system transits into a SM state corresponding to the hatched region in **Figure 25 (c)**. SM band structure is characterized, as in the case of a single QW for $d_{QW} > d_{SM}$, by non-local overlap between the side maxima of the valence band and the minimum of the conduction band. The abovementioned gapless state of the "two-layer graphene" (bilayer graphene, BG) corresponds to the blue region in **Fig. 23 (c)**. Its lower blurred boundary is determined, in fact, by the splitting conditions of H1 and H2 subbands when the separation barrier becomes tunnel-transparent for hole-like states.

Thus, depending on the parameters of the quantum wells and the barrier between them, the structure can be in several topologically non-equivalent states. Besides the phases typical for the single HgTe/HgCdTe QWs (See **Fig. 4**) the splitting of electron and hole subbands in tunnel coupled QWs induces additional topological phases in double QW heterostructures. Depending on the thickness of the QWs and the barrier between them, this system might be found in three different states. The first trivial case with thin enough QWs corresponds to a normal band structure, when both electron-like subbands lie above the hole-like subbands. The second phase is characterized by dispersion similar to that of BG and has the band ordering of E1<H1<H2<E2. BG phase is appealing from practical point of view as it allows topological phase transition driven by an interlayer bias voltage. The third phase features two pairs of edge states and can be called double inverted (DI) because both hole subbands lie above electron subbands. Although the edge channels in DI phase can not be discovered by direct transport measurements as for the QSHI we tend to believe that double inverted case is different from the trivial BI and can under certain conditions be a higher-order TI (for more detail see Ref [76] and referenced works).

One of the interesting features of single QWs is the possibility to induce phase transition by changing the temperature of the structure [57]. It results from the temperature growth of the energy of the electron subband. In DQWs the band spectrum of the structure changes with temperature in the same way which can lead to a single or double phase transition, as the mutual position of electron and hole subbands is reverted once or twice. Specifically, the structures which are in BG phase at low temperature transition into BI as they are heated while structures with double inversion experience phase transition into BG phase. In order to probe this effect and study the specific features characteristic of DQWs in each phase we performed a series MA measurements in wide temperature range for this type of structures. The experimental set up and parameters are similar to the ones used in **Chapter 2**.

The structures studied in this work were grown by the group of S.Dvoretskii and N.Mikhailov by MBE on semi-insulating GaAs substrates (013) [77]. The structures have a relaxed CdTe buffer about 5 microns thick followed by the active region. Active region is formed by the outer layers of

$Hg_{0.35}Cd_{0.65}Te$ which contain the DQW heterostructure (**Fig. 26**). The surface of the structure is covered with a 50 nm thin layer of CdTe, which serves to stabilise mercury inside the structure. Parameters of the DQWs were calculated in order to achieve desired band structure using the same method as in Ref [45]

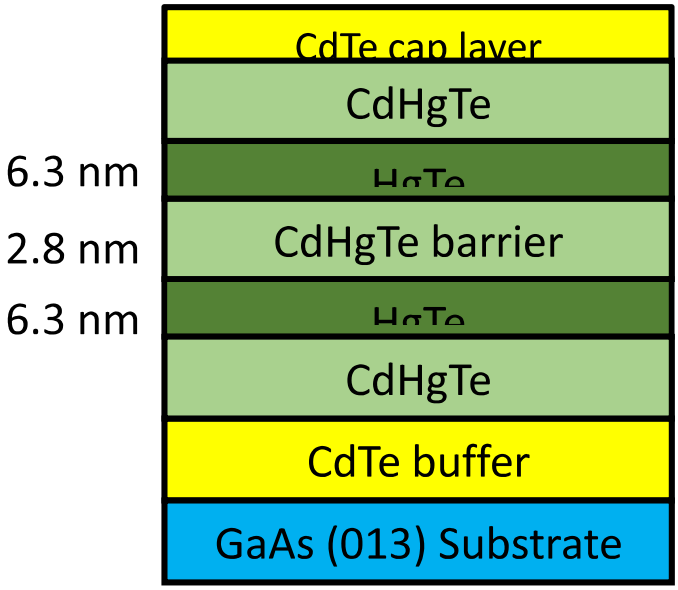

Fig. 26. Growth scheme of the studied structure 150218. Structure 150219 has the same growth scheme, but different thicknesses of HgTe QWs and barrier layer

As long as the main goal of our studies is the probing of temperature induced topological phase transitions, the widths of the layers in DQWs were selected to place temperature of phase transition in the middle of the available temperature range (2 – 120 K). The first structure (150218) has the QW width d = 6.3 nm and the barrier width t = 2.8 nm, which corresponds to BG phase at low temperatures (See **Fig. 25 (a)**). The second structure at low temperatures is in DI phase and has the same barrier but thicker QWs (d = 8.0 nm).

3.2 Temperature-induced topological phase transition between band insulator and topological insulator

The first structure 150218 is designed to experience phase transition between BG and BI as the temperature increases, so the spectra were measured in the full temperature range from 2 to 100 K.

MA pattern reveals a number of transition lines visible in the range from 30 to 700 cm^{-1} (See **Fig. 27 (a)**). Full theoretical description of this picture is not possible as the current theory is not able to quantitatively describe the anticrossing between different LLs. The fact of phase transition, however, can still be seen from the experimental data. For that we suggest approach based on qualitative difference in the structure of the transition lines in TI and BI. For TI state there are two pairs of most intensive transitions – { α, β, α', β'} that are linked to the topological state of the system. In TI

zero-mode LLs experience anticrossing which manifests itself in appearance in absorption spectra near critical magnetic field B_c of transitions α', β_1'. These transitions are "mirrored" to α and β_1 with swapped initial LLs. This effect can be observed if B_c is high enough so that α and β transitions are not forbidden by Pauli principle and the crossing point does not fall in the *Reststrahlen* bands. Unfortunately, in the vicinity of the conditions corresponding to phase transition (when B_c is close to zero) no manifestation of the LL anticrossing can be observed.

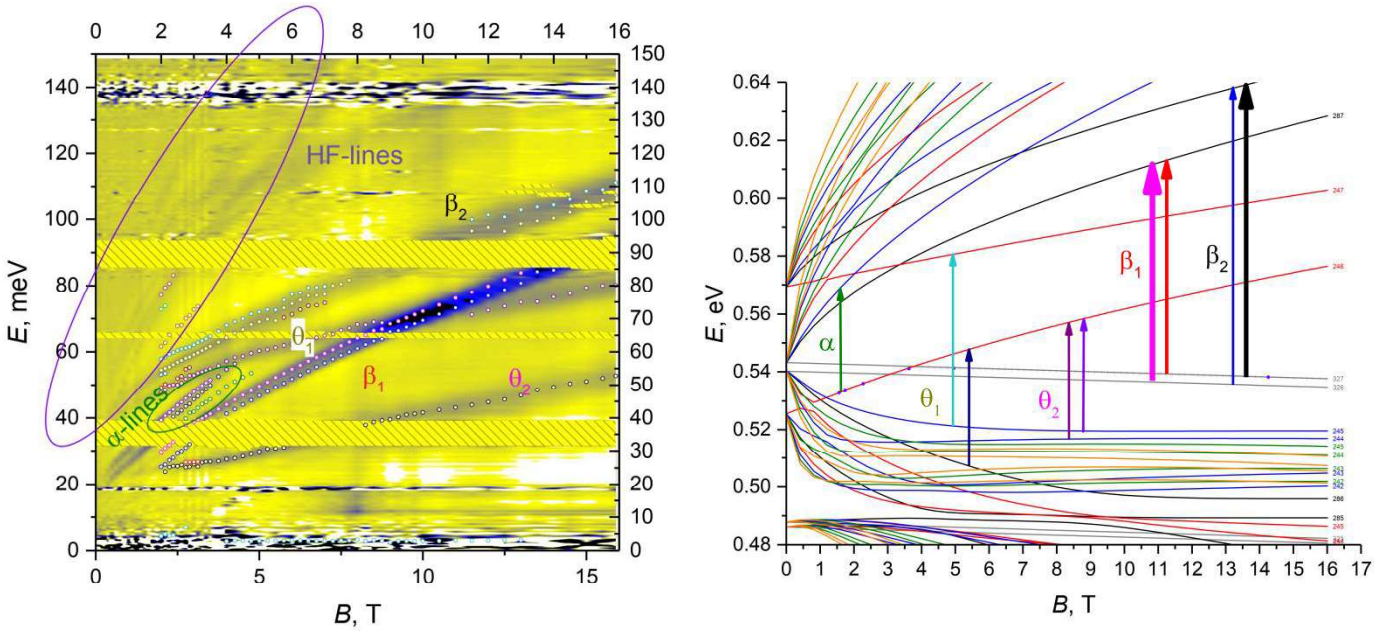

Fig. 27. A) Colour map of the MA spectra of structure 150218 at 2 K in the range of magnetic fields from 0 to 15.9 T. Depending on the intensity of absorption the colour changes from bright yellow to dark blue. Positions of the most intense absorption features observed in spectra are marked by the circles. Distinct absorption lines are labelled with Greek letters. B) Landau level fan chart for the sample 150218 at T = 2 K. Coloured lines represent Landau levels, characterized by different value of n. Vertical arrows with Greek letters represent the observed transitions

Another approach to detect the topological phase is based on analyzing behaviour of α and β_1 lines in high magnetic fields (See **Fig. 27 (b)**). One can see that the energy of lower level of α transition (n = 0) goes up with magnetic field while the energy of upper level of β transition(n = -2) goes down, on the other hand, the energy of upper levels (1 and -1) goes up for both transitions. Thus the energy of β_1 line has higher derivative over magnetic field than the one of α line. Therefore in BI state β_1 line lies above α line and never crosses it. In TI (BG) state β_1 line starts from zero and should cross α line at some point (not equal to B_c). Unfortunately, in the experiment we are not able to observe α line at high magnetic fields, besides the evolution of α and β_1 is affected by the anticrossing between the LLs and the behaviour of α and β_1 lines predicted by simple axial model cannot be observed due to interference with low symmetry effects around B_c and the limitation of maximal magnetic field. At the

same time, above the critical temperature we can clearly see that β_1 line (that has higher slope) lies above α line as expected for BI state (See **Fig. 28 (b)**).

The simplest method of determining topological phase of the system is to measure the cut-off energy of β lines. As the system approaches the point of phase transition from high temperatures cut-off of β line tends to zero energy in low magnetic fields. In the phase which corresponds to the BG or TI state β line becomes intraband transition and its cut-off energy no longer changes. The typical MA spectra corresponding to the temperatures below at and above the temperature of phase transition are shown in **Figure 28**.

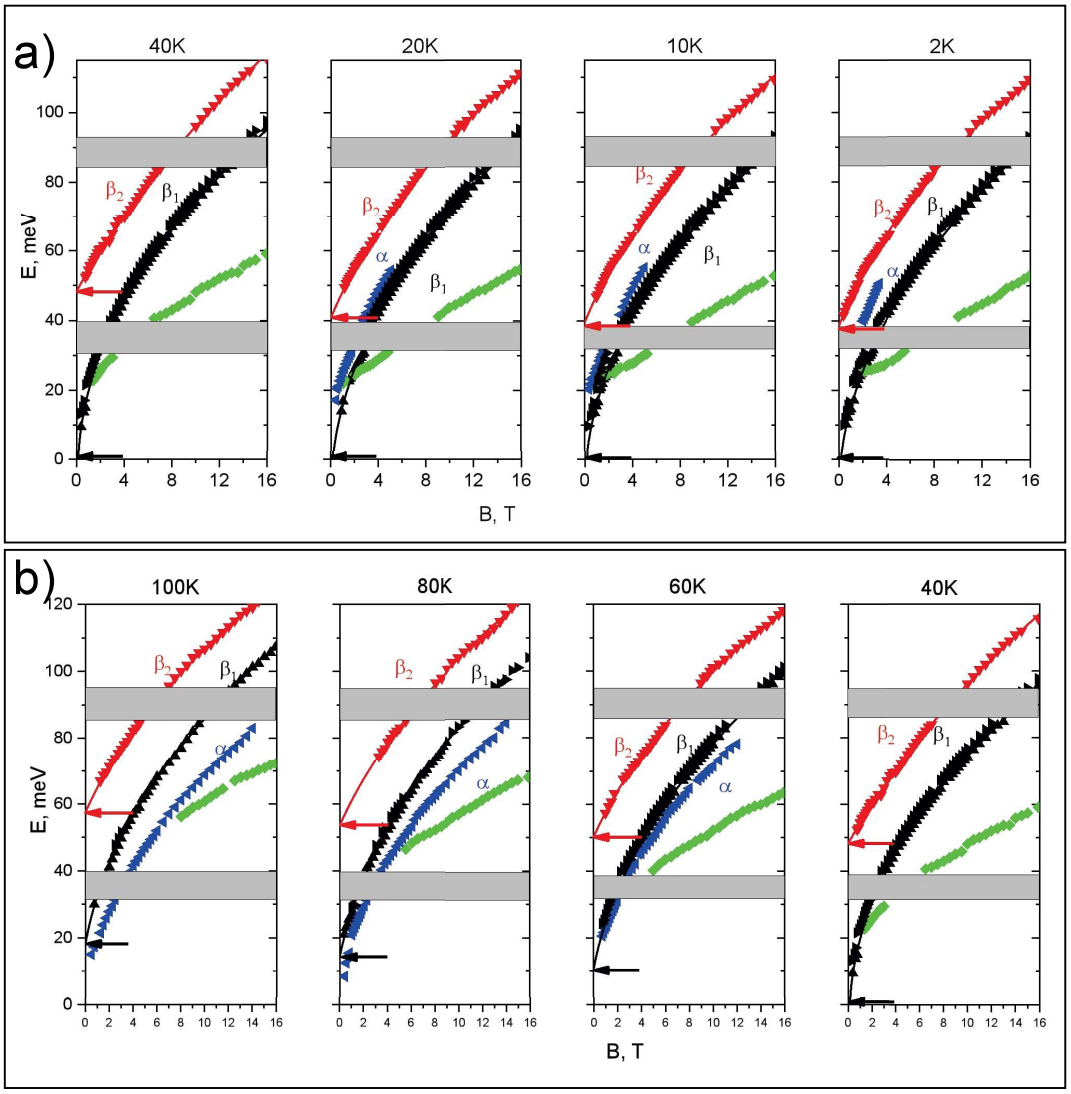

Fig. 28. Temperature evolution of the most intensive magnetoabsorption lines above (a) and below (b) the point of topological phase transition (BG->BI).

According to calculations the phase transition can be indicated by zero-energy cut-off of the absorption line corresponding to the transition between a pair of -2 and -1 landau levels, which was observed at the temperature of 40 K. Above 40 K, the cut-off energy is increasing with temperature

and below this temperature, it remains unchanged which confirms the presence of phase transition at 40 K and correlates well with our prediction.

3.3 Temperature evolution of magnetoabsorption spectra of structure 150219 and double phase transition

The position of sample 150219 in the phase diagram is shown in **Figure 29 (a).** In-situ characterization of the provided by the ellipsometry gives the thicknesses of the QWs *d* equal to 8.4 – 8.5 nm, while the barrier thickness was measured to be *t* = 2.9 – 3.0 nm. The ex-situ characterization of the structure was performed by comparing the energy of allowed inter-LL transitions with the obtained by the calculations and from the experiment. Typical MA spectrum presented as a color map is shown in **Figure 29(b)** .If we compare the observed transitions to the ones obtained for the structure 150218 (**Fig. 27**), we can see that in each case the most pronounced absorption lines are the same. Apart from the absorption lines associated with the main absorption lines *α, β_1* and *β_2* there are several regions which contain valuable information about the band structure in of the sample in magnetic field. First, one can see the region of "high-frequency"-lines, the energy of which quickly grows with the magnetic field. These lines are not intensive compared to the main magnetoabsorption lines however, they become more apparent at higher temperatures and energies. As it was shown in Ref. [78] these lines represent a superposition of multiple interband transitions, thus their full analysis is not done here. The same stands for the absorption lines which lie lower in energy than α, and β lines, which are associated with the intraband transitions in the valence band.

The fitting of the lines was performed using the main absorption lines in high magnetic fields above the points of anticrossing. Calculations were performed using the axial approximation with temperature-dependent parameters of the Hamiltonian. The structure parameters were taken from [75,79] . Dependence of E_g(x,T) was taken from [80] as it proved to fit better the experimental results in the studied structures.

The best agreement was achieved for *d* = 8.0 nm and *t* = 2.8 nm, with the built-in electric field ***E*** = 10 KV/cm. The last value was found after determining the parameters of the QW by fitting the magnitude of the splitting between the *β* lines, which results from the asymmetry of the structure. According to calculations this structure can undergo two phase transitions happening temperatures of 30 and 140 K, thus MA measurements were performed for this structure in the range 2 to 135 K, with the upper boundary determined by the limitations of experimental set-up.

After determining the parameters of the structure using the position of the absorption lines in high fields it is important to trace them across the points of anticrossing and *Reststrahlen* band in GaAs substrate for the coherent description of the behavior of the absorption lines.

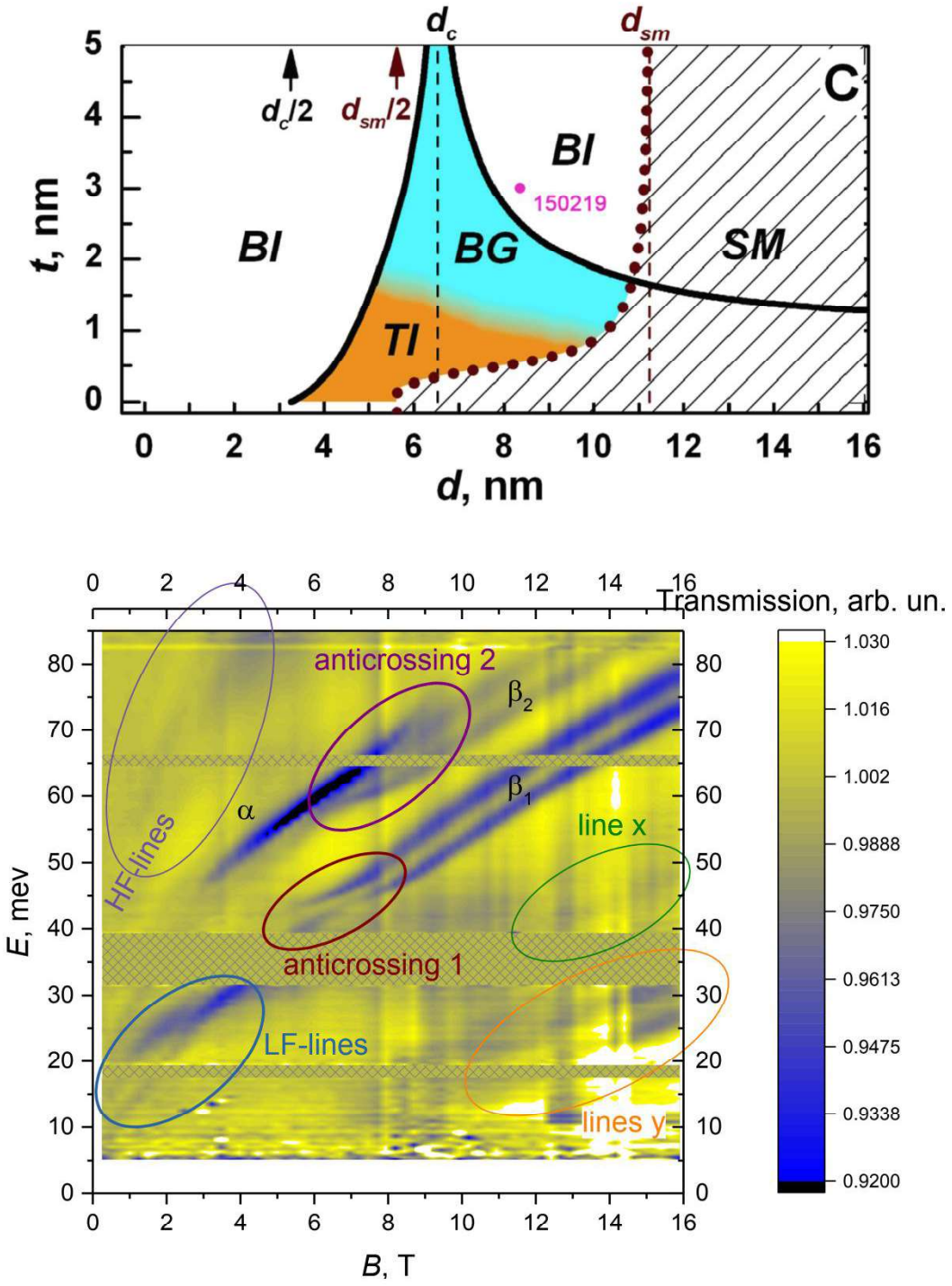

Fig. 29. a) position of the sample 150219 in the phase diagram b) "Colour map" of the observed transitions of sample 150219 at 2 K in the range of magnetic fields from 0 to 15.9 T with circled regions that have special spectral features.

First, we consider the anticrossing between the lines. As it was written previously, this phenomenon is an acute problem and was observed multiple times during the measurements of single HgTe QWs. The same effect can be seen at the measurements of the DQW samples, but the picture of the absorption lines is different in this case. That happens because in the studied structures the degeneracy of the first zero-mode LL (n = 0) is lifted and we observe not one, but two zero-mode LLs,

which participate in the anticrossing. The sketch illustrating the resulting avoided crossings is shown in **Figure 30.**

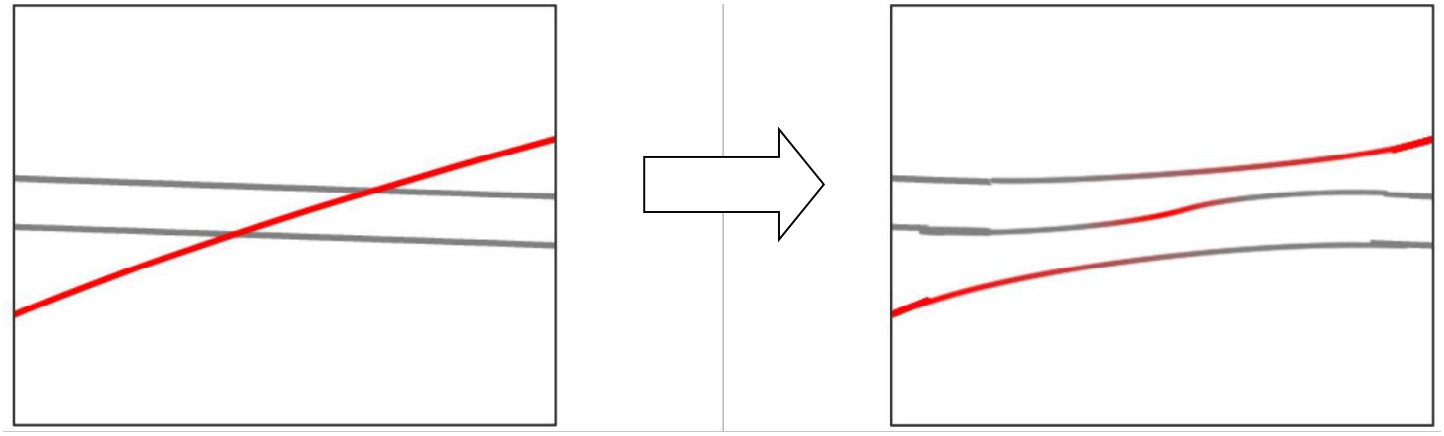

Fig. 30. The scheme illustrating the interaction between the zero-mode Landau levels in the vicinity of the anticrossing point.

This kind of picture can be seen at magnetic field around 7 T for both the β_1 and β_2 transitions, which correspond to transitions from zero mode LL to the first (n = 1) levels of H1 and H2 subbands (See **Fig. 31 (b)**). In the vicinity of the anticrossing point both β_1 lines bend towards high energies which indicates the mixing between the zero-mode LLs. Below the point of anticrossing the lower of the β_1 line (red curve) was not observed due to the depopulation of the corresponding LL. The same avoided crossings picture can be seen for the β_2 lines, however at low temperatures this effect is masked by the superposition of α line. In order to account for the mixing between the LLs we show the energy of the prohibited transition in the vicinity of the anticrossing, which represents the "trajectory" of the bending of the lines.

In order to connect the lines through the Reststrahlen band we analyzed the position of the Fermi level which was roughly estimated by the range of the visibility of high-energy transitions (β_2 lines). This gives us the list of transitions that can be seen in low magnetic fields, which are then matched with the lines above the *Reststrahlen* band.

The calculated fan chart of LL for sample 150219 with parameters derived from the MA data is shown in **Figure 31 (a).** The colour map of the MA spectra with superimposed energies of the most intensive transitions is shown in **Figure 31 (b).** As one can see, the fitting with the used parameters is in good agreement with experimental results. Calculations suggest that the studied sample at low temperatures is in DI state with both hole-like levels above the electron-like levels as it is manifested by two crossing between LL at B_{c1} = 1 T and B_{c2} = 7 - 8 T. At the same time, the abovementioned crossings at low magnetic field are not visible in the MA spectra due to the position of the Fermi level in conduction subband.

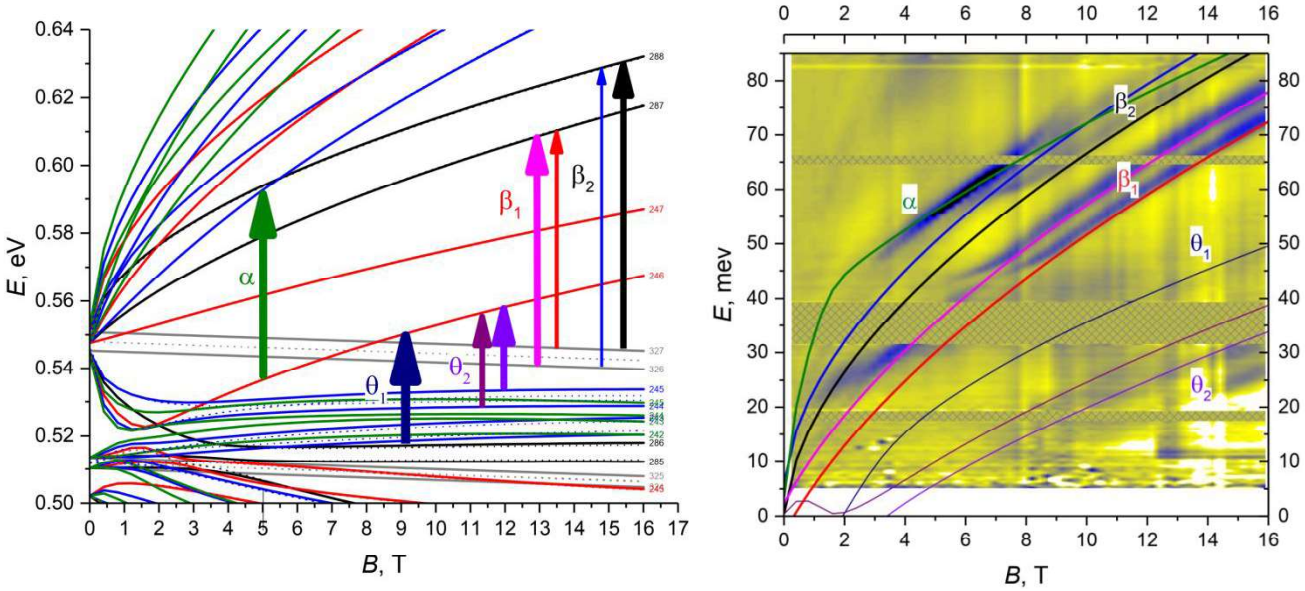

Fig. 31. a) Landau level fan chart for the sample 150219 at *T* = 2 K. Coloured lines represent Landau levels, characterized by different value of n. Vertical arrows with Greek letters represent the observed transitions. b) False colour map of the transmission of sample 150219 at *T* = 2 K as a function of energy and magnetic field with superimposed energies of the transitions shown in panel a). The maximum absorption corresponds to the blue color. Dashed regions indicate the regions of the opacity of the optical path.

As the temperature increases the MA picture becomes more sparse. We observe two pairs of β lines, α line and tree low-energy lines: Θ_1, which corresponds to transition from the upper -1 level to 0 level, and a pair of two Θ_2 which corresponds to transition between levels 1 and 0 (See **Fig. 32(a)**)

At 20 K α-line extends to higher magnetic fields (~9 T), than at *T* = 2K. Although the energy of α line is close to the energy of the β_2 lines it can be distinguished from them because it is noticeably narrower. In the region of the low fields it appears that all the main absorption lines are visible in wider range which indicates the upward shift of the Fermi level. As a result, both β_1 lines clearly extend into the low frequency field. There is also a hint that the upper β_2 line exists in the same range. LL fan-chart calculated for *T* = 20 K (**Fig. 32(a)**) shows that the band structure of the sample is still DI, however, the first critical field B_{c1} which flips the inversion between the first pair of LLs is less than 0.25 T and is not observed in the MA spectra.

On the other hand, the second critical field B_{c2} above which the band structure of the sample becomes normal clearly manifests itself by double anti-crossings observed both for the pair of β_1 and α lines. Interestingly, the shape of the lines around the anticrossing point is different for two types of transitions and matches the illustration shown in **Figure 30**. For the first anticrossing observed in line β_1 (bottom area, near β_1' line), the line in the middle disappears, while for the second anticrossing (top area, near α' line) it is, on the contrary, the strongest. This is determined by the "main" LL, which

participates in the transition. When it is the LL with index 0, transition is the weakest in the middle (β_1), and when it is LL with index -2, it is the highest. It is worth mentioning, that in the area of the second anticrossing there is also an anticrossing connected with the transition β_2, but it is noticeably weaker, so we mainly see the transitions to level n = 1.

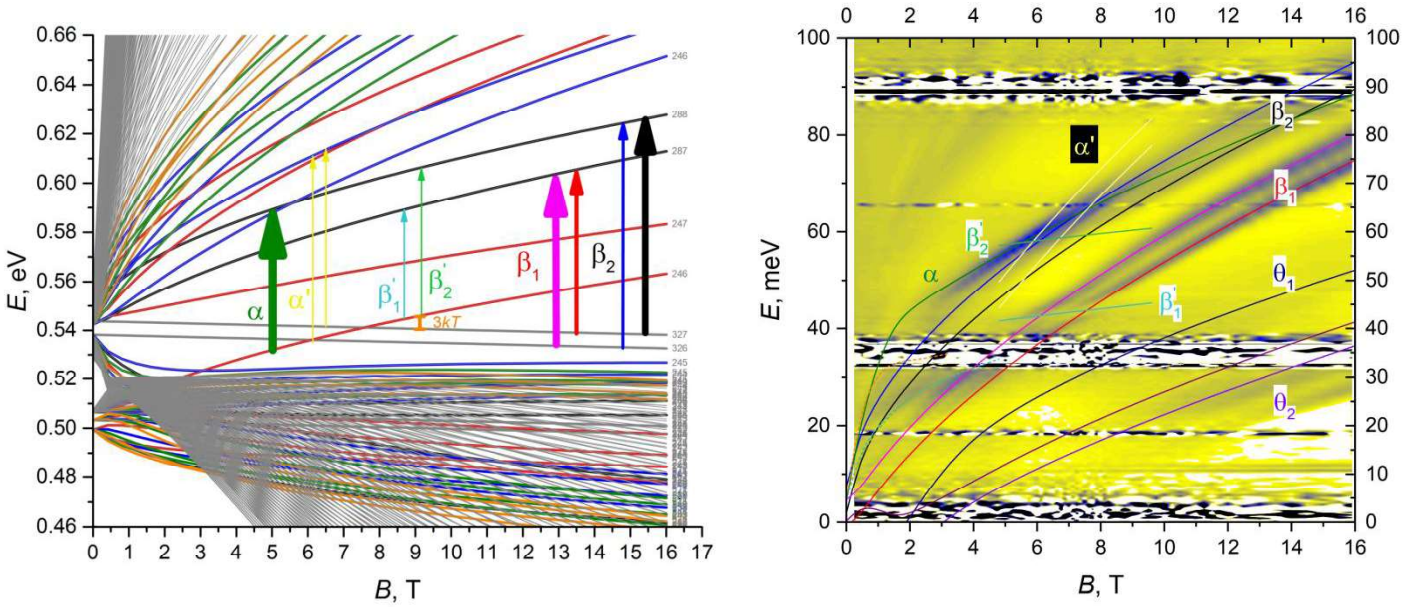

Fig. 32. a) Landau level fan chart for the sample 150219 at *T* = 20 K. Coloured lines represent Landau levels, characterized by different value of n. Vertical arrows with Greek letters represent the observed transitions. Orange arrow shows the energy the carrier can acquire by thermal activation. b) False colour map of the transmission of sample 150219 at *T* = 20 K as a function of energy and magnetic field with superimposed energies of the transitions shown in panel a). The maximum absorption corresponds to the blue color. Dashed regions indicate the regions of the opacity of the optical path.

At T = 30 K (**Fig. 33**) the system undergoes the first temperature-driven topological phase transition. Above this temperature the band structure of the DQW features one inversion between the electron- and hole-like levels and correspond to the phase of BG. At the same time the studied structure is not gapless because the built-in electric field opens the gap in spectrum and makes the system topological insulator.

Above 30 K and up to 80 K the increase in temperature leads only to quantitative changes of the MA spectra. First, α transition is getting visible in both regions of high and low magnetic fields. The upper limit is determined by the value of $3kT$, which can be used to estimate the range that can be populated by thermally activated carriers from the filled LL below the initial LL level of α. The start of α line is in good agreement with the point of the crossings between LLs of the first valence band with indices n = 0 and n = 1 at 3 T. Such agreement is not unique to this temperature and suggests that Fermi energy is pinned to this level at small magnetic fields.

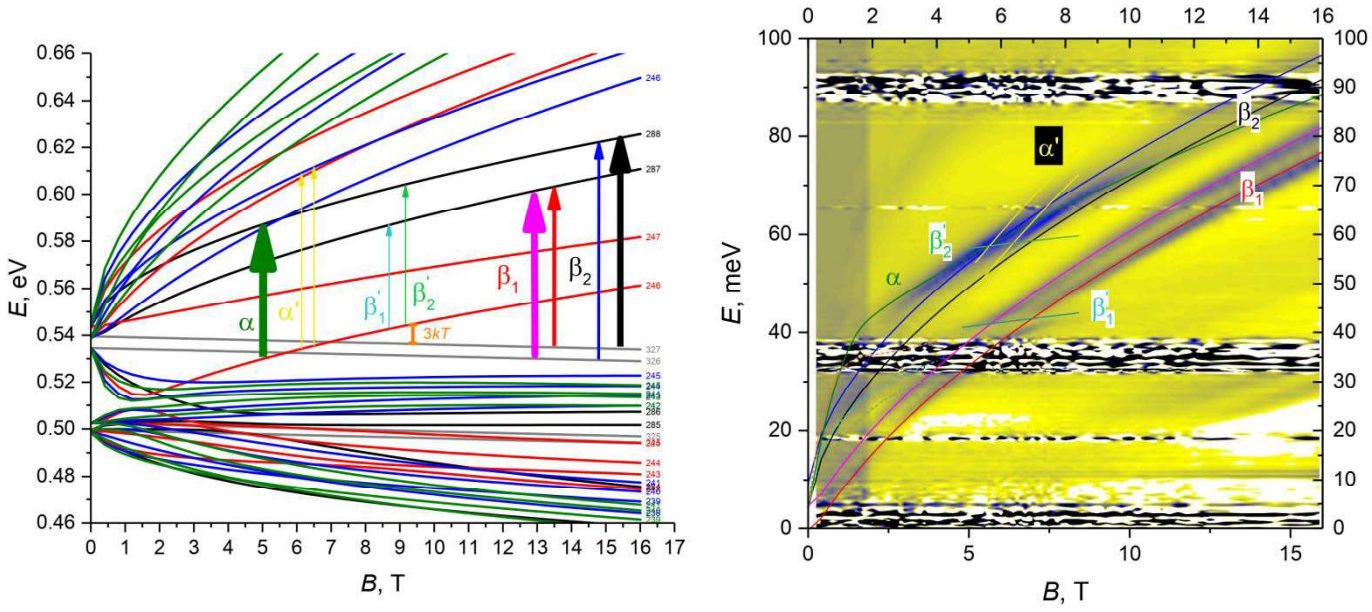

Fig. 33. a) Landau level fan chart for the sample 150219 at *T* = 30 K corresponding to the point of phase transition. Coloured lines represent Landau levels, characterized by different value of n. Vertical arrows with Greek letters represent the observed transitions. Orange arrow shows the energy the carrier can acquire by thermal activation. b) False colour map of the transmission of sample 150219 at *T* = 30 K as a function of energy and magnetic field with superimposed energies of the transitions shown in panel a). The maximum absorption corresponds to the blue colour.

At T = 80 K (**Fig. 34**) the Fermi level is shifted in the conductivity subband. We observe several intraband transitions in the conduction band (lines *γ* and α^2). The line *α* starts from the 1.5 T and can be seen up to maximum magnetic field. In weak fields we observe classical CR of electrons with cyclotron mass equal to 0.0126 m_0. The disappearance of γ line at $B \sim 4.5$ T allows estimating the carrier concentration in the conditions of the experiment ($n = 2.1 \cdot 10^{11}$ cm^{-2}). At such concentration transitions associated with β_1 lines are not active at magnetic fields below 3 T when the upper level of the transition is filled up. β_2 line can be traced down to low magnetic field, and although the exact cut-off energy at zero field can not be found, it is clearly seen that they tend to non-zero value analogously to the sample 150218.

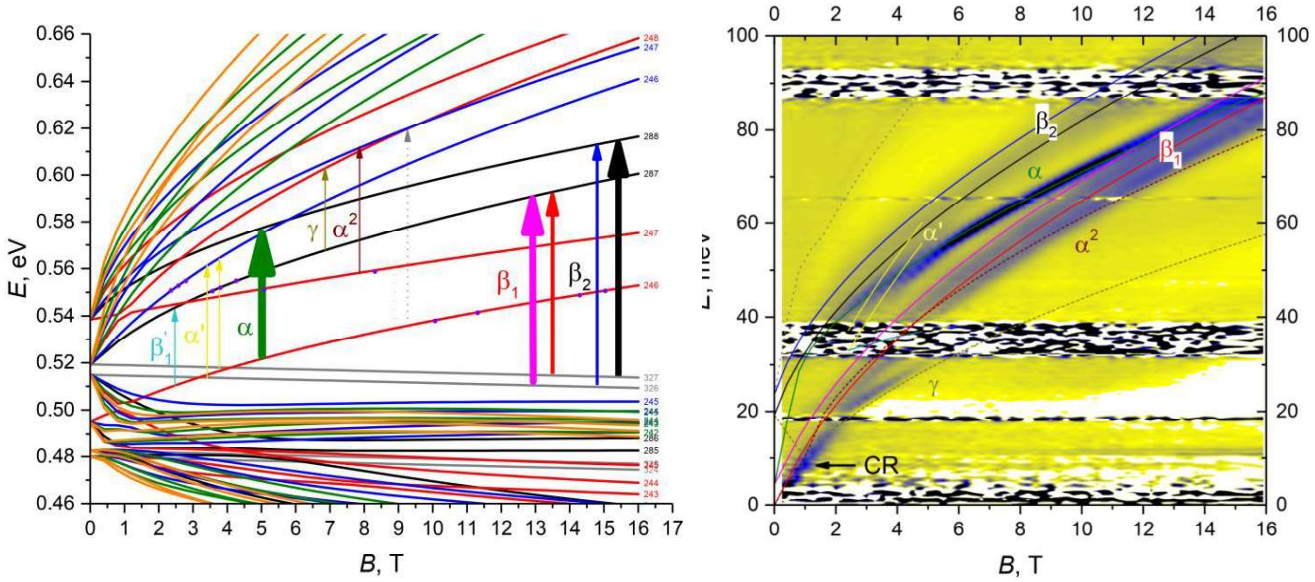

Fig. 34. a) Landau level fan chart for the sample 150219 at *T* = 80 K. Coloured lines represent Landau levels, characterized by different value of n. Vertical arrows with Greek letters represent the observed transitions. Orange arrow shows the energy the carrier can acquire by thermal activation. b) False colour map of the transmission of sample 150219 at *T* = 80 K as a function of energy and magnetic field with superimposed energies of the transitions shown in panel a). The maximum absorption corresponds to the blue colour. The arrow shows the absorption associated with cyclotron resonsance of electrons.

At the highest temperature available for our system T = 135 K (**Fig. 35**) the cyclotron mass increases up to $m^* = 0.0147m_0$. The carrier concentration determined by the upper boundary of γ line (B = 5.5–6 T) is equal to $n = 3.2 \cdot 10^{11}$ cm^{-2}. α line starts at magnetic field of 3 T due to depopulation of the initial zero-mode LL. The anticrossing between zero-mode LLs at this temperature is happening between 0 and 1 T, which signifies that the band structures of the system is turning to normal. The critical magnetic field of the anticrossing is moving monotonously with temperature with the rate of approximately 0.1 T/K, which suggests that the structure undergoes the second phase transition at *T* = 145 – 150 K.

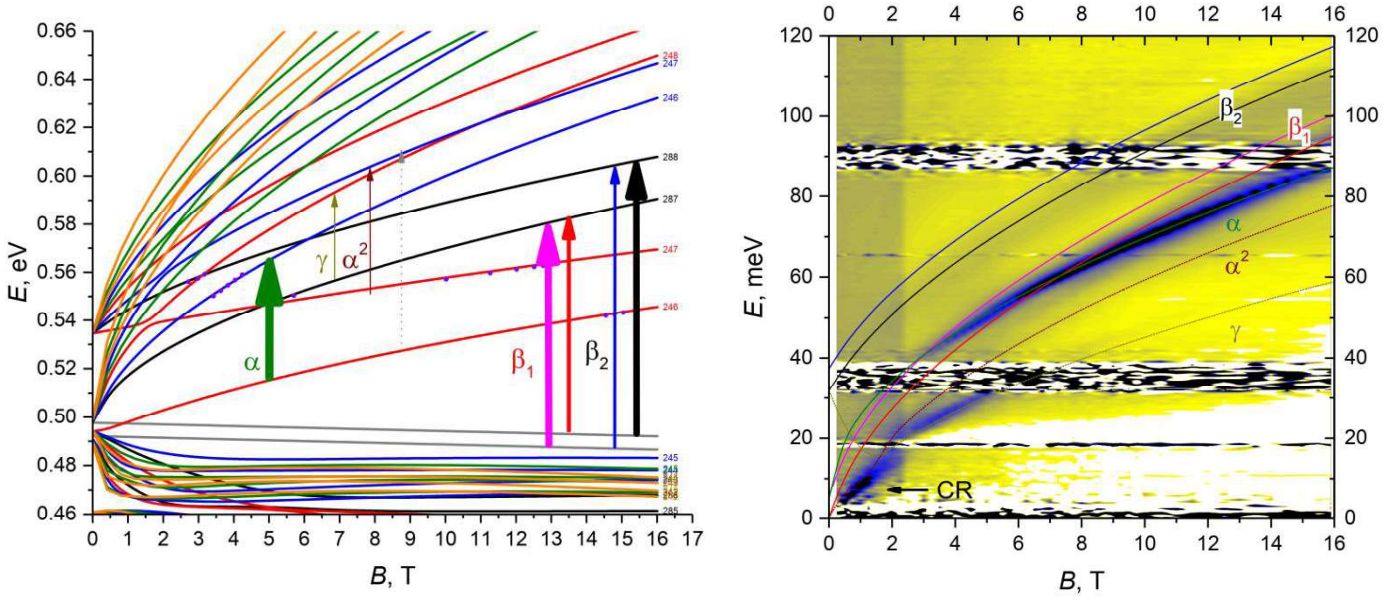

Fig. 35. a) Landau level fan chart for the sample 150219 at *T* = 135 K. Coloured lines represent Landau levels, characterized by different value of n. Vertical arrows with Greek letters represent the observed transitions. Orange arrow shows the energy the carrier can acquire by thermal activation. b) False colour map of the transmission of sample 150219 at *T* = 135 K as a function of energy and magnetic field with superimposed energies of the transitions shown in panel a)

3.4 Splitting of the zero-mode Landau levels by the built in electric field

Despite that characterization of the topological phases was the main goal of the studies of DQW heterostructures, in the course of the measurements we have observed a peculiar feature of the MA pattern which is specific to such structures and may be worth the separate study.

As it was discussed in **Section 3.1**, one of the most practically important feature of HgTe DQW heterostructures is the ability to tune the bandgap by the electric field. More precisely in the BG graphene phase the electric field applied to the growth direction shifts the mutual position of the quantisation subbands in two QWs and opens the gap in the spectrum. The same effect noteworthy can be achieved in the asymmetrical structure [81].

In the magnetic field the splitting of the bands at zero quasimomentum breaks the degeneracy of zero-mode LL. In MA spectra the gap is represented as the splitting of the absorption lines which involve this level. This effect was previously observed in the DQWs similar to the ones studied in this work and it was attributed to the built-in electric field generated by the surface charge (the effect of structure asymmetry could not provide gap with the observed magnitude unless the difference in the QW thickness was 2 nm, which contradicts with in-situ characterization of the samples).

It should be noted that within our calculations the electric field is an independent parameter, which was adjusted last for each temperature in order to fit the lines which involve the split levels. For the studied structures there are two pairs of such levels – β_1 and β_2 (See **Fig. 36**)

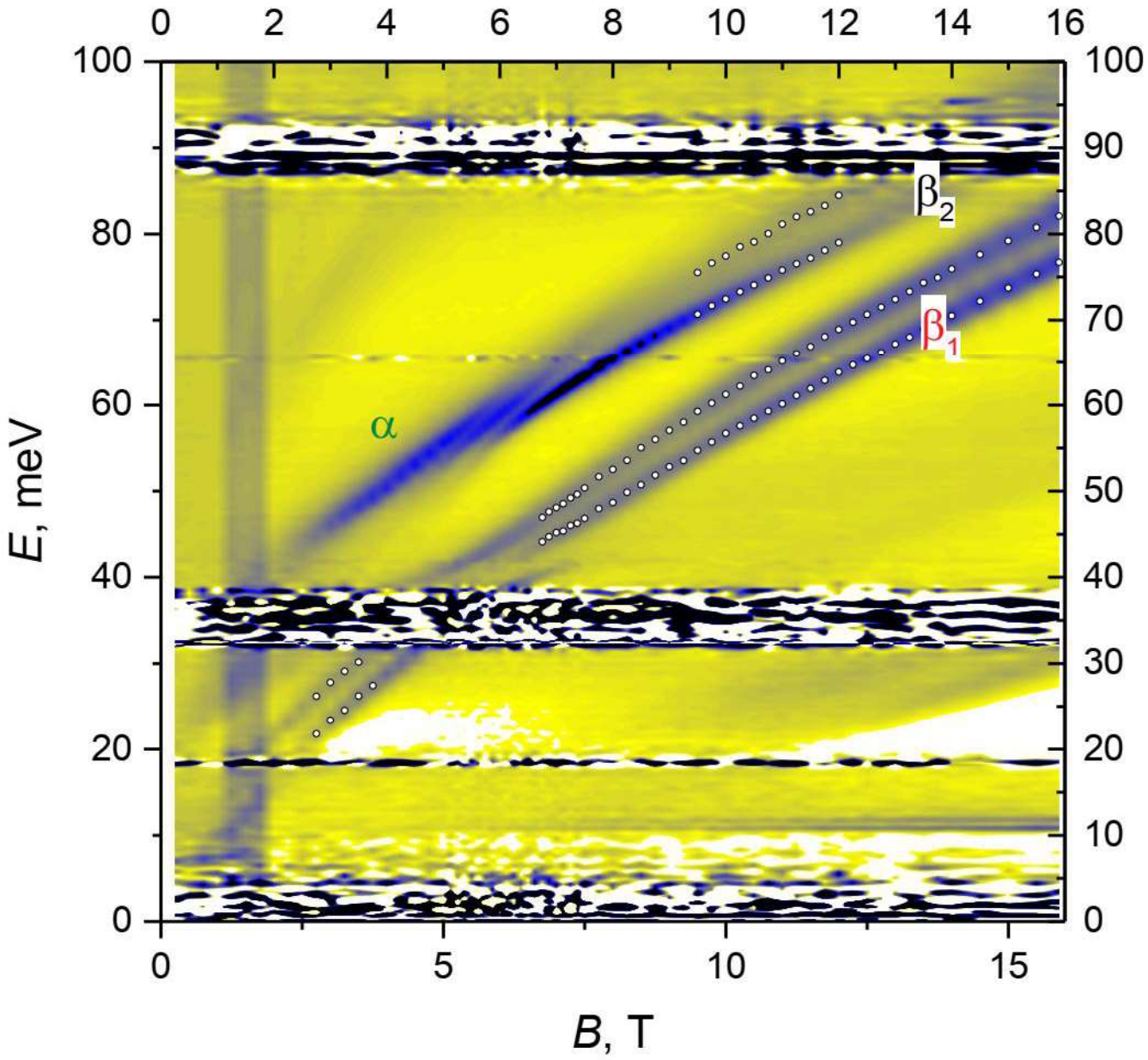

Fig. 36. Colour map" of the observed transitions of structure 150219* at 40 K in the range of magnetic fields from 0 to 15.9 T. The white dots show the maxima of the absorption lines β_1 and β_2.

The splitting was measured as the difference in the energy of the absorption maxima of the corresponding lines. When the maximum was not evident due to the broadening of the lines we used the Lorentzian analysis of the absorption line. The results of the measurements at T = 40K for structures 150218 and 150219 are shown in **Figure 37**.

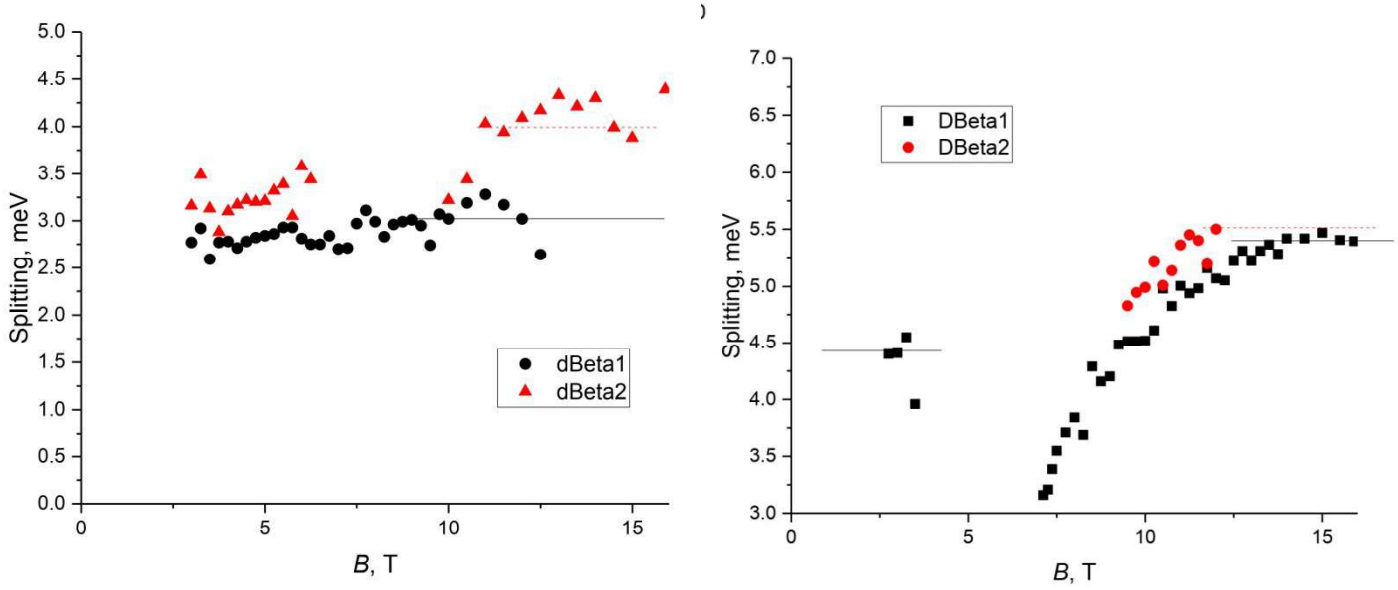

Fig. 37. Dependence of the magnitude of splitting of the lines lines β_1 and β_2. on the magnetic field at T = 40 K for a) sample 150218 b) sample 150219

As one can see, the dependence is different for two samples. For sample 150218 the splitting can be considered constant with magnetic field while for sample 150219 the splitting value increases for both of the lines. The summary of the measurements performed at all temperatures is shown in **Figure 38**. For sample 150218 one can see that the first pair of lines is almost constant of splitting while the other pair (β_2) is diverging as the temperature increases. Moreover the values obtained for the different sets of lines are different. This fact cannot be explained in a simple model of independent LLs as in this case the splitting values should be the same.

For sample 150219 the observed dependence of the splitting at high magnetic field is in-line with the common understanding of its origin. The two sets of lines have the same magnitude of the effect and its value is almost independent of temperature. However, if one considers the values that are obtained from the lower range of the fields, the magnitude is no longer constant and has a pronounced minimum at T = 50 K.

These results suggest that the splitting of absorption lines is not fully attributed to the broken degeneracy of the zero-mode LL is probably affected by the other mechanism.

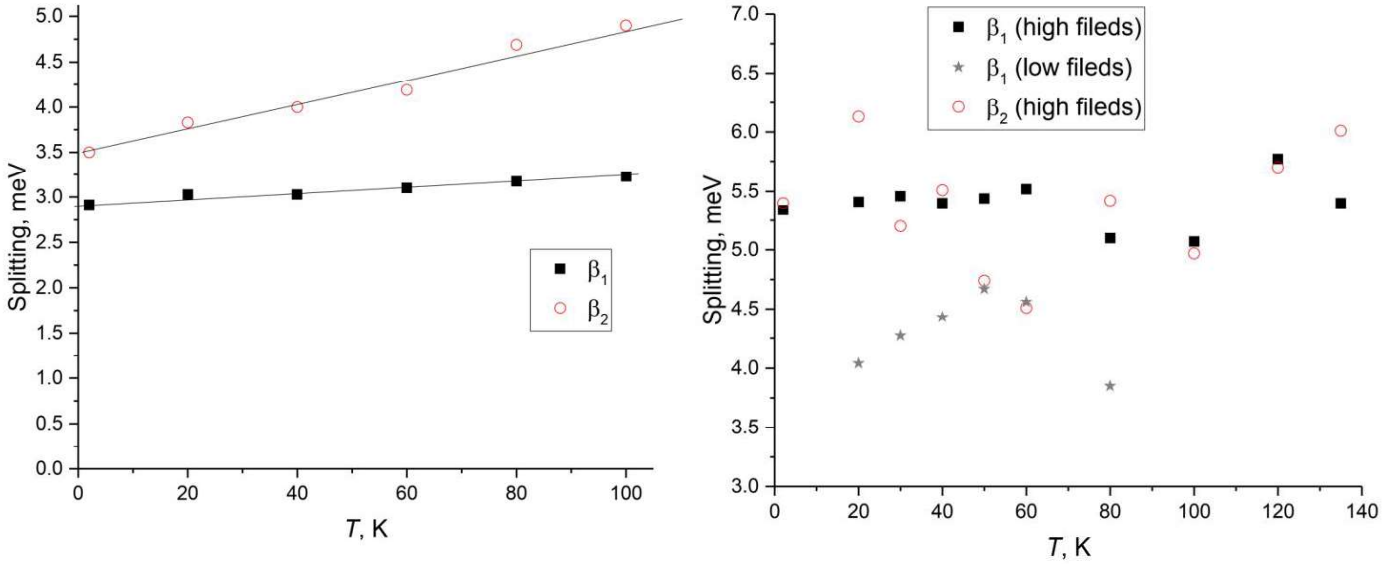

Fig. 38. Temperature dependence of the magnitude of splitting of the lines lines β_1 and β_2 for a) sample 150218 high magnetic field b) sample 150219 high and low magnetic field

3.5 Summary

The magneto-optical results presented in this chapter prove that temperature can be used as an external parameter to control band structure of HgTe/CdTe DQW and, as a consequence, to induce a topological phase transition. A set of two samples was investigated. The first sample at low temperatures in the state of bilayer graphene/TI and undergoes a phase transition at T_c = 40 K, characterized by a band gap opening. The summary of the experimental values of cut-off energy for sample 150218 are given in **Figure 39(a)**. The corresponding results of numerical calculations of the band structure based on the 8-band Kane model calculations are shown in **Figure 39 (b).**

The second investigated sample has the same BG band structure as the first sample in the intermediate temperature range (30 – 150 K). Extrapolation of the value of critical magnetic field (B_c) to higher temperatures suggests that at T = 150 K it undergoes the phase transition similar to the one found in first sample. The feature of the sample 150219 is that when the temperature goes below the critical value (T_c = 30 K) it undergoes another phase transition into the gapped state with two mutual inversions between hole-like and electron-like subbands. The second transition can lead to a formation of a novel phase, high order TI.

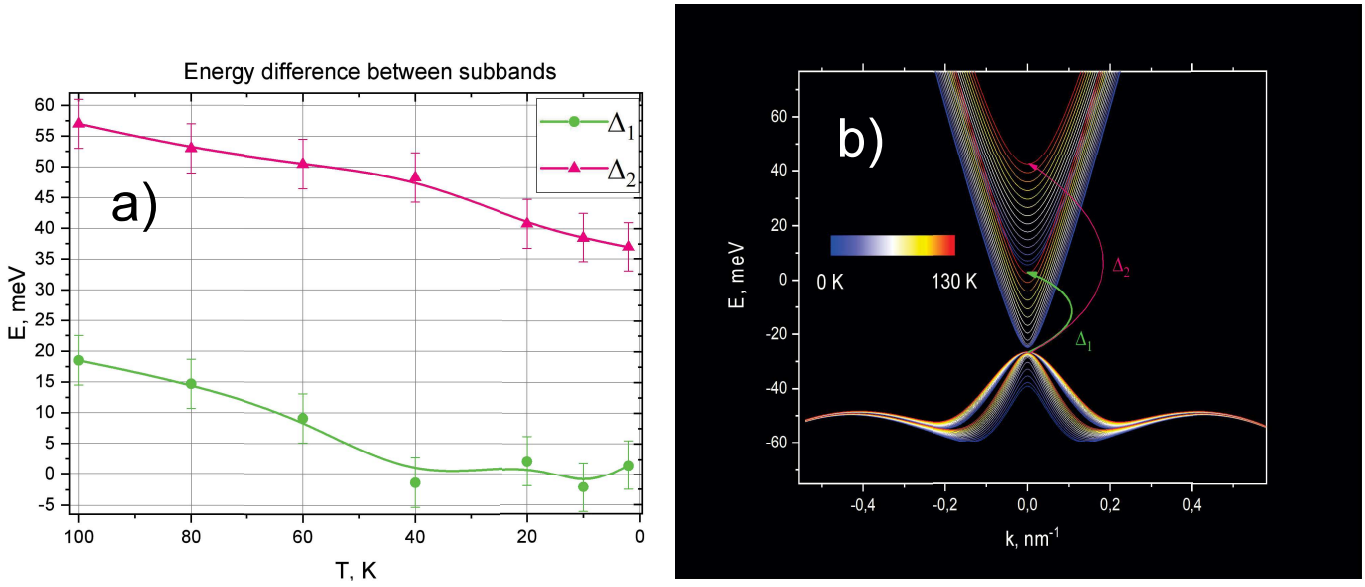

Fig. 39. a) cut-off energy of β transitions at different temperatures of sample 150218 b) calculation of the band structure of sample 150128 in the temperature range from 0 to 130K the arrow indicate the experimentally measured interband distances.

Another feature that was observed in the MA spectra of the studied samples is the unusual behaviour of the splitting of transitions involving zero-mode LLs. The magnitude of this effect contrary to the current understanding of the splitting mechanisms has dependence on the magnetic field and is different for different sets of lines.

If the first of these three effects is understandable as it stands, the other two require a more in-depth experimental and theoretical study. It is desirable that these first results pave the way for a detailed study of the effect of the electric field, e-e interactions, and multiple band inversions going towards high order topological insulators.

Chapter 4. Spectral studies of waveguide heterostructures with CdxHg1-xTe/CdyHg1-yTe quantum wells as a basis for the optical sources of far-infrared spectral range

As mentioned previously, HgCdTe-based QW is the first semiconductor structure in which the state of QSHI was demonstrated. But beyond this potential application for quantum technologies, this material is indispensable for the production of infrared (IR) detectors [82]. In this context, the band structure of both bulk HgCdTe solid solutions and heterostructures with QWs has been widely studied and described in detail. At the same time, a much smaller number of papers have considered the influence of the band structure of narrow-gap HgTe/HgCdTe heterostructures on the mechanisms of carrier recombination; only a few papers regarding mid IR lasers cover this topic [83,84]. Only recently it has been shown that due to specific characteristics of the band spectrum of HgCdTe-based QWs they can be used to obtain stimulated emission in the mid- and far IR range [85].

At present, the most effective semiconductor sources for far-IR range are quantum cascade lasers (QCL). They demonstrate the best figures of merit in almost entire mid- and far-IR range. The only "blind spot" of QCLs is the wavelength range from 20 to 60 μm caused by strong lattice absorption at frequencies of optical phonons in materials traditionally used for their production. It should be said that QCLs based on InAs partially solve this problem by stepping into the region of 20 - 60 μm from the side of the mid-IR region [86,87], while QCLs based on GaN working up to 5 THz were proposed to cover it from the side of long waves [88]. Nevertheless, at the moment the wavelength range from 20 to 60 μm is not fully covered by semiconductor coherent radiation sources.

HgCdTe based interband lasers are therefore of interest as an alternative to QCLs, as they are less demanding from the technological point of view and have greater wavelength tuning capabilities, while optical phonon frequencies in HgCdTe are lower than in AIIIBV materials [89]. The main advantage of heterostructures with HgTe/HgCdTe QWs as a material for creating IR sources is the suppression of Auger-recombination, which is the cornerstone of interband sources in the middle and far infrared range. The first results on obtaining SE from waveguide heterostructures with HgTe/CdHgTe QWs were rather encouraging [85], so the development of radiation sources of mid- IR range based on HgCdTe and optimization of heterostructure parameters for progression into the long-wavelength region is an acute problem. In this chapter we will therefore describe/study the potential/use of MCTs for laser applications in the THz Far-IR domain.

4.1 Mid-IR semiconductor lasers

Compact semiconductor lasers currently cover a wide range of wavelengths in the IR spectral region. While most commonly used type of sources in the near-IR range is semiconductor laser diode, mid and far infrared ranges are covered mostly by unipolar QCLs. The existing QCL technology allows creating radiation sources in the wavelength range from 3 to 20 μm operating up to room temperature [87,90]. QCLs are also used to produce THz radiation with a frequency of up to 5 THz [91,92]. However, the efficiency of most QCLs decreases at the wavelengths greater than 20 μm, because in this range the lattice absorption in GaAs and InP which are usually used for manufacturing of QCLs rapidly grows and above 30 μm it becomes practically insurmountable. Up to day generation from QCL structures was obtained only at several wavelengths in the spectral range of 20 - 25 μm corresponding to the minimum of absorption in the corresponding materials [86,93–95].

Lasers based on lead chalcogenides PbSnSe(Te) are an alternative source of radiation in the long wavelength part of the middle and far IR ranges. Lasers of this type are reported to be able to produce radiation at the wavelengths up to 50 μm [96,97], but their characteristics, in particular the output power, are limited due to difficulties in growth technology, and high (~10^{18}cm^{-3}) concentration of the defects. Besides, such lasers have not found wide application due to severe degradation during operation.

At the same time, the growth technology of another narrow-gap material, HgCdTe, is already well developed due to its extreme importance for the production of IR detectors. Modern MBE allows to produce high quality epitaxial films not only on CdZnTe substrates, which are usually used for HgCdTe growth, but also on alternative GaAs substrates [98]. In addition to the bulk films with low dark carrier concentration (~10^{14} cm^{-3}), MBE can be used to produce heterostructures with QWs [77]. Quantum wells based on narrow-gap solid solutions of $Hg_{1-x}Cd_xTe$ open up additional options for manipulating the energy of interband transitions and “engineering” of the energy spectrum of the carriers.

Experimental studies of lasing in HgCdTe-based structures were previously focused on the short-wave part of the mid-IR range, up to 3 μm [99–107]. Using the bulk layer HgCdTe as an active medium, the authors of previous works demonstrated emission at room temperature under optical excitation at the wavelength of 1.5 μm [102], and recently at wavelength of 2.5 μm [99]. At wavelengths above from 2.5 μm emission was obtained only at temperatures below 200 K [101,108]. In addition, several groups were able to get spontaneous [106,109] and laser [104,110] emission from the structures of this type under current pumping. The lowest generation wavelength of about 5.3 μm was obtained by Arias et. al. [100] at temperatures of liquid nitrogen and below. In a work by J. Bleuse et al. [107] previous publications on the topic of mid-IR lasers based on HgCdTe heterostructures were reviewed. In this paper it was concluded that interband lasers based on HgCdTe are not competitive in comparison with unipolar QCLs of mid-IR range. The main reason was stated to be the increasing role of non-radiative Auger-recombination accompanying the decrease of the bandgap. At the same time, in a theoretical

paper by Vurgaftman and Meyer it was shown that Auger-recombination can be suppressed in HgCdTe quantum wells compared to bulk solid solutions with the same bandgap [83].

As it has already been mentioned, in narrow-gap solid solutions based on lead and tin chalcogenides laser generation at wavelengths up to 50 μm was achieved. In these solid solutions, despite the high residual concentration of impurities and defects (the concentration of free carriers at 4.2 - 70 K exceeds 10^{17} cm^{-3} even in the best samples), Auger-recombination turns out to be suppressed due to "symmetry" of dispersion laws of of electrons and holes which allows lasing action [111].

The proximity of the effective mass values of electrons and holes leads to increased threshold energy of Auger-recombination, the value of which reaches the bandgap of the material with symmetrical parabolic bands. Similar "symmetry" can be achieved in heterostructures with QWs based on HgCdTe. The energy spectrum of HgTe/HgCdTe QWs can be regulated by changing their thickness and cadmium content in QW and barrier layers. At critical width the bandgap of HgTe/HgCdTe QW may close and the spectrum of carriers becomes "graphene-like" [12], which can fully prohibit Auger recombination. Secondly, the energy of optical phonons in HgCdTe solid solutions are shifted to the low-frequency region compared to $A_{III}B_{V}$ materials. The energy of HgTe- and CdTe-like optical phonons in HgCdTe is approximately 15 and 20 meV, respectively [89]. This suggests that in the wavelength range of 10-30 μm, which lies above the double phonon frequency, lattice absorption cannot interfere with emission from HgCdTe-based heterostructures. A number of recent studies of PL in structures grown by the MBE in the IPS SBRAS, demonstrate weak temperature attenuation of interband PL, especially in heterostructures with QWs [64,112]. In recent years, a record PL wavelength of 26 μm [63] was obtained in the bulk structure of HgCdTe, and then this result was improved to 36 μm [113].

Spectro-kinetic studies of PL under powerful pulse excitation carried out in our laboratory have shown that the decay time of interband PL in QWs on the basis of HgCdTe increases with increasing the pumping intensity and reaches 5 μs in structure with 120 meV bandgap. This was explained by the saturation of the channel of non-radiative recombination by the Shockley-Read-Hall mechanism [114]. Then, in the course of the first studies of the waveguide structures with QWs, stimulated emission with wavelengths up to 10.2 μm [85] were demonstrated at temperatures up to 120 K.

In the works [59,85] it was suggested that the use of structures with narrow $Cd_xHg_{1-x}Te/Cd_yHg_{1-y}Te$ QWs instead of bulk layers as an active region of laser structures makes it possible to significantly reduce the rate of non-radiative Auger recombination and increase the achievable wavelength of radiation. An important practical result obtained in these works is relatively low threshold pumping intensity required for the onset of SE. This in fact means that such structures have a "budget" of excitation power to emit further in the long wavelength region of the spectrum.

In this work, we conduct experimental studies to support this assumption. We present new designs of waveguide heterostructures, for which SE at the wavelengths up to 18 μm was obtained. Then we analysed the active region of the heterostructure and optical pumping in order to improve the characteristics of SE at longer wavelengths and higher temperatures.

In the course of work, the PL, MA and SE spectra of waveguide heterostructures based on HgCdTe were studied. Calculations of the band structure performed by V.Ya. Aleshkin were used to determine carrier dispersion of the investigated structures. A four-band Kane model of was used to calculate dispersion laws of electrons and holes, which was confirmed to perfectly agree with the experimental results in HgTe QWs [26,59]. QWs grown on the GaAs (013) substrate were considered as they correspond to experimental samples. The Kane Hamiltonian for such quantum wells is given in [115]. Calculations also considered symmetry reduction on a heterojunctions by the means of Ivchenko term [116]. For the case under consideration the explicit form of this term is given in [117].

4.1.1 Auger recombination threshold

As it is known, the main factor that leads to the temperature quenching of stimulated radiation in narrow-gap semiconductor structures is the Auger-recombination, a three-particle process in which the energy released during the recombination of the electron-hole pair is transferred to a third carrier[118,119]. However, Auger-recombination requires that the total kinetic energy of electrons and holes involved in recombination exceeds the threshold value $E_{th} \sim m_e/m_h$, where m_e and m_h are the masses of the electron and the hole.

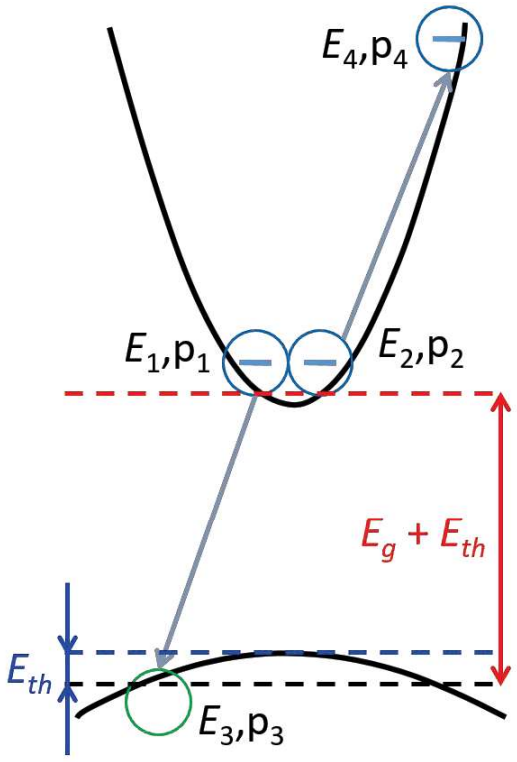

Fig. 40. Schematic picture of the Auger process.

Obviously, Auger-recombination becomes ineffective at temperatures much lower than this threshold energy. The magnitude of the threshold energy can be determined if the law of dispersion of carriers involved in the Auger-recombination process is known by minimizing the initial energy of the three particles capable of participating in the process.

4.2 Stimulated emission measurements – setup specifics

Stimulated emission requires higher excitation power which can be achieved by pulsed sources. In this work we used either OPO or CO2 laser. The pulsed nature of the SE does not allow using Lock-in amplifier for averaging the signal, thus it was directly passed to the ADC board after its amplification. The filters of the pre-amplifier were set to the most narrow range, which does not affect the shape of the signal. Geometry of the setup was also modified. The SE signal was most often collected from the edge of the sample, because the radiation pattern of the SE is not homogeneous, and the maximum lies in the plane of the structure.

During all the measurements the Fourier spectrometer was operated in the step-scan mode. In this mode the moving mirror of the spectrometer is moving not at a constant speed, but in separate "steps", the length of which is determined by the required upper boundary frequency of the investigated spectrum, and the number - by spectral resolution. After the mirror is positioned, for each of the steps there is a delay, which allows the mirror to stabilize, before the actual measurements start.

Stabilization of the mirror is required because, as it was mentioned before, one of the main challenges of PL measurements in the long-wavelength range is the necessity to selectively amplify small PL signal whilst minimizing the powerful background radiation of the room temperature bodies. It turns out, that the modulation of the background thermal radiation caused by the movement of the mirror causes the overload of the detector and the entire measurement circuit. Thus, the measurements of the signal must start with some delay to let the overload relax. For MCT detectors a delay of 500 ms is enough to avoid the overload, while for silicon bolometer it takes at least 3 s.

During the PL studies in quasi-continuous regime, when the mirror is stable, background radiation does not affect the measurement, since only the modulated signal is recorded. When SE is considered, the Lock-in amplifier cannot be used, thus a background radiation is still reflected in the spectrum. However, the spectrum of the SE is usually represented by a single narrow and intensive line, and the influence of the background radiation is insignificant.

Additional reduction of the background noise was achieved by utilising time resolved PL spectroscopy. It is based on the fact that when SE starts, all the radiation is emitted over a short period of time (shorter than 10 ns). During that period the power of SE by far exceeds the background radiation while still being less intensive on the average.

For time resolved measurements, the spectrometer was operated in step-scan mode with external synchronisation by the excitation pulse, For each point of the interferogram a series of measurements was done at different time slices after the synchronisation pulse. The Fourier transform of each of the time slices gives the emission spectrum at a certain moment of time. Although time resolution does not provide additional information for the studies of SE, since the evolution was determined by time constant of the detector, it reduces the noise and allows finding even the weak SE signal.

4.3 Studied structures

All waveguide structures studied in this work were grown by MBE on a semi-insulating GaAs substrate similarly to the DQW heterostructures [77]. First, a buffer layer of 50 nm ZnTe was grown sequentially followed by a relaxed CdTe buffer about 5 microns thick and then the main part of the structure (**Fig. 41**). The surface of the structure is covered with a 50 nm thin layer of CdTe, which serves to stabilise mercury inside the structure.

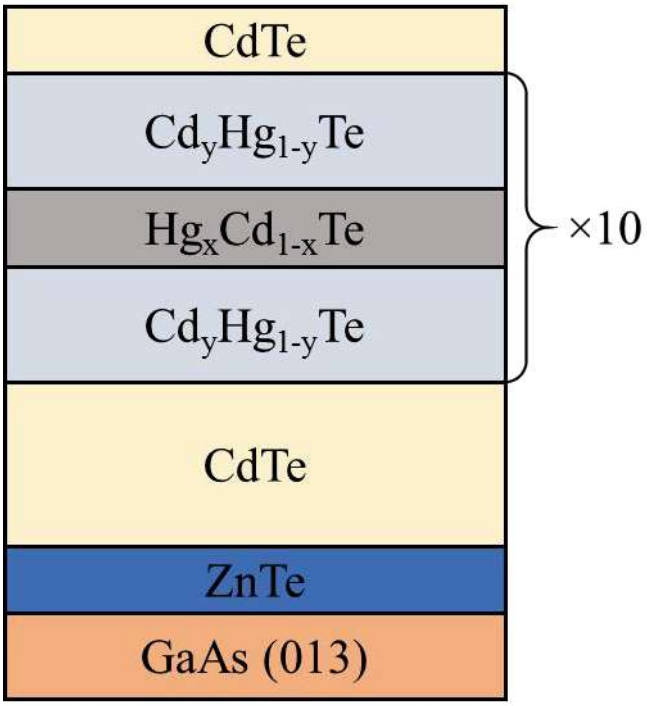

Fig. 41. General growth scheme of studied quantum well heterostructures.

The core of the structure consists of an active region, which is formed by the array of HgCdTe QWs, separated by tunnel non-transparent barriers with high (usually about 65%) cadmium content, and "waveguide layers" - wide layers of CdHgTe, which provide localization of the maximum TE_1 mode in the vicinity of the active region.

The characteristic growth scheme of waveguide structures (for structure 170127) is shown in **Fig. 42.** Parameters of studied structures are given in **Table 3**.

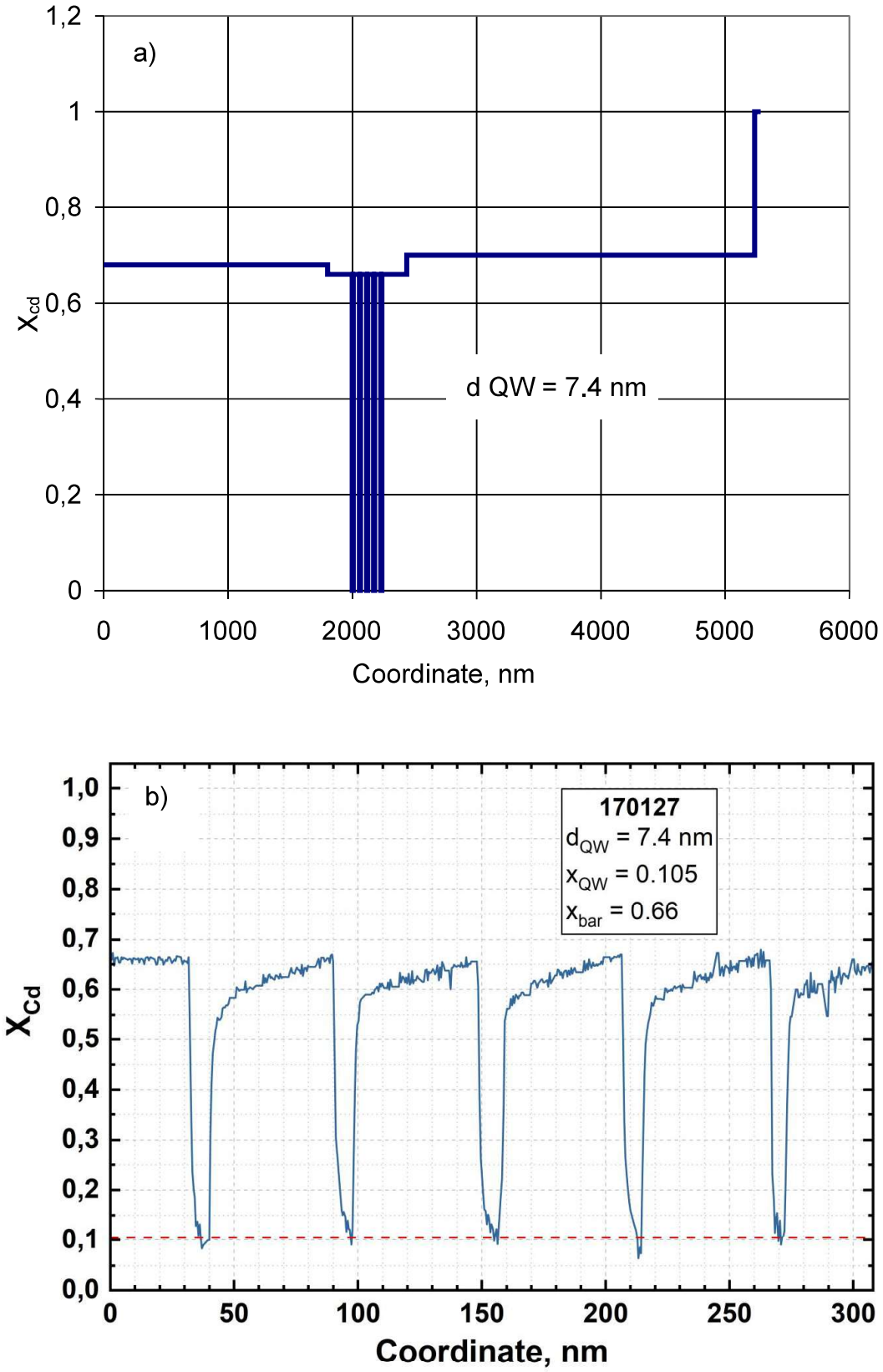

Fig. 42. (a) Cd distribution for sample 170127 (14 μm emission wavelength) measured during the sample growth. The end of the CdTe buffer layer is taken as a starting point. (b) Zoom in the active region of the sample.

Table 3. Parameters of the studied structures adjusted according to their ex-situ characterization: d_{buf} – thickness of the waveguide layer from the substrate side; d_{wg} – thickness of the waveguide layer from the surface side; x_{bar} – Cd content (x_{Cd}) in the barrier layers between the QWs; n_{well} – the number of the QWs in the active region; d_{well} – width of the QWs; x_{well} – Cd content in QWs; E_g – the bandgap of the structure, calculated in the framework of Kane Hamiltonian 8×8 for T = 0 in reciprocal centimetres, cm^{-1} (units of frequency commonly used in IR spectroscopy) and corresponding wavelength in μm.

Sample	d_{buf} (мкм)	d_{wg} (мкм)	x_{bar}	n_{well}	d_{well} (нм)	x_{well}	E_g (cm^{-1})	E_g (μm)
161103	1.9	2.9	0.65	5	2.8	0	1370	7.3
161111	1.7	2.7	–	1	100	0.265	1370	7.3
161222	3.4	4.4	0.63	5	6.1	0.108	890	11.2
170126	1.8	2.8	0.66	10	7.6	~ 0.1	550	18
170127	1.8	2.8	0.66	10	7.4	0.105	660	15.2
170202	2.7	3.47	0.60	5	3.85	~ 0.1	680	14.7
180913	1.8	3.2	0.3	10	5.7	~ 0.1	560	17.8

It is important to note that as the wavelength increases, thicker waveguide layers are required for effective mode localization. At wavelengths above 18 μm, in order to realize dielectric waveguide, one needs to grow layers of up to 5 μm of total thickness. This is a challenging task from the point of view of the growth technology of such structures, because during the growth of a narrow QWs even a small deviation from the given width of the well may result in a large change of the transition energy, so the growth rate of the active region should be less than that of the bulk layers.

Within the framework of this work, the technology of "fast" growth of waveguide structures with QWs was probed, within which waveguide layers are grown at high rate but relatively low homogeneity of solid solution. The active region, at the same time, is grown slower but with higher accuracy. This provides an overall growth rate corresponding to the growth rate of bulk HgCdTe films (2-3 μm/hour). Studies of PL and SE have shown that the quality of such structures is not inferior to other structures in the series.

4.4 Ex-situ sample characterisation

The main objective of characterization of heterostructures with QWs is to determine the band gap of the sample, since even small deviation from the desired growth parameters can lead to a significant

shift of the fundamental transition energy and, accordingly, the wavelength of emission. At the same time, the emission wavelength, regulates the thickness of waveguide layers used to restrain the electromagnetic field and large mismatch between expected and actual transition energies leads to the electromagnetic field "leaking" into the substrate and prevents the onset of SE. Secondly, the information on bandgap value is important for the set-up adjustments in order to search for SE signal in a specific wavelength range.

Another important task of sample characterization is to reconstruct the growth parameters of the QWs required to calculate the dispersion relations and the probabilities of radiative and non-radiative recombination, which are crucial for the analysis of the fundamental processes that determine the efficiency of SE. Understanding the relationship between the structure parameters, recombination processes and its photoresponse allows increasing the figures of merit of the structures (critical temperature of SE quenching, maximum wavelength, threshold pumping intensity).

In this work the main characterization methods used were PL and MA spectroscopy, introduced in **Chapter 2**. PL spectroscopy is a natural method of structure characterization as it uses the setup, similar to that used for obtaining SE. PL spectra allow us to determine the optical bandgap of the structures, while the study of their temperature dependence provides information about the growth parameters of the QW.

Figure 43 shows the temperature dependence of PL spectra for structures 150120 and 161222, both of which were designed for emission wavelength of 10 μm. At low temperatures the red boundary of PL spectra is practically the same, but PL spectrum of structure 150120 is significantly wider of structure 161222. We attribute it to the higher homogeneity of the second sample which is caused by the use wider QWs in sample 161222. For wide QWs deviation of the QW width from its original value the leads to smaller relative difference for two samples, and as a result, lower energy dispersion

With increasing temperature, the PL lines broaden and shift towards higher energies. An important observation is that the PL line of sample 150120 moves faster than the line of sample 161222. This is due to the presence of a small cadmium concentration in the QWs of structure 161222, which slows down the temperature growth of the energy of fundamental transition in a QW. Thus the analysis of PL spectra makes it possible to distinguish between the QWs made of pure HgTe and QWs with residual concentration of CdTe.

The main disadvantage of this method of sample characterisation is its low accuracy. As **Figure 43** demonstrates, at low temperatures the PL lines have the width at half maximum (FWHM) equal to 6 meV for structure 161222 and 15 meV for structure 150120. At room temperature characteristic FWHM of the studied structures reaches 80 meV. On the other hand the divergence of the bandgap energy in QWs the with typical CdTe concentration (from 5 to 15%) acquired over 300 K temperature

range is less than 30 meV. It increases the mistake in parameters of the QWs due to uncertainty of the red border position of PL line. Another common problem is the interference of PL collected from the top of the structure, which distorts the shape of the line and can mask the red border of the PL line.

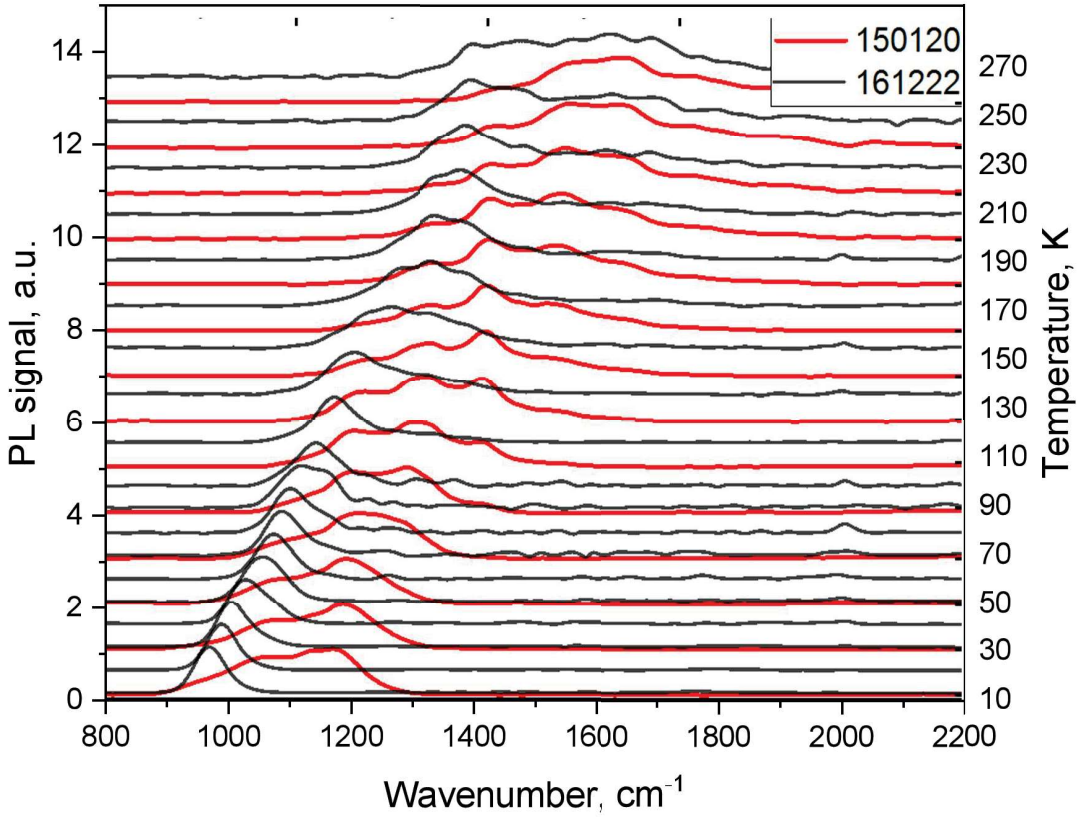

Fig. 43. Temperature dependence of the PL spectra of structures 150120 and 161222. The spectra were measured under continuous wave 800 nm pumping. The right

A more reliable way to determine the width and composition of the QW is to track the energy of the excited states in the QW, which is locked to its parameters. Given that there are only two unknown parameters, in order to find them it is sufficient to measure the energy of only two different optical transitions. Unfortunately, the excited carriers quickly decay to the ground states through phonon emission. As a result, the transitions from the excited states are not visible in the PL spectra.

One way to detect excited states is by photoconductivity (PC) spectroscopy. When PC spectrum is recorded, sample acts as a photoresistor, the sensitivity of which is measured depending on the wavelength of the incident radiation. Contrary to the PL, PC is based on absorption mechanism, which reflects all optically active transitions including those, for which radiative recombination is not the dominant process. Yet, the matrix element of optical transitions between the excited states of the QW is small and they manifest themselves as a small variation on the large background coming from of the

fundamental transition. Moreover, even if the spectrum is normalised by the transmission of the optical path one can still observe the features inherent to the sample, such as impurity bands and phonon absorption. Thus, the PC spectroscopy can be used only in conjunction with PL spectroscopy for refining the parameters of the structure.

The most universal method of sample characterization used in this work is MA spectroscopy introduced in **Section 2.2.** Like for the PC its underlying physical effect is the absorption of radiation by the electron gas, therefore it reveals all optically active transitions. However, in contrast to PC, spectral features of different energy levels are separated and the intensity of some optical transitions increases with magnetic field making detection of the excited states an easier task compared to other methods.

Figure 44 (a) shows the MA spectra of structure 170126 which emits at the wavelengths of 18 μm. The spectra (Courtesy of L. Bovkun et. al.) were measured at Laboratoire National des Champs Magnétiques Intenses (LNCMI-G, Grenoble, France) in magnetic fields up to 11 T at T = 4.2 K.

An evident difference between the TQW heterostructures discussed in **Chapter 2** and HgCdTe waveguide heterostructures is that absorption spectra contain a large number of transitions between LLs, which makes their complete analysis a tedious task. At the same time, as noted earlier, in order to determine the parameters of the QW it is sufficient to measure the energies of the excited states of the QW at zero magnetic field. For the studied structure there are two different set of LLs tending to 70 and 140 meV. Comparing these values to the calculation of the band structure for QW of different structure shows that the best correlation between theory and experiment correspond to the width of a QW equal to 7.8 nm and the CdTe concentration in the well equal to 0.08.

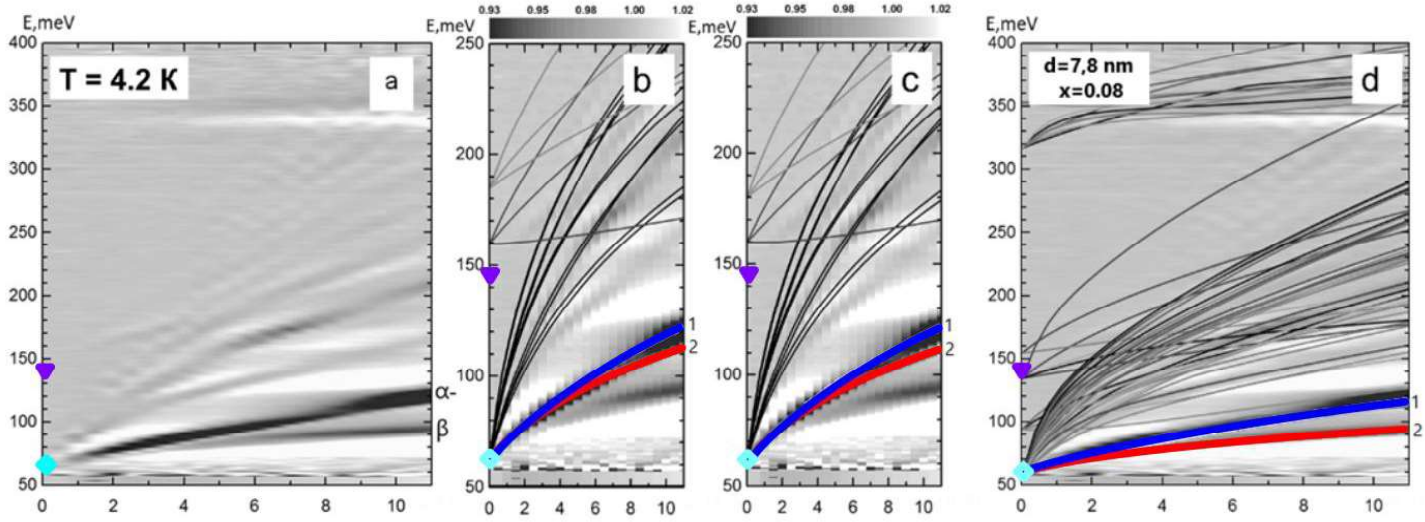

Fig. 44. Results of magneto-optical measurements of structure 170126 at T = 4.2K (a) with superimposed results of theoretical calculations (b - d) of possible inter-LL transitions for the (b) rectangular well HgTe with a thickness of 4.4 nm (c) trapezium QW with bases 3.5 nm and 7

nm bases; (d) rectangular well $Hg_{0.92}Cd_{0.08}Te$ with a thickness of 7.8 nm. The cut of energies of interband transition are marked with symbols. Calculated energies of α- and β transitions are highlighted with blue and red curves correspondingly.

The result based on the energies of excited states in a QW can be independently verified by comparing the magnetic field dependence of the strongest interband transitions: α- and β with results of the calculations. The analysis of MA data shows that the observed magnetoabsorption pattern cannot be described without assuming that there is Cd in the QW. Indeed, **Fig. 44 (b)** demonstrates that the calculations of transitions for a zero concentration of Cd in the QW, do not allow a satisfactory description of the observed lines.

The behaviour of α- and β transitions allows determining not only the Cd content in solid solution of the QW, but also gives information on its shape. As shown if **Fig. 42 (b)** the interfaces between the QW and barrier layers are not sharp, hence the QWs have trapezoidal shape. One may suggest that a QW with trapezium profile is able to better describe the experimental data so we performed calculation for the QWs with such shape as well. The best fitting of the experimental data by a trapezium HgTe QW is shown **Fig. 44 (c),** and it evidently does not improve the agreement between theory and experiment. On the other hand, the results of the calculations based on the parameters obtained from the energy of excited states are in good agreement with experimental data (**Fig. 44 (d)**).

In a similar fashion we performed characterisation of all the studied structures either by comparing the obtained temperature dependencies of the bandgap otr the energies of excited states in a QW with the results of calculations on a set of $Hg_xCd_{1-x}Te$/ $Hg_yCd_{1-y}Te$/ $Hg_xCd_{1-x}Te$ QWs with different widths and cadmium contents. It should be noted that for the composition of barrier layers (x_{bar}) we were using the values measured in-situ during the sample growth. This can be done because small deviations in parameters of the barriers have little effect on the band spectrum of the QW.

4.5 Comparison of the structures with single potential well and an array of narrow QWs

The first goal of this part of the work is to compare structures with the same bandgap but different design of the active region, containing either a single potential well or a cluster of thin HgCdTe QWs. Preconditions that structures with low-cadmium narrow QWs are preferable for obtaining SE in the long-wavelength region of the spectrum can be found in paper [120]. Specifically, in structures with wide potential wells, formed by solid solution of HgCdTe SE was observed only at temperatures up to 120 K which is more than 50 K less than in the structure of with narrow HgTe QW, despite the fact that structures with wider wells were designed for a shorter wavelength. Besides, complete realisation of SE in the structure with bulk layer of CdHgTe used as an active region, was not possible, as reported in [121]. These results indicate that narrow QWs are more effective as radiation sources in mid- and far-

IR range, than bulk layers, but no direct comparison of the emissivity of structures with narrow HgTe QWs and wide potential wells has been done yet.

In order to assess the prospective of wide and narrow wells for HgCdTe based long-wave lasers, emission studies in pulsed regime were conducted on two structures (161111 and 161103). The design of waveguide is aimed at effective localization of radiation with a wavelength corresponding to the calculated energy of interband transitions. **Fig. 45 (a, b)** show the distribution of the refractive index along the growth axis of the sample (reflecting the thickness and composition of the structure layers) and the calculated localization of TE_1 mode for both structures. As it can be seen from **Fig. 45 (a, b)**, the designs of the dielectric waveguides for these structures are almost identical. In structure 161111 there is one wide (100 nm) potential well with the composition of solid solution x = 0.265, and in structure 161103 there are 5 2.8 nm-wide HgTe QWs placed in the high e-field region.

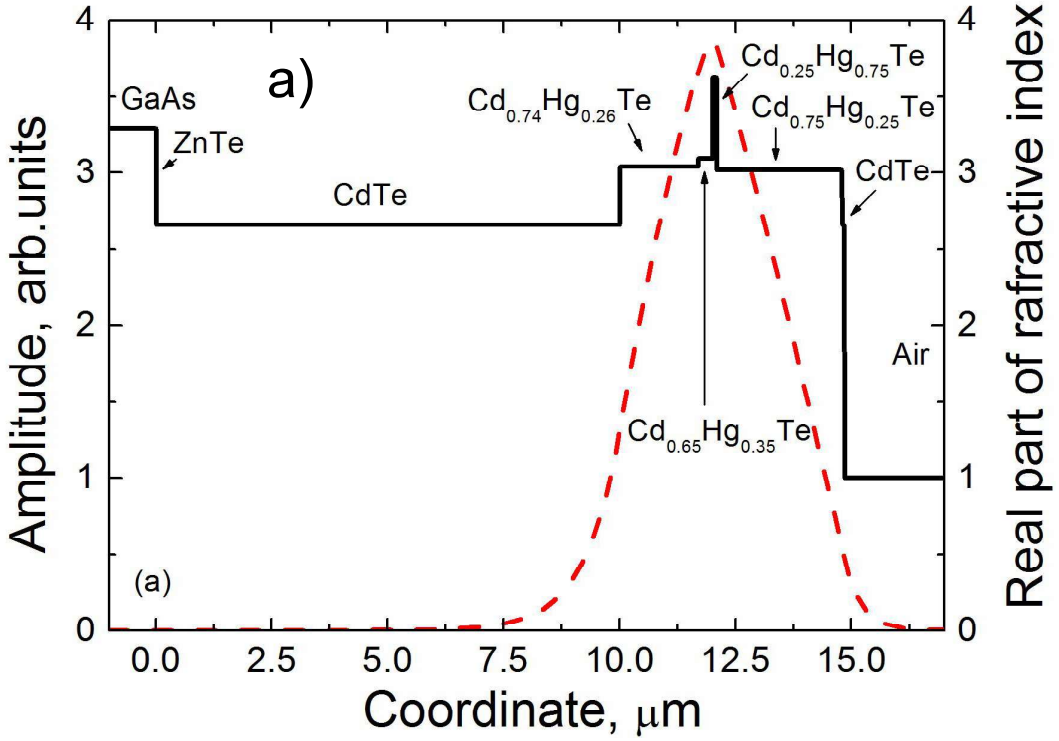

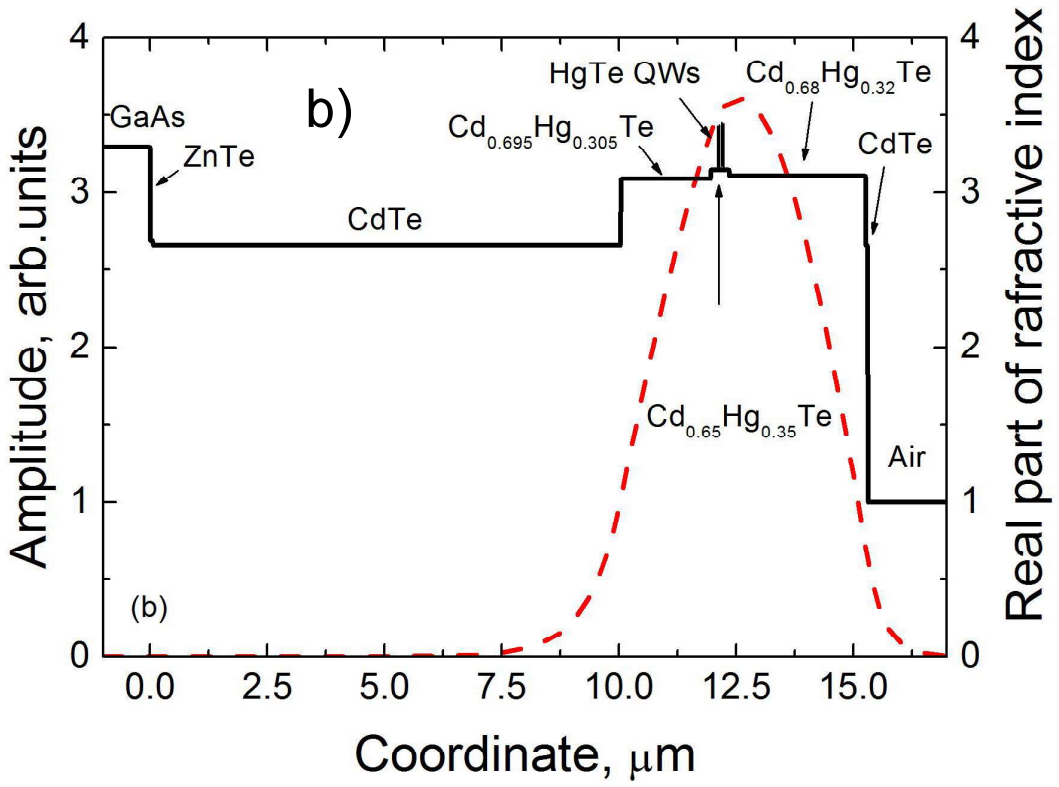

Fig. 45. Distribution of the real part of the refractive index and calculated localization of the TE mode for the radiation wave 6.6 μm a) in the structure 161111 b) in structure 161103

Fig. 46 (a,b) shows the results of the calculations of the band structure for samples under study, performed within the axial approximation within Kane Hamiltonian 8 × 8. We can see that the values of the bandgap in the two analyzed structures are close and equal to approximately 170 meV.

Results of emission studies in these structures are presented in **Figure 47.** As can be seen, for both structures, the longwave cut-off of the emission spectrum lies close to 170 meV, which corresponds to the energy of the fundamental interband transition, but in a structure with narrow QWs at the pumping intensity of 200 W/cm2 a narrow line of SE appears, while in a structure with a wide well only a much wider spectrum of spontaneous PL is observed up to the maximum pumping intensity of ~ 100 kW/cm^2 and SE cannot be obtained. It should be noted that the samples were grown within the same technological series and the lifetimes measured by photoconductivity relaxation (at low excitation) are ~ 10 μs in both structures. The most probable reason for the absence of SE in the structure with wide well is difference in the band spectrum, which becomes important at high carrier concentration when Auger-recombination has a significant contribution to the total recombination rate of the carriers.

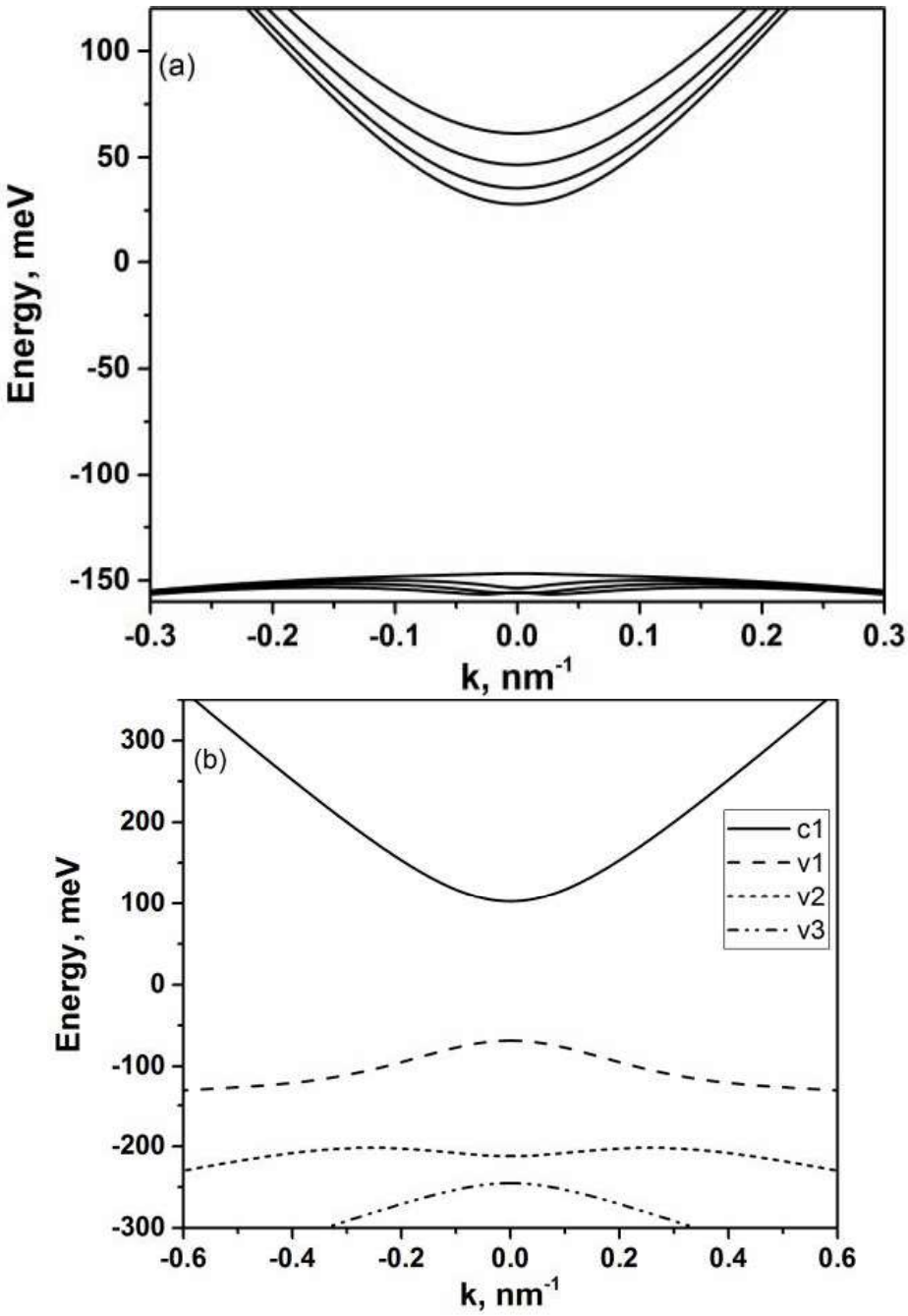

Fig. 46. a) Results of calculation of the energy spectrum of structure161103 b) results of calculation of the energy spectrum of structure 161111 (first 4 sub-bands of valence and conductivity bands).

In addition to the threshold Auger process mentioned in the **Section 4.1**, in there are non-threshold Auger recombination processes which are specific to heterostructures with QWs and arise due to the presence of interfaces. Such processes were studied in detail in [122]. According to the authors, the following conditions must be met to suppress non-threshold recombination processes: (i) $E_g < E_c$, $E_g < E_v$, where E_c, E_v is the value of the energy gap between fundamental states in a QW the energy of the continuum for electrons and holes respectively; (ii) $E_g < E_2 - E_1$, where E_2, E_1 is the energy of excited dimensional quantization levels. Calculations show that the first condition is satisfied in both structures: the energy transmitted to the carrier during Auger recombination is close to E_g and insufficient for

"ejection" of the carrier into delocalized states in the barriers. Obviously, this condition will be fulfilled for structures with narrower bandgap as well, and the better the smaller the is band gap of the QW. On the other hand, as we can see from **Figure 46** the second condition in wide wells can hardly be fulfilled even in very narrowband structures: the energy gap between electronic subbands does not exceed 10 meV while the spectrum of holes is practically not quantized. At the same time, in narrow QWs the second condition for electrons is clearly fulfilled (according to the calculation, in the QW considered there are no localized states in electronic subband at all, except for the second one), and for holes of the energy order E_g it is enough only for transition to the second subband. Finally, the "threshold" Auger process similar to that in the bulk material is also suppressed in the narrow QWs, since the effective masses of electrons and holes in the main subbands are closer than in the broad well. (As shown in paragraph 3.1, the threshold energy for such an Auger process involving two electrons and a hole is equal to $\mu \cdot E_g$, where μ is the ratio of electron mass to hole mass).

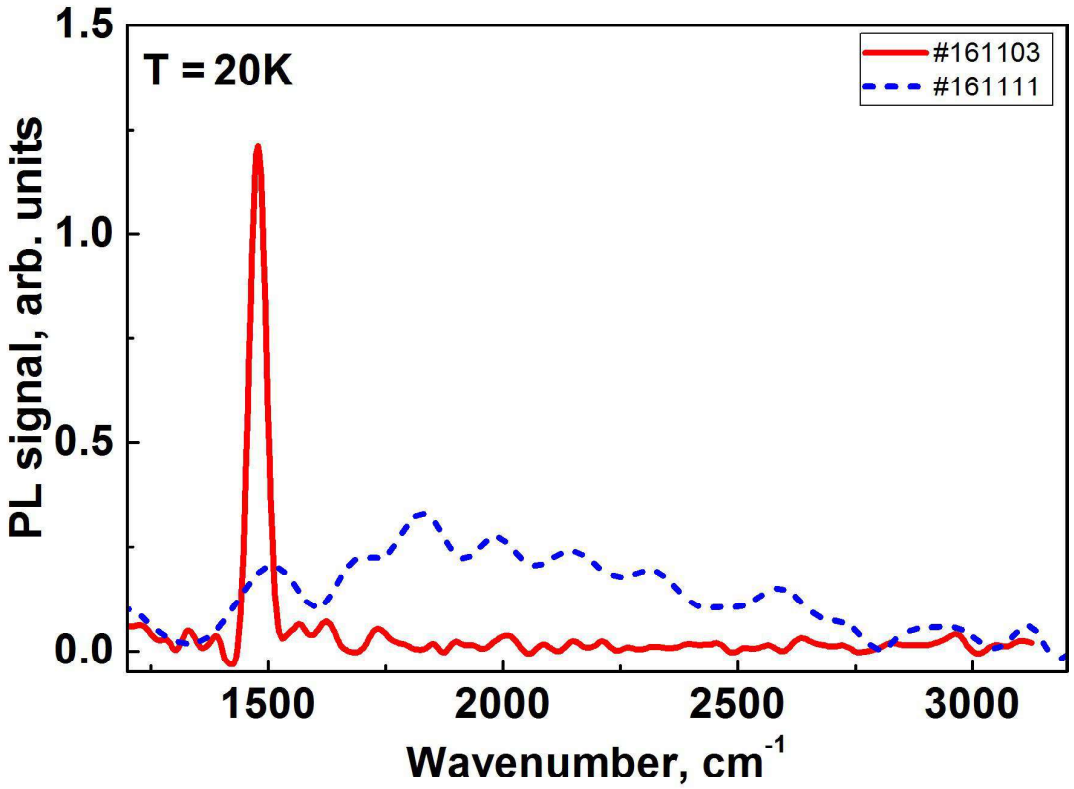

Fig. 47. PL and SE spectra of the structures under study at 20 K under pulsed 1.5 μm pumping. Pumping intensity was equal to 2 kW/cm^2 for structure 161122 and 100 kW / cm^2 for structure 161111

Summing up, as it was suggested earlier, narrow QWs are more favourable for obtaining SE in the long-wavelength region as they provide better suppression of AR. At the same time, the only publication that was focused on SE in structures with potential well at the wavelength above 5 μm [121]

reports on the ambiguous results. In this part of the work we performed a direct comparison between heterostructures with narrow QWs and wide potential wells (published in [123]). Our results confirm the superiority of QWs as in similar experimental conditions SE does not develop in structure with potential well. This result sets the vector of future studies of HgCdTe-based sources for mid- and far-IR range. Specifically, all subsequent structures in this work used narrow QWs in the active region and were focused on optimizing their design.

4.6 Optimization of the parameters of the QWs for suppression of Auger-recombination and obtaining SE in the long wavelength region of the spectrum

As it was mentioned above, radiation sources based on HgCdTe have the greatest practical value for the region of the *Reststrahlen* band in $A_{III}B_V$ materials (from 25 to 60 μm). The first experiments on emission from heterostructures with HgTe/CdHgTe QWs showed that SE in such structures can be obtained at wavelengths up to 10 μm, which significantly exceeds the best results obtained in bulk films. In addition, it has been shown that the critical temperature of SE quenching is above 77 K, and the threshold for pumping intensity is as low as 0.1 kW/cm^2 at 20 K. These results indicate that it is possible to create structures for producing SE with longer wavelength in the far-IR region. At the same time, it is known that a reduction of the bandgap leads to an increase in the Auger recombination rate and a decrease in the rate of radiant recombination. Therefore, as the wavelength increases, more and more stringent requirements are imposed on the active region design to reduce the effect of Auger recombination.

When the active region of the structure is formed by the bulk HgCdTe layer, its band structure is rigidly bound to the required wavelength, since the wavelength determines the required composition of the solution *x*, which is the main growth parameter of the bulk structures. For $Hg_{1-x}Cd_xTe/Hg_{1-y}Cd_yTe/Hg_{1-x}Cd_xTe$ QWs, the bandgap is determined at given temperature and pressure, by three parameters - composition of the barrier layers, width of the QW and the composition of the solid solution in the QW, each parameter affecting the band structure of the QW.

This paragraph presents the studies of long-wave SE in HgCdTe-based heterostructures and the influence of Auger recombination as the most important channel of non-radiative recombination in dependence. The latter is done using the calculations of the threshold energy of CCHC-process (in initial condition there are two electrons in the bottom of conduction subband and one hole in the top of valence subband) for the selected designs of structures.

Figure 48 shows the spectra of SE of the investigated structures measured at 20 K. The control of the onset of SE was carried out by the start of superlinear growth of the signal and narrowing of PL

spectrum with increasing the pumping power in the same way as in [85]. Emission characteristics of the investigated structures are presented in **Table 4**. The critical temperature (CT) denotes the maximum temperature which is SE could be obtained. At temperatures above CT SE was "quenched" and only a wide spectrum of spontaneous PL was observed.

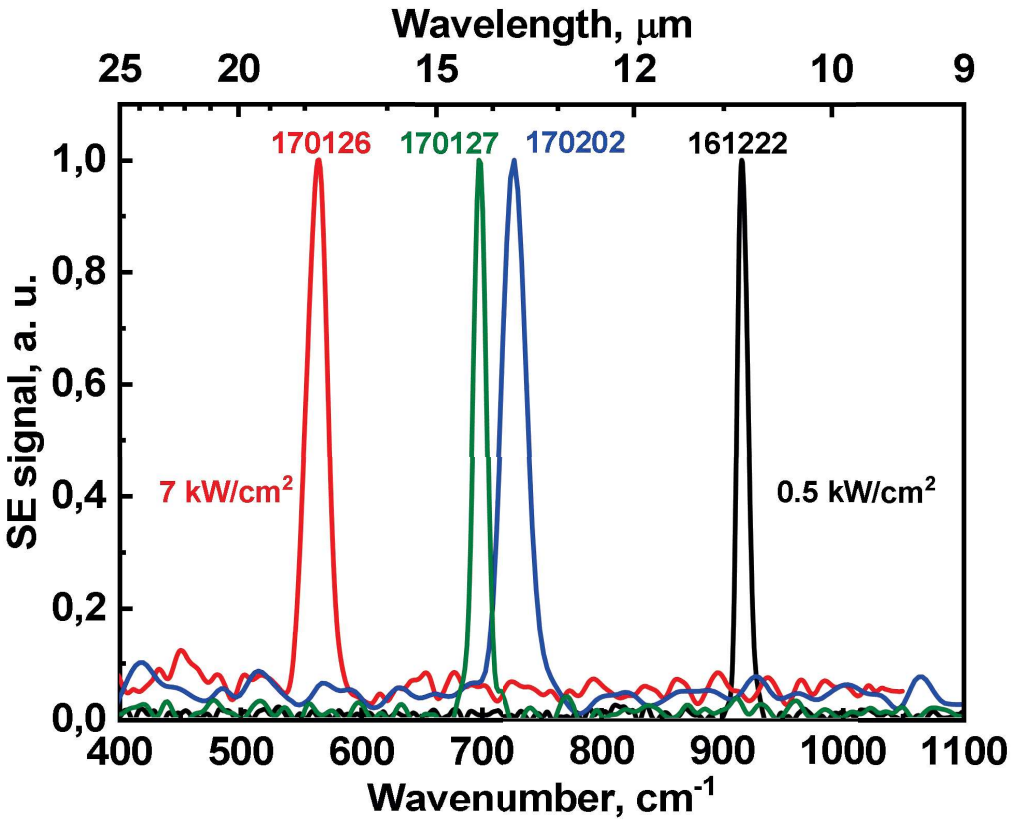

Fig. 48. Stimulated emission spectra of the investigated structures at temperature 20 K.

As it can be seen from **Table 4**, with increasing emission wavelength the threshold pumping power density also increases while CT decreases. Maximum SE wavelength of 18 μm was obtained from structure 170126 at power density of 5 kW/cm^2. Comparing the thresholds of structures 161222, 170127 and 17026 we speculate, that each increase in the wavelength by 4 μm results into corresponding five-fold increase in the threshold pumping power density. This trend suggests that even in structures with design of the active region similar to existing structures, the maximum wavelength that can be achieved is equal to 32 μm with the threshold of ~200 kW/cm^2.

Critical temperature, on the other hand, although growing on average with the SE wavelength, can differ substantially in structures with a close value of the bandgap. We relate such behaviour to the influence of the Auger recombination. As noted earlier, in narrow QWs the energy gap between the ground confinement levels and excited levels exceeds the bandgap, so non-threshold Auger recombination is prohibited. At the same time, the processes between the carriers of the ground quantization levels although demonstrating threshold behaviour, are generally allowed. Comparison of

experimentally determined CT values with the calculations of the threshold energy of Auger recombination, (E_{th}) showed that the maximum temperature of SE observation correlates with the threshold energy and is approximately half of E_{th}[K].

Table 4. Emission wavelength, critical temperature and pumping intensity thresholds, for studied waveguide structures

Sample	Wavelength at T=8 K, μm	SE threshold at T=8 K, kW/cm^2	Critical temperature T_{max}, K	Wavelength at T_{max}, μm	SE threshold at T_{max}, kW/cm^2
161222	10.9	0.2	100	9.4	10
150120	10.2	0.12	175	6.8	200
170202	13.7	1	60	11	160
170127	14.2	0.5	80	11.2	40
170126	18.6	5	40	16.8	7.5
180913	PL 18.5	-	-	-	-

In order to understand why the threshold energy value of recombination Auger-recombination energy differs in structures with different parameters of the QWs, we have analysed the calculations of the band spectrum . **Figure 49** shows the band spectrum of structure 170127 with 8.7 nm thick $Cd_{0.1}Hg_{0.9}Te/Cd_{0.65}Hg_{0.35}Te$ QWs (**Fig. 49(a)**) and the second structure having same bandgap but with $HgTe/Cd_{0.65}Hg_{0.35}Te$ QWs with a thickness of 4.2 nm (**Fig. 49(b)**). As it can be seen, for the structure 170127 the region of quasi-symmetry between electron and hole dispersion laws is rather narrow and lies around the region of k = 0 nm^{-1}. The first electron subband retains a quasi-relativistic form in a wide range of wave vectors, while the dispersion of the hole subband is non-monotonic, due to the presence of side maxima - additional extremes of dispersion law at non-zero k.

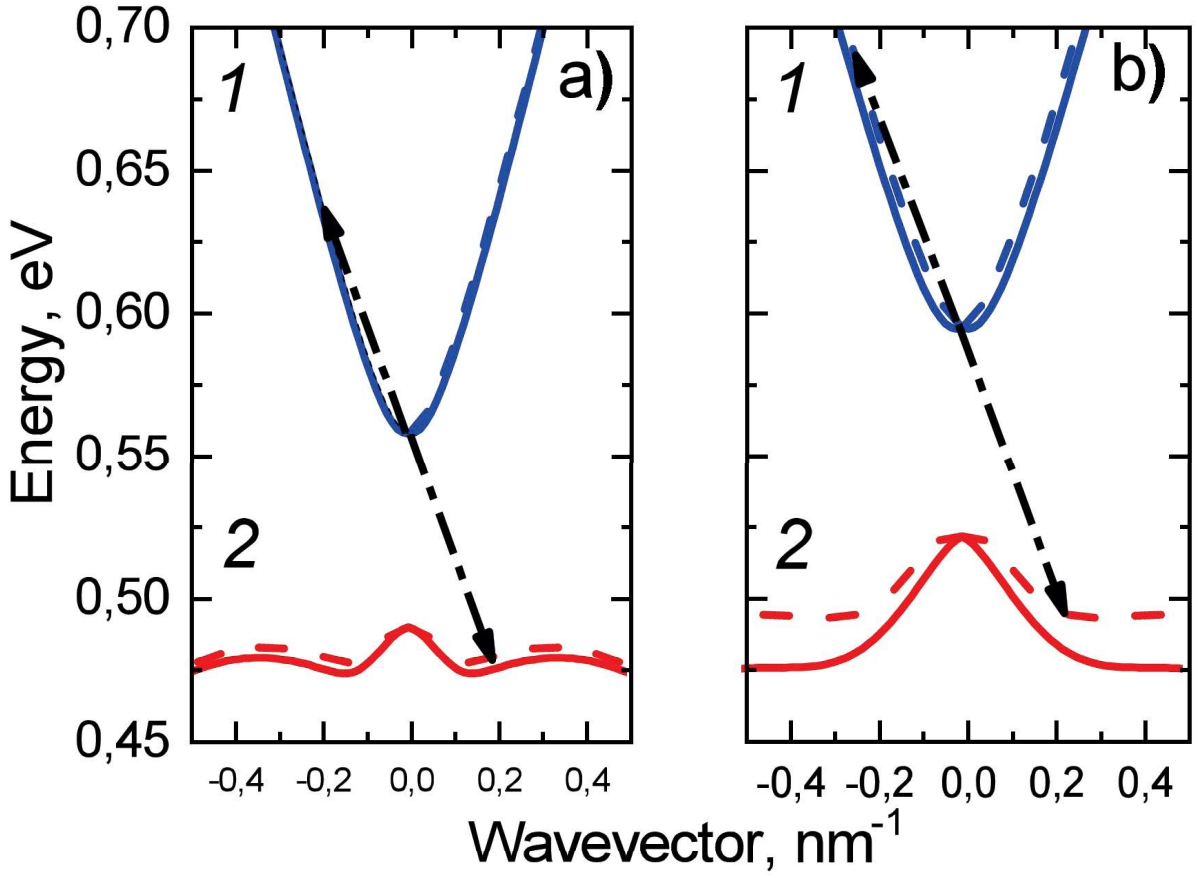

Fig. 49. Calculations of the energy band structure of (a) 8.7 nm wide $Cd_{0.1}Hg_{0.9}Te/Cd_{0.65}Hg_{0.35}Te$ QW and (b) 4.2 nm wide $HgTe/Cd_{0.65}Hg_{0.35}Te$ QW. The temperature is equal to 20 K. The wavevector is directed along the [100] axis. The band structure consists of two pair of electron and hole subbands due to spin-splitting (solid and dashed curves). 1 – electron subbands, 2 – hole subbands. The arrows indicate the transitions of the electrons corresponding to threshold CHCC Auger process.

Since the threshold energy of a process involving two electrons and a hole (CHHH-process) is several times higher than the threshold energy of the process involving two electrons and a hole (CCHC-process), at the critical temperature is determined by the latter. To illustrate the difference between the ongoing processes in different QWs, the lowest initial and final states of the carriers able to take part in Auger-recombination are shown in **Figure 49** with arrows. Comparing the two cases one can see that the momentum of the holes involved in Auger process in binary HgTe and $Cd_{0.1}Hg_{0.9}Te$ QWs is almost the same, but the energy (counting from the top of the valence band) of the hole is significantly smaller than in a QW with non-zero cadmium content. It is due to the presence in Cd0.1Hg0.9Te quantum wells aforementioned side maxima, which leads to an increase in the "effective mass" of holes occupying the states away from zero *k*. It is well known that an increase in the effective mass of holes leads to a decrease in the threshold energy of the Auger process, so, the

more pronounced side maxima are, the lower is Auger recombination threshold. (It should be noted that the term "effective mass" used here is conditional on the upper valence subband, since the law of dispersion in it is not quadratic and, generally speaking, non-monotonous. Here, this term should be understood as a value providing a connection between the kinetic energy of a hole and its wave vector. The greater wave vector at fixed kinetic energy, the higher "effective mass".)

Thus, the main goal of band structure engineering in HgCdTe QWs is to reduce the influence of side maxima of dispersion of the holes. As **Figure 47** demonstrates, the reduction of cadmium content in the wells leads to almost twofold increase in the threshold energy of Auger recombination, and as a consequence, an increase in CT. This result was confirmed by the comparison of CT in investigated structure 160122 with the results obtained earlier in the structure 150120 (**Table 4**). Both structures have the bandgap of 125 meV, and similar optical quality (**Fig. 41**), however, in structure 150120 SE was obtained at temperatures up to 175 K, while in structure 161222 SE quenching occurs at 100 K.

The results above show that the use of structures with narrow wells made of pure HgTe can significantly increase CT and increase the maximum possible wavelength of SE by suppressing Auger-recombination involving the holes in the side maxima of the valence band. In general, a reduction of the energy of side maxima keeping a fixed bandgap can be achieved not only by reducing cadmium content in the well, but also by decreasing cadmium content in the barriers simultaneously. To estimate the effect of this parameter, we have calculated and investigated the dependence of the threshold energy of Auger-recombination on the Cd content in the barrier layers $Hg_{1-x}Cd_xTe$ at the same time varying the thickness of HgTe QW, to ensure the conservation of optical transition energy between the main electron and hole subbands in the vicinity of 70 meV (corresponding wavelength ~ 18 μm). The results of the calculations are shown in **Figure 50**.

Two sets of curves (solid and dash) represent the width of a QW and the threshold energy of Auger recombination at 8 and 77 K. Black square corresponds to the studied structure 170126. In this structure with 8.7 nm $Cd_{0.1}Hg_{0.9}Te$ QW and $Cd_{0.65}Hg_{0.35}Te$ barriers, SE at 18 μm wavelength was obtained at 20 K and the maximum temperature of SE observation was equal to 40 K. The threshold energy calculated for the CHCC process for structure 170126 is about 10 meV. As **Figure 50** shows, the threshold energy for the structures with binary HgTe QWs is significantly higher and only slightly decreases with temperature.

At the same time as one can see, the dependence of the threshold on Cd concentration is non-monotonous with the maximum lying in the area x=0.7. Above this value the threshold value is almost constant, but when the Cd concentration is lower, it rapidly decreases, almost approaching the threshold energy for the structure with $Cd_{0.1}Hg_{0.9}Te$ QW.

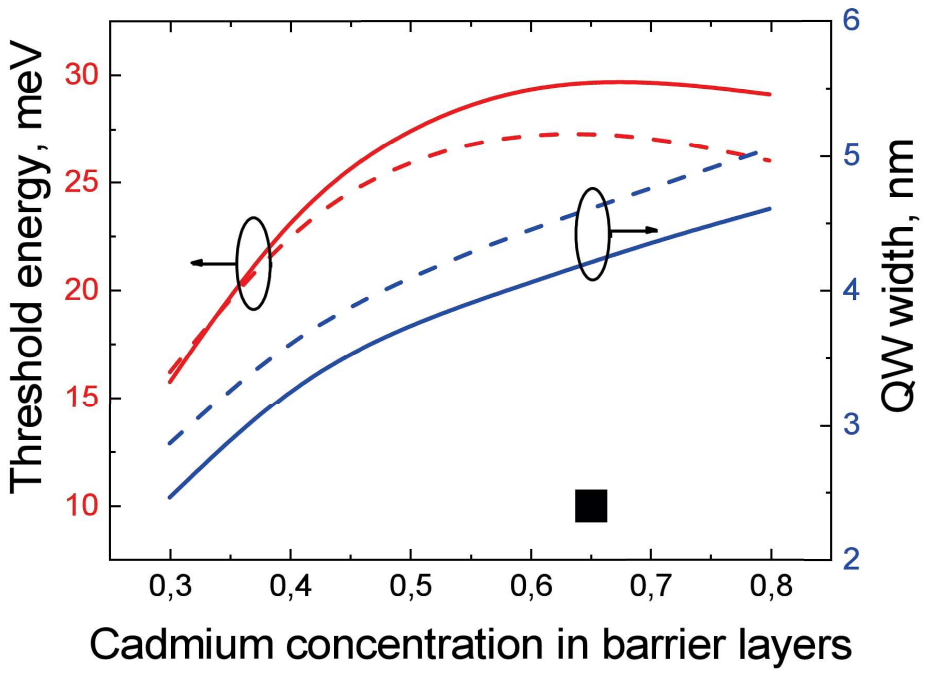

Fig. 50. Threshold energy of CHCC Auger recombination and HgTe QW width versus the content of Cd in barriers at a fixed energy of optical transition equal to 70 meV calculated for two temperatures: 20 K (solid curves) and 77 K (dashed curves). Square shows the threshold energy of structure 170126 with 8.7-nm-wide $Cd_{0.1}Hg_{0.9}Te/Cd_{0.65}Hg_{0.35}Te$ QW.

In order to understand the reason of such behaviour of the threshold energy dependence of the process Auger process let us turn again to the calculations of the spectra of electronic and hole levels. The results of calculations for a) in trinary well with "high" barriers, b) binary well with "high" barriers and c) trinary well with "low" barriers are shown in **Figure 51**. **Figure 51 (a)** shows that for the first case, there are additional maxima in the valence subband 7 meV lower in energy than the top of the valence band. In the HgTe well surrounded by $Cd_{0.65}Hg_{0.35}Te$, these extrema are practically absent (**Fig. 51 (b)**), while in the structure with 5.7 nm wide $Cd_{0.1}Hg_{0.9}Te/Cd_{0.3}Hg_{0.7}Te$ QW they are weakly pronounced and lie 10 meV lower than the main maximum (**Fig. 51 (c)**).

The reason of why the third case is the worst lies in the dispersion of holes in the vicinity of k=0. We can see that the dependence in **Figure 51 (c)** is more "flat" than in panels **a)** and **b)**. This means that a decrease in cadmium content in the barriers leads to an increase in the effective mass of holes in the valence band's main maximum area. Thus, the condition of symmetry of dispersion of electrons and holes is not fulfilled and the Auger-recombination channel opens at lower energies, which is reflected in the graph of threshold energy dependence in the form of a sharp drop.

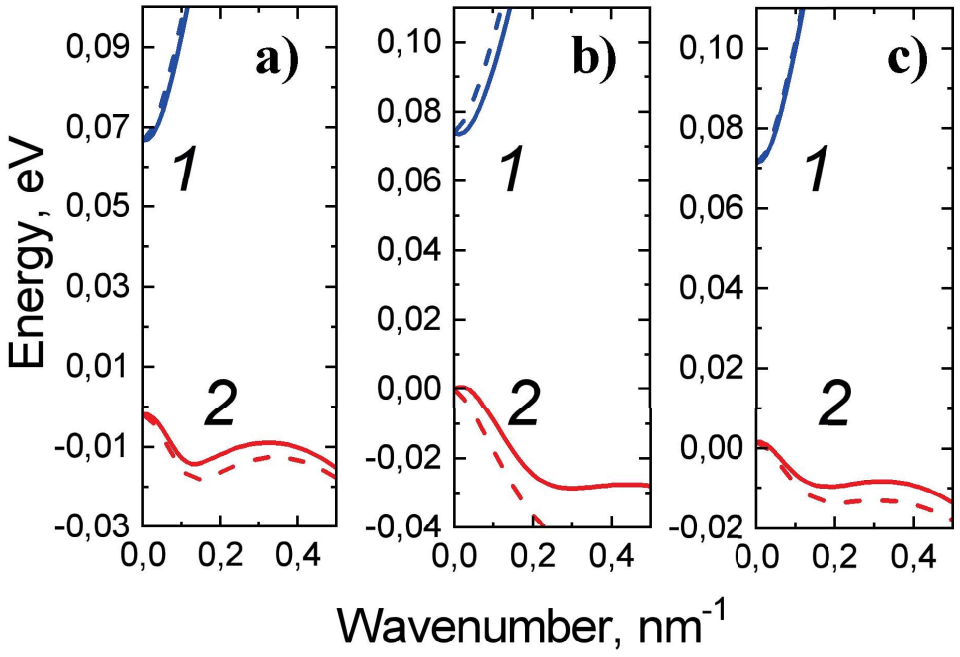

Fig. 51. Energy band structure of first conduction and valence subbands at 20 K, calculated for (a) $Cd_{0.1}Hg_{0.9}Te/Cd_{0.65}Hg_{0.35}Te$ QW with 8.7 nm width, (b) $HgTe/Cd_{0.65}Hg_{0.35}Te$ QW with 4.2 nm width (c) $Cd_{0.1}Hg_{0.9}Te/Cd_{0.3}Hg_{0.7}Te$ QW with 5.7 nm width. The wavevector is directed along the [100] axis. The band structure consists of two pair of electron and hole subbands due to spin-splitting (solid and dashed curves). 1 – electron subbands, 2 – hole subbands.

To test the emissivity of the structures with different composition of the barriers we have studied PL spectra in continuous and pulsed modes in structures with close bandgap, but with different core designs. The first structure had 7.4 nm wide $Hg_{0.903}Cd_{0.097}Te/Cd_{0.7}Hg_{0.3}Te$ QWs and the second had 5.7 nm wide $Cd_{0.1}Hg_{0.9}Te/Cd_{0.3}Hg_{0.7}Te$ QWs (structures 170126 and 180913). **Figure 52** shows the spectra of PL in continuous mode in these structures. As one can see from the signal-to-noise ratio, the spontaneous PL intensity in both structures has similar amplitude, due to the low rate of Auger recombination at low intensity of optical pumping. However, under pulsed pumping SE can be obtained only in structure 170126 (See **Fig. 48**), which is observed up to 40 K, while in the structure 180913 we were not able to find any signal under pulsed pumping.

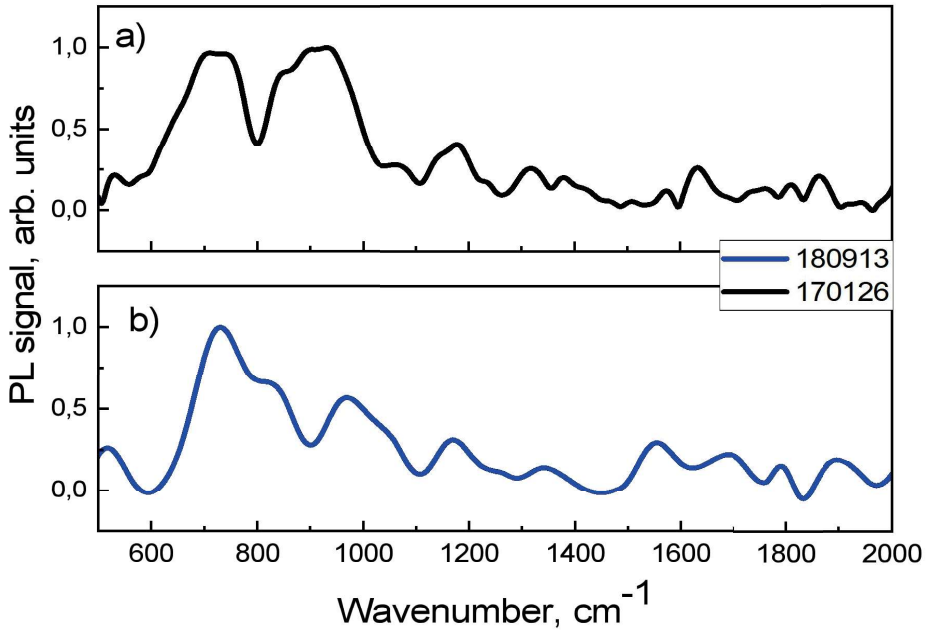

Fig. 52. PL spectra measured at 8 K under 808-nm continuous excitation of a) structure 170126, b) structure 180913.

It should be noted that the threshold energy calculations of Auger recombination above were performed for a fixed wavelength of radiation. At the same time, as **Table 4** demonstrates, in the investigated structures the emission wavelength decreases with temperature growth. The biggest interest for the design of future structures is the CT dependence on the wavelength, which will allow to obtain SE for a given wavelength at maximum temperature. To estimate the maximum CT achievable at a certain wavelength (T_{max}), it is possible to use empirical expression $T_{max} \approx E_{th}/2$.

As an illustration of this approach, we have considered a series of six HgCdTe heterostructures with an optimal design of the active region (binary HgTe QWs with widths from 3.8 to 6.4 nm, separated by barriers with 70 percent Cd content). All the structures reach the bandgap of 90 meV (corresponding wavelength 14 μm) at a certain temperature (T_{90}), specific for each structure and determined by the width of the QW. For each structure the band spectrum and possible configurations of Auger processes were calculated. **Figure 53** shows the dependence of the threshold energy of the CCHC-process for the investigated structures. The threshold energy of Auger-recombination is lower in structures with high T_{90} (and wide QW) than in structures with low T_{90} (and narrow QW) going from 40 meV in structure with minimal T_{90}, equal to 8 K up to 19 meV in a structure with the largest T_{90}, equal to 300 K. In order to estimate the highest possible CT of SE we have plotted a linear plot of $E=2T$ where the temperature is measured in energy units (dashed line) in the same coordinates, as the T_{90}. The crossing between these plots indicates the point above which Auger-recombination must

be effective enough to suppress the SE, which limits the operating temperature of lasers to 14 μm on HgCdTe with pure HgTe to the region T < 175 K.

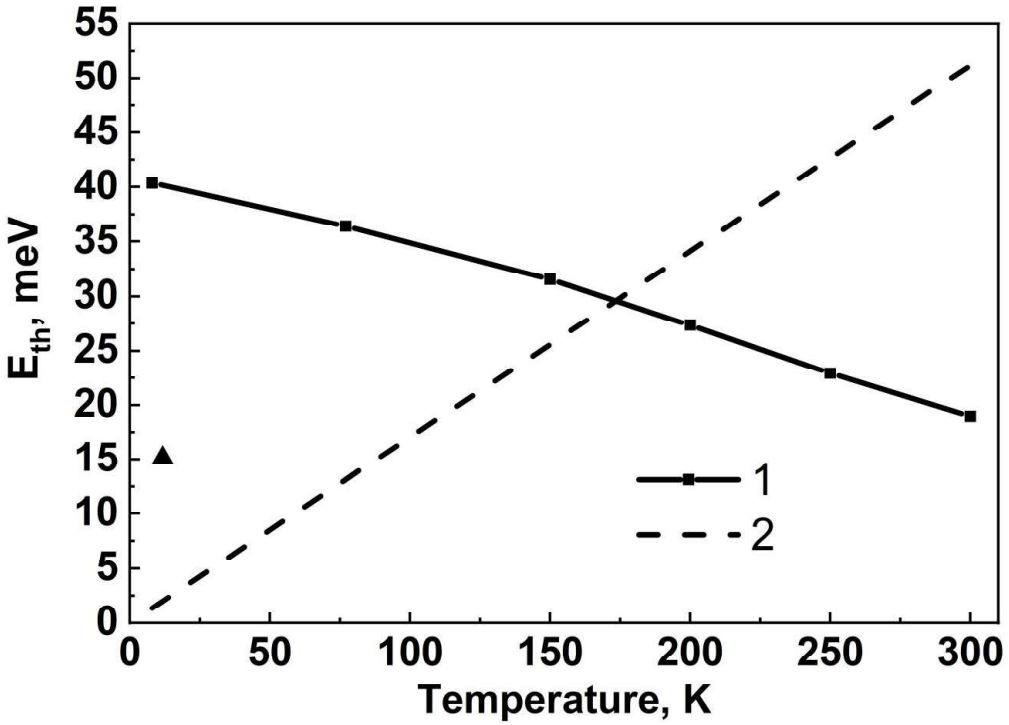

Fig. 53. Threshold energies of Auger recombination of HgTe/$Cd_{0.7}Hg_{0.3}Te$ with QW widths from 3.8 to 6.4 nm at T_{90}. (squares). Dashed line (20) is the plot of function $E = 2T$ where [T] = meV. The threshold energy of Auger recombination of structure 170127 is shown for comparison (triangle).

Summing up, the results suggest that the recombination threshold, which is the main factor leading to the suppression of Auger recombination in long-wavelength HgCdTe heterostructures structures with QWs, can be significantly increased in structures with properly selected parameters. Calculations of band structure and Auger recombination threshold energy show that HgTe/$Hg_{1-x}Cd_xTe$ QWs, where x_{Cd} - lies in the range 0.6-0.75, is optimal for obtaining SE. This result is confirmed by direct measurements of the CT for SE in a series of waveguide structures with different active region designs, designed for the wavelength range from 7 to 18 μm. The resulting characteristics of the pumping power density threshold suggest a further increase in the wavelength up to at least 30 μm. The results presented in this chapter are published in [124–127]

4.7 Effect of pumping wavelength on SE characteristics in the long wavelength region

During the studies of SE under intensive optical pumping we have found that despite relatively low pumping power thresholds (**Table 4**), at low temperatures, above the threshold of pumping power, the signal increases linearly up to a certain power, then saturates and begins to decrease

The dependence of the integral radiation intensity of the structure 170127 on the pumping power at different temperatures is shown in **Figure 54**. In contrast to the threshold pumping intensity, the "quenching intensity" (QI), i.e. the photon flux at which the PL signal is maximal, is independent of temperature. The most interesting dependence is observed at temperatures close to the critical one. In particular, at T=60 K, the emission intensity with pumping growth develops as a "threshold - growth - attenuation - growth" law, and the growth rate in the area of high intensities differs from the growth rate just above the threshold. At temperatures above 70 K the signal grows monotonically up to the highest pumping power, although one can see a kink in the graph after which the growth rate slows down.

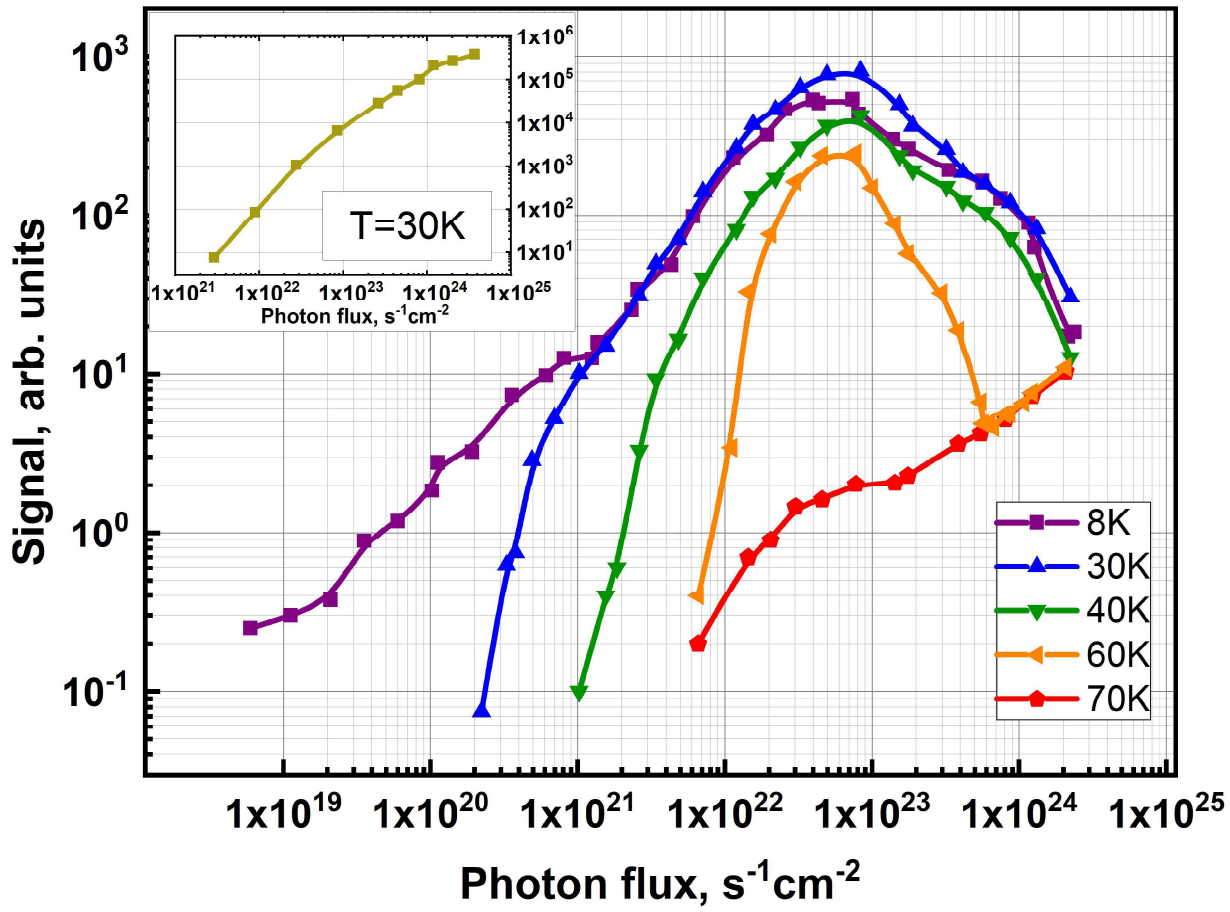

Fig. 54. Integral SE intensity dependence on the excitation photon flux for structure #1 and 2.3 μm excitation at different temperatures. Typical dependence for 10.6 μm excitation is presented on the inset.

We attribute such complex behaviour of the signal to the heating of the electronic system by high-energy pumping radiation. In order to release the excess energy received after generation, the electron-hole pair must emit more than 30 optical phonons (the energy difference between the initial

and final states of the pair is approximately ~453 meV for excitation at 2.3 μm wavelength, while the energy of the most energetic optical phonon in HgCdTe is 15 meV).

The observed phenomenology suggests that the amount of heating carriers receive is proportional to their concentration. When concentration of non-equilibrium carriers is small, heating practically does not affect the intensity of SE and we observe typical threshold behaviour. As excitation increases the additional electron-hole pair introduce more energy to the system and the heating effect overcomes the amplification of radiation.

This behaviour can be caused by two possible mechanisms. First, high concentration of electrons can lead to their “back-heating” by non-equilibrium phonons: at high density of electrons and phonons part of the latter has time to be reabsorbed by the electron gas before the lattice thermalization. Due to this effect, the transfer of energy from the electron gas to the lattice takes more time and carriers remain in the non-equilibrium state during the emission. The second factor that slows down the cooling of the media is the Auger-recombination. Since the energy of the recombining electron-hole pair during the Auger processes is carried away by a third carrier, it contributes to the total temperature of the non-equilibrium electron-hole plasma. The probability of Auger-recombination increases as a cube of carrier concentration, so it is obviously much higher at high pumping intensity. At the same time, the thermalization of electron gas occurs over a shorter time, so at a certain pumping power, the carriers reach a quasi-equilibrium distribution with a temperature higher than the temperature of the lattice. If this temperature remains high enough for a long time in comparison with the lifetime of the electron-hole pair, it leads to the broadening of the modal gain and quenching of the SE.

The heating of the electron gas can be reduced by excitation with lower photon energy. In our experiment we used pulsed CO_2 pumping with 10.6 μm wavelength. As the **inset of Fig. 54** demonstrates, under 10.6 μm wavelength excitation, the quenching of SE was not observed even at a greater number of photons in the pulse than under 2.3 μm pumping. It should be noted that direct comparison between these two cases is not possible due to different absorption coefficients and the use of TPX filter to cut-off CO_2 radiation. However, the spectra measured under excitation corresponding to the lowest point of the curve in the **inset of Fig. 54** indicate that at such power we observe SE, thus it lies above the threshold. As the pumping intensity ranges from $2 \cdot 10^{21}$ to $3 \cdot 10^{24}$ the number of generated carriers increases by over three orders of magnitude marginally exceeding the value obtained under 2.3 μm pumping.

Our results show that under excitation with low photon energy, the quenching of SE due to the heating of the carriers is reduced. We assume that this is a consequence of the lower energy of the electron-hole pairs generated, as they are able to descend faster to their ground state. Moreover, as mentioned earlier, Auger-recombination is suppressed in narrow HgCdTe QWs due to the proximity of

effective masses of electrons and holes in the vicinity of the Γ point, and rapid development of Auger-recombination begins when the holes reach lateral maximums of the dispersion curve. Carriers generated by long-wavelength pumping have low energy and, accordingly, are close to the bottom of the conductivity band and the top of the valence band, and are not able to participate in Auger-recombination significantly decreasing its rate.

The picture of the occurring physical processes becomes more evident when considering spectral features of the observed PL signal. **Figure 55 (a)** shows the emission spectra of structure 170127, measured at 10 K. When the pumping power exceeds the threshold value, a narrow peak of SE appears at the red (long-wave) edge of the PL line. Its width at half height is approximately ~1.5 meV. As the pumping power increases, the SE line widens and gradually shifts towards high energies. At the point of the QI, the integral signal reaches its maximum, and the width of the SE line approaches ~2 meV, while remaining significantly narrower than spontaneous PL. The shift and broadening of the SE line indicate the population of the states with higher energies by hot electrons. It should be noted that qualitatively similar effect can be achieved in a system with "cold" carriers, but in order to observe the same amplitude of the shift, the concentration of the carriers must exceed the number of photons in the pumping pulse. Thus, the changes of the SE spectrum are most coherently explained by the heating of carriers by energetic excitation photons. At higher pumping intensities we observe a splitting of the SE line into three less intensive lines. Competition between the individual modes leads to less effective amplification and, as a result, to the quenching of SE.

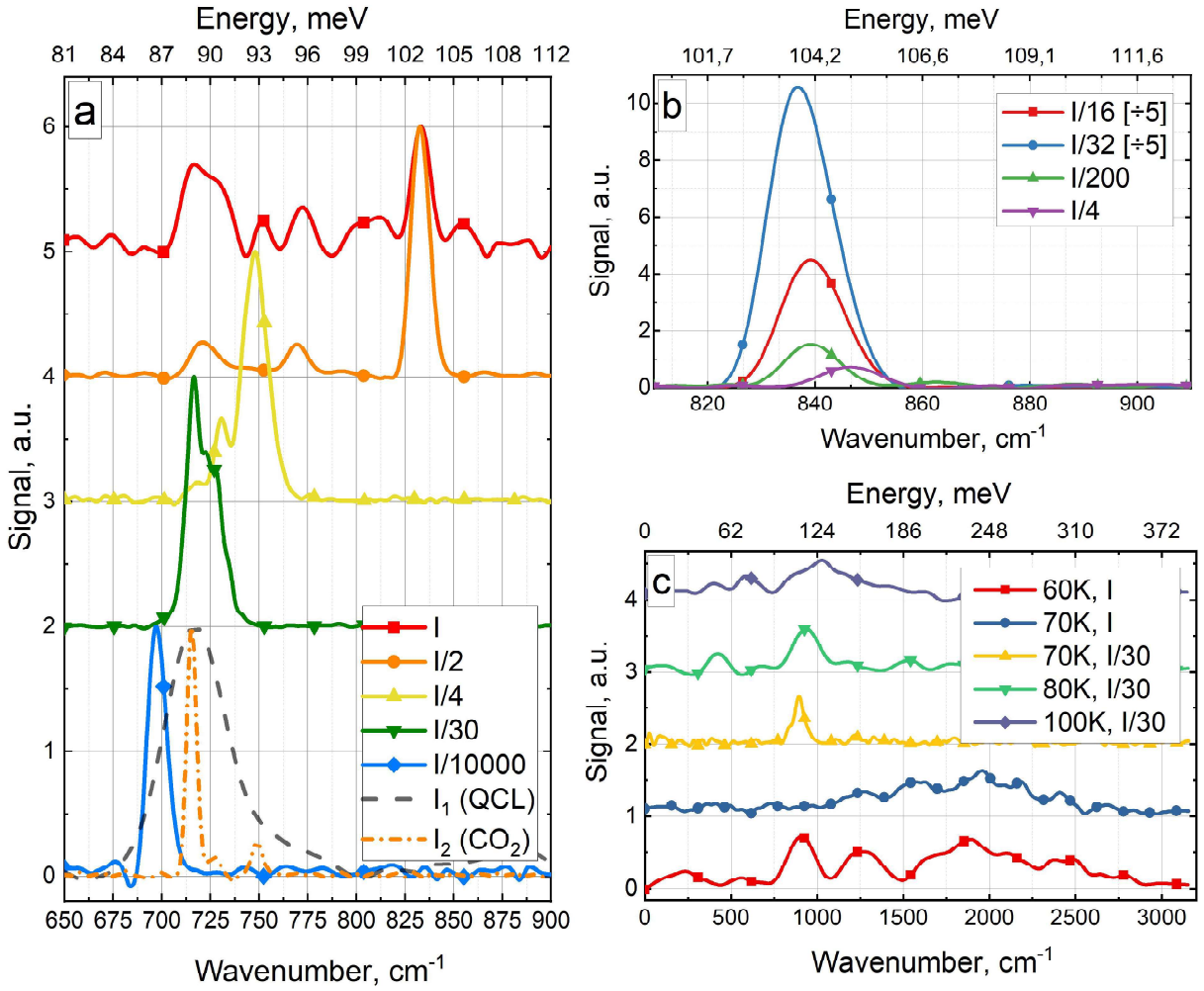

Fig. 55. SE and PL spectra from structure 170127 obtained at different conditions: (a) T=10K; λ_{exc} = 2.3 μm (solid curves), λ_{exc} = 10.6 μm (dash dot curve), λ_{exc} = 8.3 μm (dash curve) (b) T=60K; λ_{exc} = 2.3 μm (c) different temperatures; λ_{exc} = 2.3 μm. Excitation intensity I corresponds to $2 \cdot 10^{22}$ $s^{-1}cm^{-2}$ photon flux, I_1 corresponds to 10^{18} $s^{-1}cm^{-2}$ photon flux, and I_2 corresponds to 10^{24} $s^{-1}cm^{-2}$ photon flux.

At T=60 K, the position of the SE line is stable both at low intensities and in the middle range when the integral signal decreases (Compare **Fig. 54 and Fig. 55 (b)**). However, as the integral signal begins to rise again, we observe a wide spectrum of spontaneous radiation that accompanies the SE line (**Fig. 55 (c)**). As the temperature of the structure increases, the amplification profile becomes so wide that it does not exceed the losses at any one point, and the spectrum has only the spontaneous luminescence of hot carriers. It can be seen that the red boundary of the spontaneous PL is the same as the SE line obtained at lower pumping powers. Therefore, observation of "hot" PL indicates the presence of carrier heating and depopulation of low energy states. Spontaneous PL is not sensitive to the distribution of the carriers, so the growth of the integral signal at high pumping power is due to increasing contribution from the spontaneous PL.

Above QI at temperatures above 70 K, the spectrum is dominated by the spontaneous PL with temperature and intensity increasing monotonically with the pumping power. At low excitation levels, we observe weak "cold" PL lines, the position of which corresponds to the bandgap of the structure (**Fig. 55 (c)**). Speaking about "cold" PL, we assume that at temperatures above 70 K the QI lies is below the threshold intensity, so the SE cannot occur at any excitation, as the negative effect of carrier heating suppresses the gain.

In contrast, when using of long-wave excitation, even in the case of maximum power, the SE line "warms up" by less than 2 meV (**Fig. 55 (a)**), which indicates that the induced heating of carriers is much less than that of the short-wavelength excitation. This result suggests that in the case of long-wavelength pumping, when the heating of the carriers is weak, it is possible to increase the operating temperatures in structures under study.

The advantage of long-wavelength pumping is confirmed by conducting the experiments on the structure 170126 with the bandgap of approximately 60 meV. In this structure under 2.3 μm pumping SE was obtained only in a few experiments at practically one pumping intensity (the 3-fold increase of pumping power over the threshold already lead to the SE quenching), while using excitation with a wavelength of 10.6 μm, we observed SE in a wide range of power densities at temperatures up to 40 K. At the same time, we should note that when investigating the structure with a smaller gap, saturation of the signal with pumping intensity was observed even under 10.6 μm excitation (**Fig. 56**).

Thus, even the energy of photons produced by CO_2 laser may be too high to initiate SE in HgTe/HgCdTe structures with wavelengths greater than 30 μm. However, even if heating at long wavelengths is significant, at the moment, with the use of CO2 pumping, heating of carriers does not lead to the quenching of SE, which suggests the possibility of further increase in the SE wavelength.

Concluding, contrary to previous sections, which were focusing on the internal parameters of the structure, main goal of this part of the work was to investigate how the properties of SE are influenced by external factors. We investigated the emission spectra and intensity from structures emitting at 14 and 18 μm at different temperatures and excitation intensities at two different excitation wavelengths. The results show that short-wavelength excitation (λ=2.3 μm) at high intensities increases the temperature of the electron gas. This effect intensifies at higher power of excitation and lower bandgap of the structure. As a result, dependence of SE signal on pumping intensity is non-monotonous and there is temperature-independent optimal intensity. The most important effect that was found in this part of the work is weaker heating under long-wavelength excitation, which demonstrates its advantage in future attempts of increasing the emission wavelength. These results were published in [128].

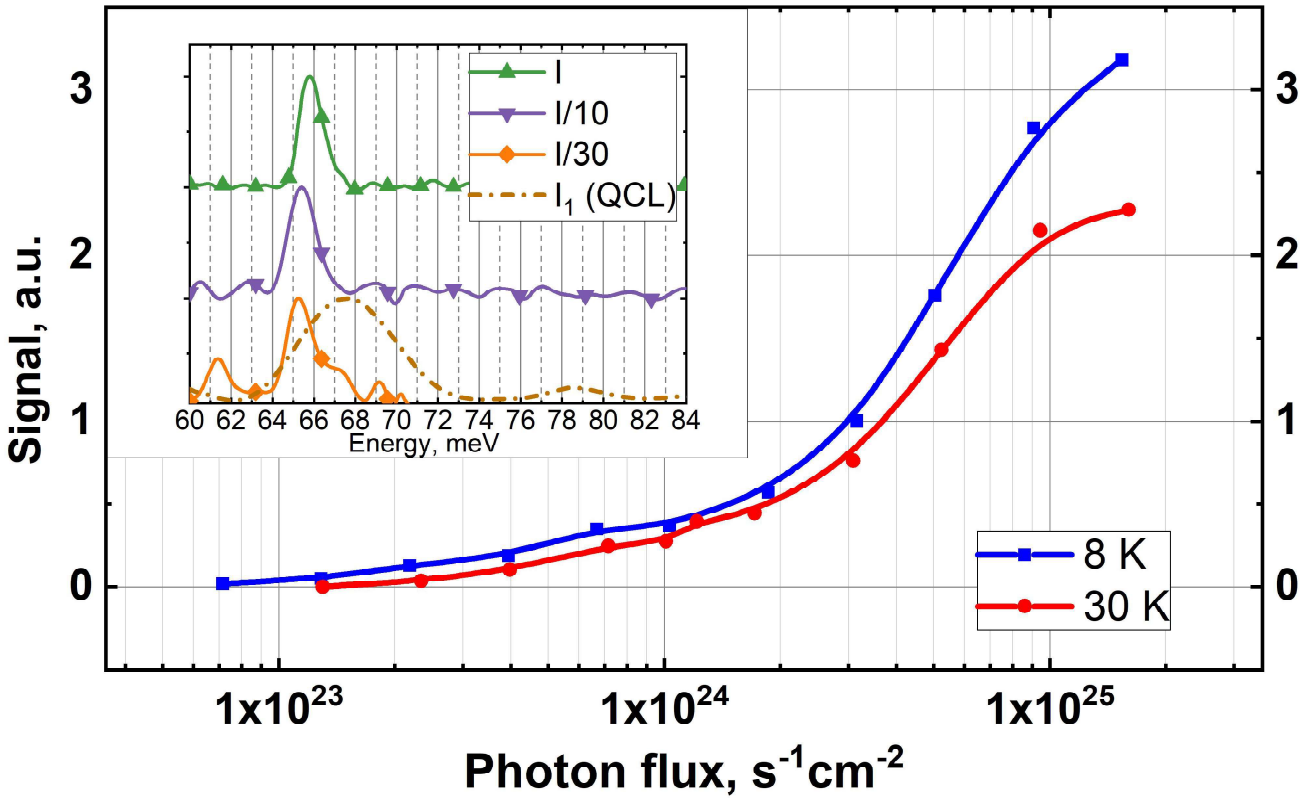

Fig. 56. SE and PL spectra at 30 K (on the inset) and integral SE intensity dependence on the excitation photon flux for structure 170126 and CO_2 laser excitation. Excitation intensity I corresponds to 10^{24} $s^{-1}cm^{-2}$ photon flux.

4.8 Summary

In this chapter we studied the prospects of HgCdTe-based heterostructures with QWs to be used as long-wavelength radiation sources. In a series of waveguide heterostructures with QWs of thickness from 6.1 nm to 7.6 nm SE under optical pumping was obtained up to 18 μm. Despite the growth of the pumping threshold intensity with radiation wavelengths from 0.2 kW/cm2 at 10.9 μm to 5 kW/cm2 at 18 μm, in absolute terms this value remained relatively small and more than 2 orders of magnitude less than the maximum optical excitation power strength that can be used without damaging the heterostructure. Thus, the obtained results demonstrate the possibility of further increasing the wavelength and damping temperature of radiation in HgTe/CdHgTe based heterostructures.

In order to improve the characteristics of SE we analysed the influence of parameters of QWs lying in active region of waveguide heterostructure on the characteristics of SE. It is shown that the CT of SE can be with high accuracy defined using the calculation of AR threshold, which can be maximized by adjusting cadmium content in the material of QWs and barriers and therefore its band structure. The results of the calculations of AR threshold in structures of different design give evidence that thin wells made of binary HgTe with high cadmium content (~0.7) barriers. This theoretical result was confirmed by the measurements of SE spectra from structures with equal bandgap but different QW parameters.

Finally, we evaluated the effect of optical pumping wavelength on the characteristics of SE from HgCdTe heterostructures. The use of short-wavelength optical excitation at high (>10^{23} photons in pulse) power was shown to lead to heating of carriers and quenching of SE. At the same time, pumping with a wavelength of 10.6 μm did not cause carrier heating up to $3*10^{24}$ photons in the pulse, and hence is preferable for obtaining SE in the long wavelength range.

Conclusions and Outlook

The object of this thesis was to investigate the properties of the band structure of Hg(Cd)Te/HgCdTe and AlSb/InAs/Ga(InSb)/InAs/AlSb heterostructures. An important property of these material systems is the ability to tune their bandgap across the far-IR and THtz range. This makes these materials indispensible for creating IR detectors. and at certain parameters make the gap inverted, which results into the formation of novel phases of matter, known as topological insulators. The experimental part of this thesis is divided into three main parts according to the investigated system. Probing of the band structure is performed by Fourier transform magnetoabsorption and photoluminescence techniques, the experimental set-ups for which are given in Chapter 2.

The first experimental part is devoted to the studies of type-II heteostructures on the basis of InAs/Ga(In)Sb. The studies focus on the experimental probing of the new W-shaped quantum wells which were suggested as a possible candidate for fabrication of high-temperature topological devices At the state of art the current through the edge channels, which is a direct demonstration of the topological insulator phase was observed only at extremely low temperatures or in exotic monolayer materials. The main problem that scientists face is a very small value of the inverted bandgap which can be achieved in semiconductor systems. One of the possible solutions is to make more complex heterostructures in the basis of already-known topological systems which would allow increasing the bandgap. This idea was recently applied to the InAs/Ga(In)Sb CQWs. The bulk band gap in such structures is formed due to the hybridization gap between electron and hole levels in different layers.. So far, the topological insulator state was investigated only in the two-layered heterostructures InAs/GaSb. However, due to the lack of the symmetry of the structure in growth direction the inverted bandgap opened at non-zero k and is small compared to HgTe/CdTe heterostructures. In this works we investigated three samples with symmetrical TQWs. We performed their characterization by the means of magnetoabsorption and photoluminescence spectroscopy in order to prove the expected value of the bandgap prior to the actual transport measurements

The first studied structure was TQW InAs/GaSb/InAs, which was designed to have the highest possible bandgap which can be achieved without using the strained layers. The results of magnetoabsorption confirmed the predicted value of the bandgap of 16 meV and revealed that the spectra contain the absorption line associated with the interband transition. The last result confirmed that the band structure of the studied sample is inverted, which is a necessary condition for the formation of TI phase. The measurements performed at different temperatures demonstrated that the bandgap of the inverted TQW heterostructures does not change with temperature, which is an important adbvantage over HgTe/CdTe QWs, for which high values of the bandgap can be achieved only at low temperatures.

The second sample had parameters of the QWs close to the first studied structure but it was grown on a different buffer layer, which results in a strain of the active layer. As a result the bandgap of this sample becomes indirect and it is semimetal. The magneoabsorption spectra confirmed the inverted band structure of the sample, but in order to determine the value of the indirect bangap the additional photoluminescence measurements were required.

The third studied structure is the first step towards practical high temperature topological insulators. The design of the third structure utilises strained layers as in the second structure and the optimized geometry for the given strain as in the first structure. The resulting bandgap value obtained from the magnetoabsorption spectra was found to be 38 meV, which is an over seven-fold increase compared to CQW InAs/GaSb heterostructures. Importatntly, the temperature-dependent measurements showed that the bandgap is constant as for the first structure, which shows that it can be used in the fmodel transport experiments attempting to find the edge current in TQW systems at temperatures above liquid helium temperature.

The second part of the thesis presented in Chapter 3, deals with the heterostructures on the basis of HgTe/CdHgTe QWs which has the same geometry as A3B5 structures studied in the first part of the work. Despite the apparent similarity in the shape of the heterostructure, the purpose and the consequences of designing such structures is very different. One of the most appealing properties of the HgTe DQW heterostructures is the ability to mimic the bandstructure of bilayer graphene – gapless state with parabolic conduction and valence bands touching at zero quasimomentum. The interest to such system is that its bandgap can be manipulated many external parameters: temperature, pressure, electric and magnetic fields, even by illumination. Moreover, when the band structure of the DQW is similar to bilayer graphene, topological insulator phase in it can be switched on and off by applying external field. It makes this system an interesting playground for studying the interaction of topologically non-trivial coupled QWs.

In this chapter we experimentally studied the temperature evolution of two samples with HgTe DQWs. We establish the way to determine the band order for the studied system on the basis of MA spectra and apply it to both samples. The first sample at low temperatures is characterized by inverted gapless band structure and experiences topological phase transition at the critical temperature T_c = 40 K accompanied by a change of band order to non-inverted. This phase transition is similar to the one observed earlier in single HgTe QWs. At the same time this case has its own peculiar properties: below the point of temperature driven phase transition the band structure of DQW remains gapless, in a wide range of the temperatures, while at critical temperature there are not Dirac fermions, but Kane fermions as in the bulk HgCdTe layers.

The second sample has the behaviour opposite to the first DQW sample. At low temperature it has non-zero inverted bandgap, but above the critical temperature of 25K, it transitions into the BG graphene state, which corresponds to the first structure at low temperature. Moreover, our results indicate that at higher temperature of approximately 150 K, the second structure experiences second phase transition into a normal band-insulatror state. Such behaviour is very unusual as it implies that the topologically non-trivial state can be found only in confined space of the parameters, while trivial phase take the rest of the diagram. Such behaviour can not be found in “classical” phases of matter regulated by the symmetry breakings.

The goal of the third part of this thesis is to develop physical basis for creation of the new type of far-IR and THz sources on the basis of HgTe/CdHgTe heterostructures. The main fundamental effect that enables the SE on the interband transitions in far IR range is the suppression of Auger recombination (non-radiative three-particle process, which transfers the enegy of recombined electron-hole pair to the remaining carrier) in structures with some dispersion laws. One example of such dispersion is the quasirelativistic dispersion with non-zero mass, which is found in the HgTe/CdHgTe QWs with thicknesses close to critical. Such dispersion appears owing to the strong interaction between the quantization subbands in HgTe QW, which is also responsible for the formation of the TI states. At the same time, when the QWs are getting thicker, the interaction between the subbands weakens and properties of SE become strongly dependent on the band structure of the QW. Thus our experiments focus on the characterization of the structures by the means of MA and PL and the investigation of the properties of SE from structures with different dispersion laws.

In the first experimental series two structures with the same bangap but different band structure are compared. The thick QW with was not able to provide any emission under optical pumping except for the weak and broad line of spontaneous photoluminescence. At the same time, in a narrow HgTe QW SE was demonstrated in a wide range of temperatures. These results confirm that the band structure of the QWs is of paramount importance for the long-wavelength lasers based on HgCdTe. They also show that the narrow HgTe QWs are preferable for the studies of SE in mid- and far-IR range.

In the second experimental series we investigated a number of the samples designed to emit radiation in the range from 10 to 18 μm. We performed characterisation of the samples and investigated the connection of their band structure and important parameters of SE, such as the threshold pumping intensity and the critical temperature of SE. The findings show, that pure HgTe QWs with $Hg_{0.3}Cd_{0.7}Te$ barriers are optimal for obtaining SE, as out of all designs they host dispersion law which is the closest to the quasirelativistic.

In the third experimental series we compared characteristics of SE obtained under long-wavelength (10.2 μm) and short-wavelenth (2.3 μm) pumping. We have found that the measured intensity of SE

was decreasing at high values of the short-wavelength pumping power. On the other hand, for long-wavelength excitation SE was growing in the whole available power range and the maximum intensity was several orders of magniture higher that under short-wavlelength excitation. These results point the direction for the future studied if HgTe based sources.

Summing up, this thesis is dealing with the properties of the band structure of wide-spread semiconductor materials. The results show that this band structure is very flexible and allows creating the materials for the future optoelectronics and topological devices as well as radiation sources.

Bibliography

1. L. D. Landau, “On the theory of phase transitions. I.,” Zh. Eksp. Teor. Fiz. **11**, 19 (1937).

2. X. Chen, Z. C. Gu, and X. G. Wen, “Local unitary transformation, long-range quantum entanglement, wave function renormalization, and topological order,” Phys. Rev. B - Condens. Matter Mater. Phys. **82**(15), 1–28 (2010) [doi:10.1103/PhysRevB.82.155138].

3. J. M. Kosterlitz, “Nobel lecture: Topological defects and phase transitions,” Rev. Mod. Phys. **89**(4), 1–7 (2017) [doi:10.1103/RevModPhys.89.040501].

4. V. Berezinskiĭ, “Destruction of Long-range Order in One-dimensional and Two-dimensional Systems Possessing a Continuous Symmetry Group. II. Quantum Systems,” Sov. J. Exp. Theor. Phys. **34**(3), 610 (1972).

5. J. M. kosterlitz and D. J. Thouless, “Ordering, metastability and phase transitions in two-dimensional systems,” J. Phys. C Solid State Phys. **6**(7), 1181–1203 (1973) [doi:10.1088/0022-3719/6/7/010].

6. C. Nayak et al., “Non-Abelian anyons and topological quantum computation,” Rev. Mod. Phys. **80**(3), 1083–1159 (2008) [doi:10.1103/RevModPhys.80.1083].

7. A.Yu. Kitaev, “Fault-tolerant quantum computation by anyons,” Ann. Phys. (N. Y). **303**, 2–30 (2002).

8. F. D. M. Haldane, “Model for a quantum hall effect without landau levels: Condensed-matter realization of the ‘parity anomaly,’” Phys. Rev. Lett. **61**(18), 2015–2018 (1988) [doi:10.1103/PhysRevLett.61.2015].

9. C. L. Kane and E. J. Mele, “Z2 topological order and the quantum spin hall effect,” Phys. Rev. Lett. **95**(14), 3–6 (2005) [doi:10.1103/PhysRevLett.95.146802].

10. C. L. Kane and E. J. Mele, “Quantum Spin hall effect in graphene,” Phys. Rev. Lett. **95**(22), 1–4 (2005) [doi:10.1103/PhysRevLett.95.226801].

11. B. A. Bernevig and S. C. Zhang, “Quantum spin hall effect,” Phys. Rev. Lett. **96**(10), 1–4 (2006) [doi:10.1103/PhysRevLett.96.106802].

12. B. A. Bernevig, T. L. Hughes, and S. Zhang, “Quantum Spin Hall Effect and Topological Phase Transition in HgTe Quantum Wells,” Science (80-.). **314**(5806), 1757–1761 (2006) [doi:10.1126/science.1133734].

13. M. König et al., “The quantum spin Hall effect: Theory and experiment,” J. Phys. Soc. Japan

77(3) (2008) [doi:10.1143/JPSJ.77.031007].

14. C. Brüne et al., “Spin polarization of the quantum spin Hall edge states,” Nat. Phys. **8**(6), 485–490, Nature Publishing Group (2012) [doi:10.1038/nphys2322].

15. L. Fu, C. L. Kane, and E. J. Mele, “Topological insulators in three dimensions,” Phys. Rev. Lett. **98**(10), 1–4 (2007) [doi:10.1103/PhysRevLett.98.106803].

16. M. Z. Hasan and C. L. Kane, “Colloquium: Topological insulators,” Rev. Mod. Phys. **82**(4), 3045–3067 (2010) [doi:10.1103/RevModPhys.82.3045].

17. H. Zhang et al., “Topological insulators in Bi 2 Se 3, Bi 2 Te 3 and Sb 2 Te 3 with a single Dirac cone on the surface,” Nat. Phys. **5**(6), 438–442, Nature Publishing Group (2009) [doi:10.1038/nphys1270].

18. C. Brüne et al., “Quantum Hall effect from the topological surface states of strained bulk HgTe,” Phys. Rev. Lett. **106**(12), 1–4 (2011) [doi:10.1103/PhysRevLett.106.126803].

19. M. Konig et al., “Quantum Spin Hall Insulator State in HgTe Quantum Wells,” Science (80-.). **318**(5851), 766–770 (2007) [doi:10.1126/science.1148047].

20. K. V. Klitzing, G. Dorda, and M. Pepper, “New Method for High-Accuracy Determination of the Fine-Structure Constant Based on Quantized Hall Resistance,” Phys. Rev. Lett. **45**(6), 494–497 (1980) [doi:10.1103/PhysRevLett.45.494].

21. S. Murakami, N. Nagaosa, and S. C. Zhang, “Spin-Hall insulator,” Phys. Rev. Lett. **93**(15), 6–9 (2004) [doi:10.1103/PhysRevLett.93.156804].

22. I. Knez, R. R. Du, and G. Sullivan, “Evidence for helical edge modes in inverted InAs/GaSb quantum wells,” Phys. Rev. Lett. **107**(13), 1–5 (2011) [doi:10.1103/PhysRevLett.107.136603].

23. P. Leubner et al., “Strain Engineering of the Band Gap of HgTe Quantum Wells Using Superlattice Virtual Substrates,” Phys. Rev. Lett. **117**(8), 1–5 (2016) [doi:10.1103/PhysRevLett.117.086403].

24. S. Wu et al., “Observation of the quantum spin Hall effect up to 100 kelvin in a monolayer crystal,” Science (80-.). **359**(6371), 76–79 (2018) [doi:10.1126/science.aan6003].

25. N. Katsuragawa et al., “Room-temperature quantum spin Hall phase in laser-patterned few-layer 1T′- MoS2,” Commun. Mater. **1**(1), 4–6, Springer US (2020) [doi:10.1038/s43246-020-00050-w].

26. M. Marcinkiewicz et al., “Temperature-driven single-valley Dirac fermions in HgTe quantum wells,” Phys. Rev. B **96**(3), 8–11 (2017) [doi:10.1103/PhysRevB.96.035405].

27. C. Liu et al., “Quantum spin hall effect in inverted type-II semiconductors,” Phys. Rev. Lett. **100**(23), 1–4 (2008) [doi:10.1103/PhysRevLett.100.236601].

28. Y. Naveh and B. Laikhtman, “Band-structure tailoring by electric field in a weakly coupled electron-hole system,” Appl. Phys. Lett. **66**(15), 1980–1982 (1995) [doi:10.1063/1.113297].

29. M. J. Yang et al., “Evidence of a Hybridization Gap in ‘Semimetallic’ InAs/GaSb Systems,” Phys. Rev. Lett. **78**(24), 4613–4616 (1997) [doi:10.1103/PhysRevLett.78.4613].

30. L. L. Chang and L. Esaki, “Electronic properties of InAs GaSb superlattices,” Surf. Sci. **98**(1–3), 70–89 (1980) [doi:10.1016/0039-6028(80)90477-X].

31. M. Altarelli, “Electronic structure and semiconductor-semimetal transition in InAs-GaSb superlattices,” Phys. Rev. B **28**(2), 842–845 (1983) [doi:10.1103/PhysRevB.28.842].

32. M. Lakrimi et al., “Minigaps and novel giant negative magnetoresistance in Inas/Gasb semimetallic superlattices,” Phys. Rev. Lett. **79**(16), 3034–3037 (1997) [doi:10.1103/PhysRevLett.79.3034].

33. L. Du et al., “Robust helical edge transport in gated InAs/GaSb bilayers,” Phys. Rev. Lett. **114**(9), 1–5 (2015) [doi:10.1103/PhysRevLett.114.096802].

34. I. Knez, R. R. Du, and G. Sullivan, “Finite conductivity in mesoscopic Hall bars of inverted InAs/GaSb quantum wells,” Phys. Rev. B - Condens. Matter Mater. Phys. **81**(20), 5–8 (2010) [doi:10.1103/PhysRevB.81.201301].

35. Y. Naveh and B. Laikhtman, “Magnetotransport of coupled electron-holes,” Europhys. Lett. **55**(4), 545–551 (2001) [doi:10.1209/epl/i2001-00450-8].

36. B. Zhou et al., “Finite Size Effects on Helical Edge States in a Quantum Spin-Hall System,” Phys. Rev. Lett. **101**(24), 246807 (2008) [doi:10.1103/PhysRevLett.101.246807].

37. K. Suzuki et al., “Edge channel transport in the InAs/GaSb topological insulating phase,” Phys. Rev. B - Condens. Matter Mater. Phys. **87**(23), 1–6 (2013) [doi:10.1103/PhysRevB.87.235311].

38. C. Charpentier et al., “Suppression of bulk conductivity in InAs/GaSb broken gap composite quantum wells,” Appl. Phys. Lett. **103**(11), 28–31 (2013) [doi:10.1063/1.4821037].

39. I. Knez et al., “Observation of edge transport in the disordered regime of topologically insulating InAs / GaSb quantum wells,” Phys. Rev. Lett. **112**(2), 18–22 (2014) [doi:10.1103/PhysRevLett.112.026602].

40. T. Akiho et al., “Engineering quantum spin Hall insulators by strained-layer heterostructures,”

Appl. Phys. Lett. **109**(19), 192105 (2016) [doi:10.1063/1.4967471].

41. L. Du et al., “Tuning Edge States in Strained-Layer InAs/GaInSb Quantum Spin Hall Insulators,” Phys. Rev. Lett. **119**(5), 1–6 (2017) [doi:10.1103/PhysRevLett.119.056803].

42. S. S. Krishtopenko and F. Teppe, “Quantum spin Hall insulator with a large bandgap, Dirac fermions, and bilayer graphene analog,” Sci. Adv. **4**(4), eaap7529 (2018) [doi:10.1126/sciadv.aap7529].

43. S. Murakami et al., “Tuning phase transition between quantum spin Hall and ordinary insulating phases,” Phys. Rev. B - Condens. Matter Mater. Phys. **76**(20), 1–6 (2007) [doi:10.1103/PhysRevB.76.205304].

44. I. Vurgaftman, J. R. Meyer, and L. R. Ram-Mohan, “Band parameters for III-V compound semiconductors and their alloys,” J. Appl. Phys. **89**(11 I), 5815–5875 (2001) [doi:10.1063/1.1368156].

45. S. S. Krishtopenko, W. Knap, and F. Teppe, “Phase transitions in two tunnel-coupled HgTe quantum wells: Bilayer graphene analogy and beyond,” Sci. Rep. **6**(May), 30755, Nature Publishing Group (2016) [doi:10.1038/srep30755].

46. S. S. Krishtopenko et al., “Pressure- and temperature-driven phase transitions in HgTe quantum wells,” Phys. Rev. B **94**(24), 245402 (2016) [doi:10.1103/PhysRevB.94.245402].

47. S. S. Krishtopenko et al., “Cyclotron resonance of dirac fermions in InAs/GaSb/InAs quantum wells,” Semiconductors **51**(1), 38–42 (2017) [doi:10.1134/S1063782617010109].

48. S. Ruffenach et al., “Magnetoabsorption of Dirac Fermions in InAs/GaSb/InAs ‘Three-Layer’ Gapless Quantum Wells,” JETP Lett. **106**(11), 727–732 (2017) [doi:10.1134/S0021364017230102].

49. S. S. KRISHTOPENKO et al., “Temperature-dependent terahertz spectroscopy of inverted-band three-layer InAs/GaSb/InAs quantum well,” Phys. Rev. B **97**(24), 1–8, American Physical Society (2018) [doi:10.1103/PhysRevB.97.245419].

50. M. Orlita et al., “Fine structure of zero-mode Landau levels in HgTe/HgxCd 1-xTe quantum wells,” Phys. Rev. B - Condens. Matter Mater. Phys. **83**(11), 4–7 (2011) [doi:10.1103/PhysRevB.83.115307].

51. M. Zholudev et al., “Magnetospectroscopy of two-dimensional HgTe-based topological insulators around the critical thickness,” Phys. Rev. B **86**(20), 205420 (2012) [doi:10.1103/PhysRevB.86.205420].

52. S. S. Krishtopenko et al., “Effect of electron-electron interaction on cyclotron resonance in high-mobility InAs/AlSb quantum wells,” J. Appl. Phys. **117**(11), 112813 (2015) [doi:10.1063/1.4913927].

53. A. V. Ikonnikov et al., “Temperature-dependent magnetospectroscopy of HgTe quantum wells,” Phys. Rev. B **94**(15), 2–7 (2016) [doi:10.1103/PhysRevB.94.155421].

54. B. A. Assaf et al., “Massive and massless Dirac fermions in Pb1−xSnxTe topological crystalline insulator probed by magneto-optical absorption,” Sci. Rep. **6**(1), 20323, Nature Publishing Group (2016) [doi:10.1038/srep20323].

55. S. B. Zhang, Y. Y. Zhang, and S. Q. Shen, “Robustness of quantum spin Hall effect in an external magnetic field,” Phys. Rev. B - Condens. Matter Mater. Phys. **90**(11), 1–8 (2014) [doi:10.1103/PhysRevB.90.115305].

56. Y. Jiang et al., “Probing the semiconductor to semimetal transition in InAs/GaSb double quantum wells by magneto-infrared spectroscopy,” Phys. Rev. B **95**(4), 1–6 (2017) [doi:10.1103/PhysRevB.95.045116].

57. A. M. Kadykov et al., “Temperature-Induced Topological Phase Transition in HgTe Quantum Wells,” Phys. Rev. Lett. **120**(8), 86401, American Physical Society (2018) [doi:10.1103/PhysRevLett.120.086401].

58. R. Winkler et al., “Theory for the cyclotron resonance of holes in strained asymmetric Ge-SiGe quantum wells,” Phys. Rev. B - Condens. Matter Mater. Phys. **53**(16), 10858–10865 (1996) [doi:10.1103/PhysRevB.53.10858].

59. А. М. Кадыков, “Фотоотклик и стимулированное излучение в структурах на основе соединений HgCdTe в среднем и дальнем ИК диапазонах.”

60. M. S. Zholudev et al., “Anticrossing of Landau levels in HgTe/CdHgTe (013) quantum wells with an inverted band structure,” JETP Lett. **100**(12), 790–794 (2015) [doi:10.1134/S0021364014240175].

61. S. S. Krishtopenko et al., “Many-particle effects in optical transitions from zero-mode Landau levels in HgTe quantum wells,” Phys. Rev. B **102**(4), 41404, American Physical Society (2020) [doi:10.1103/physrevb.102.041404].

62. J. Shao et al., “Modulated photoluminescence spectroscopy with a step-scan Fourier transform infrared spectrometer,” Rev. Sci. Instrum. **77**(6) (2006) [doi:10.1063/1.2205622].

63. S. V. Morozov et al., “Efficient long wavelength interband photoluminescence from HgCdTe

epitaxial films at wavelengths up to 26 μ m," Appl. Phys. Lett. **104**(7), 072102 (2014) [doi:10.1063/1.4866006].

64. S. V Morozov et al., "Time resolved photoluminescence spectroscopy of narrow gap Hg1− xCdxTe/CdyHg1− yTe quantum well heterostructures," Appl. Phys. Lett. **105**(2), 22102 (2014).

65. V. V Rumyantsev et al., "Specific features of the spectra and relaxation kinetics of long-wavelength photoconductivity in narrow-gap HgCdTe epitaxial films and heterostructures with quantum wells," Semiconductors **47**(11), 1438–1441 (2013).

66. C. C. Ling et al., "Nature of the acceptor responsible for p-type conduction in liquid encapsulated Czochralski-grown undoped gallium antimonide," Appl. Phys. Lett. **85**(3), 384–386 (2004) [doi:10.1063/1.1773934].

67. N. Segercrantz et al., "Point defect balance in epitaxial GaSb," Appl. Phys. Lett. **105**(8) (2014) [doi:10.1063/1.4894473].

68. S. S. Krishtopenko et al., "Terahertz Spectroscopy of Two-Dimensional Semimetal in Three-Layer InAs/GaSb/InAs Quantum Well," JETP Lett. **109**(2), 96–101 (2019) [doi:10.1134/S0021364019020085].

69. T. Ohta et al., "Controlling the electronic structure of bilayer graphene," Science (80-.). **313**(5789), 951–954 (2006) [doi:10.1126/science.1130681].

70. M. Yankowitz et al., "Band structure mapping of bilayer graphene via quasiparticle scattering," APL Mater. **2**(9) (2014) [doi:10.1063/1.4890543].

71. P. Michetti et al., "Tunable quantum spin Hall effect in double quantum wells," Phys. Rev. B - Condens. Matter Mater. Phys. **85**(12), 1–8 (2012) [doi:10.1103/PhysRevB.85.125309].

72. P. Michetti and B. Trauzettel, "Devices with electrically tunable topological insulating phases," Appl. Phys. Lett. **102**(6) (2013) [doi:10.1063/1.4792275].

73. J. C. Budich, B. Trauzettel, and P. Michetti, "Time reversal symmetric topological exciton condensate in bilayer HgTe quantum wells," Phys. Rev. Lett. **112**(14), 1–5 (2014) [doi:10.1103/PhysRevLett.112.146405].

74. A. V. Ikonnikov et al., "Cyclotron resonance and interband optical transitions in HgTe/CdTe(0 1 3) quantum well heterostructures," Semicond. Sci. Technol. **26**(12), 125011 (2011) [doi:10.1088/0268-1242/26/12/125011].

75. E. G. Novik et al., "Band structure of semimagnetic Hg1-yMnyTe quantum wells," Phys. Rev. B -

Condens. Matter Mater. Phys. **72**(3) (2005) [doi:10.1103/PhysRevB.72.035321].

76. F. Schindler et al., "Higher-order topological insulators," 1–8 (2018).

77. S. Dvoretsky et al., "Growth of HgTe quantum wells for IR to THz detectors," J. Electron. Mater. **39**(7), 918–923 (2010).

78. L. S. Bovkun et al., "Magnetospectroscopy of double HgTe/CdHgTe QWs with inverted band structure in high magnetic fields up to 30 T," Opto-Electronics Rev. **27**(2), 213–218, Association of Polish Electrical Engineers (SEP) (2019) [doi:10.1016/j.opelre.2019.06.001].

79. S. Kasap and A. Willoughby, *Mercury Cadmium Telluride: Growth, Properties and Applications*, John Wiley & Sons (2011).

80. J. P. Laurenti et al., "Temperature dependence of the fundamental absorption edge of mercury cadmium telluride," J. Appl. Phys. **67**(10), 6454–6460 (1990) [doi:10.1063/1.345119].

81. D. B. Topalović et al., "Asymmetric versus symmetric HgTe / Cd x Hg 1 - X Te double quantum wells: Bandgap tuning without electric field," J. Appl. Phys. **128**(6), AIP Publishing LLC (2020) [doi:10.1063/5.0016069].

82. A. Rogalski, "HgCdTe infrared detector material: History, status and outlook," Reports Prog. Phys. **68**(10), 2267–2336 (2005) [doi:10.1088/0034-4885/68/10/R01].

83. I. Vurgaftman and J. Meyer, "High-temperature HgTe/CdTe multiple-quantum-well lasers," Opt. Express **2**(4), 137 (1998) [doi:10.1364/OE.2.000137].

84. Y. Jiang, M. C. Teich, and W. I. Wang, "Carrier lifetimes and threshold currents in HgCdTe double heterostructure and multi-quantum-well lasers," J. Appl. Phys. **69**(10), 6869–6875 (1991) [doi:10.1063/1.347676].

85. S. V. Morozov et al., "Long wavelength stimulated emission up to 9.5 μ m from HgCdTe quantum well heterostructures," Appl. Phys. Lett. **108**(9), 092104 (2016) [doi:10.1063/1.4943087].

86. K. Ohtani et al., "Far-Infrared Quantum Cascade Lasers Operating in the AlAs Phonon Reststrahlen Band," ACS Photonics **3**(12), 2280–2284 (2016) [doi:10.1021/acsphotonics.6b00750].

87. M. Bahriz et al., "High temperature operation of far infrared (λ ≈20 μm) InAs/AlSb quantum cascade lasers with dielectric waveguide," Opt. Express **23**(2), 1523 (2015) [doi:10.1364/oe.23.001523].

88. W. Terashima and H. Hirayama, “GaN-based terahertz quantum cascade lasers,” Terahertz Physics, Devices, Syst. IX Adv. Appl. Ind. Def. **9483**(May 2015), 948304 (2015) [doi:10.1117/12.2184199].

89. D. N. Talwar and M. Vandevyver, “Vibrational properties of HgCdTe system,” J. Appl. Phys. **56**(6), 1601–1607 (1984) [doi:10.1063/1.334144].

90. M. S. Vitiello et al., “Quantum cascade lasers: 20 years of challenges,” Opt. Express **23**(4), 5167 (2015) [doi:10.1364/oe.23.005167].

91. B. S. Williams, “Terahertz quantum-cascade lasers,” Nat. Photonics **1**(9), 517–525 (2007) [doi:10.1038/nphoton.2007.166].

92. Q. Y. Lu et al., “Widely tunable room temperature semiconductor terahertz source,” Appl. Phys. Lett. **105**(20) (2014) [doi:10.1063/1.4902245].

93. K. Ohtani, M. Beck, and J. Faist, “Double metal waveguide InGaAs/AlInAs quantum cascade lasers emitting at 24 μ m,” Appl. Phys. Lett. **105**(12), 2–6 (2014) [doi:10.1063/1.4896542].

94. R. Colombelli et al., “Far-infrared surface-plasmon quantum-cascade lasers at 21.5 μm and 24 μm wavelengths,” Appl. Phys. Lett. **78**(18), 2620–2622 (2001) [doi:10.1063/1.1367304].

95. J. Ulrich et al., “Long wavelength (15 and 23 μm) GaAs/AlGaAs quantum cascade lasers,” Appl. Phys. Lett. **80**(20), 3691–3693 (2002) [doi:10.1063/1.1481236].

96. К. В. Маремьянин et al., “Терагерцовые инжекционные лазеры на основе твердого раствора PbSnSe с длиной волны излучения до 50 мкм и их использование для магнитоспектроскопии полупроводников,” Журнал технической физики **52**(12), 1486 (2018) [doi:10.21883/FTP.2018.12.46762.42].

97. L. Kurbatov et al., “Far-IR heterojunction lasers tunable to 46.2 microns,” in Soviet Journal of Experimental and Theoretical Physics Letters **37**, pp. 422–424 (1983).

98. V. S. Varavin et al., “HgCdTe epilayers on GaAs: growth and devices,” in Proceedings of SPIE - The International Society for Optical Engineering(March 2014), J. Rutkowski and A. Rogalski, Eds., pp. 381–395 (2003) [doi:10.1117/12.519761].

99. A. A. Andronov et al., “Stimulated emission from optically excited Cd xHg 1-xTe structures at room temperature,” J. Lumin. **132**(3), 612–616, Elsevier (2012) [doi:10.1016/j.jlumin.2011.09.019].

100. J. M. Arias et al., “HgCdTe infrared diode lasers grown by MBE,” Semicond. Sci. Technol. **8**(1S),

S255 (1993) [doi:10.1088/0268-1242/8/1S/056].

101. C. Roux, E. Hadji, and J.-L. Pautrat, “2.6 μm optically pumped vertical-cavity surface-emitting laser in the CdHgTe system,” Appl. Phys. Lett. **75**(24), 3763–3765 (1999) [doi:10.1063/1.125448].

102. C. Roux, E. Hadji, and J.-L. Pautrat, “Room-temperature optically pumped CdHgTe vertical-cavity surface-emitting laser for the 1.5 μm range,” Appl. Phys. Lett. **75**(12), 1661–1663 (1999) [doi:10.1063/1.124831].

103. J. Bonnet-Gamard et al., “Optical gain and laser emission in HgCdTe heterostructures,” J. Appl. Phys. **78**(12), 6908–6915 (1995) [doi:10.1063/1.360457].

104. M. Zandian et al., “HgCdTe double heterostructure injection laser grown by molecular beam epitaxy,” Appl. Phys. Lett. **59**(9), 1022–1024 (1991) [doi:10.1063/1.106332].

105. E. Hadji et al., “Photopumped infrared vertical-cavity surface-emitting laser,” Appl. Phys. Lett. **68**(18), 2480–2482 (1996).

106. E. Hadji et al., “3.2 μm infrared resonant cavity light emitting diode,” Appl. Phys. Lett. **67**(18), 2591–2593 (1995) [doi:10.1063/1.115141].

107. J. Bleuse et al., “Laser emission in HgCdTe in the 2–3.5 μm range,” J. Cryst. Growth **197**(3), 529–536 (1999).

108. A. Ravid et al., “Optically pumped laser oscillation at #2.9 μm of a HgCdTe layer grown by metalorganic chemical vapor deposition,” Appl. Phys. Lett. **55**(26), 2704–2706 (1989) [doi:10.1063/1.101930].

109. J. P. Zanatta et al., “HgCdTe molecular beam epitaxy material for microcavity light emitters: Application to gas detection in the 2–6 μm range,” J. Electron. Mater. **32**(7), 602–607 (2003).

110. H. Q. Le et al., “High-power diode-laser-pumped midwave infrared HgCdTe/CdZnTe quantum-well lasers,” Appl. Phys. Lett. **65**(7), 810–812 (1994) [doi:10.1063/1.112239].

111. J. O. Dimmock, I. Melngailis, and A. J. Strauss, “Band structure and laser action in Pb x Sn 1− x Te,” Phys. Rev. Lett. **16**(26), 1193 (1966).

112. К. Д. Мынбаев et al., “Фотолюминесценция гетероструктур на основе Hg1−xCdxTe , выращенных методом молекулярно-лучевой эпитаксии,” Физика И Техника Полупроводников **45**(7), 900–907 (2011).

113. В. В. Румянцев et al., “Релаксация носителей заряда в узкозонных эпитаксиальных слоях

HgCdTe и структурах с квантовыми ямами на основе HgTe/HgCdTe," in Нанофизика и наноэлектроника, pp. 749–750 (2018).

114. S. Ruffenach et al., "HgCdTe-based heterostructures for terahertz photonics," APL Mater. **5**(3), 035503 (2017) [doi:10.1063/1.4977781].

115. M. S. Zholudev et al., "Cyclotron resonance in HgTe/CdTe-based heterostructures in high magnetic fields," Nanoscale Res. Lett. **7**(1), 1–7 (2012) [doi:10.1186/1556-276X-7-534].

116. S. A. Tarasenko et al., "Split Dirac cones in HgTe/CdTe quantum wells due to symmetry-enforced level anticrossing at interfaces," Phys. Rev. B - Condens. Matter Mater. Phys. **91**(8) (2015) [doi:10.1103/PhysRevB.91.081302].

117. G. M. Minkov et al., "Valence band energy spectrum of HgTe quantum wells with an inverted band structure," Phys. Rev. B **96**(3), 1–8 (2017) [doi:10.1103/PhysRevB.96.035310].

118. S. Krishnamurthy, M. A. Berding, and Z. G. Yu, "Minority carrier lifetimes in HgCdTe alloys," J. Electron. Mater. **35**(6), 1369–1378 (2006) [doi:10.1007/s11664-006-0270-2].

119. K. Jóźwikowski, M. Kopytko, and A. Rogalski, "The bulk generation-recombination processes and the carrier lifetime in mid-wave infrared and long-wave infrared liquid nitrogen cooled HgCdTe alloys," J. Appl. Phys. **112**(3), 033718 (2012) [doi:10.1063/1.4745872].

120. S. V. Morozov et al., "Investigation of possibility of VLWIR lasing in HgCdTe based heterostructures," J. Phys. Conf. Ser. **647**(1), 2–6 (2015) [doi:10.1088/1742-6596/647/1/012008].

121. S. V. Morozov et al., "Long wavelength superluminescence from narrow gap HgCdTe epilayer at 100 K," Appl. Phys. Lett. **107**(4), 042105 (2015) [doi:10.1063/1.4926927].

122. A. S. Polkovnikov and G. G. Zegrya, "Auger recombination in semiconductor quantum wells," Phys. Rev. B **58**(7), 4039–4056 (1998) [doi:10.1103/PhysRevB.58.4039].

123. V. V. Rumyantsev et al., "Investigation of HgCdTe waveguide structures with quantum wells for long-wavelength stimulated emission," Semiconductors **51**(12), 1557–1561 (2017) [doi:10.1134/S106378261712017X].

124. M. A. Fadeev et al., "Effect of Cd content in barriers on the threshold energy of Auger recombination in waveguide structures with HgTe/Cd x Hg 1-x Te quantum wells, emitting at a wavelength of 18 μm," Quantum Electron. **49**(6), 556–558, {IOP} Publishing (2019) [doi:10.1070/QEL17034].

125. V. Y. Aleshkin et al., “Threshold energies of Auger recombination in HgTe/CdHgTe quantum well heterostructures with 30–70 meV bandgap,” J. Phys. Condens. Matter **31**(42), 425301, IOP Publishing (2019) [doi:10.1088/1361-648x/ab301a].

126. V. V. Utochkin et al., “Study of the Auger Recombination Energy Threshold in a Series of Waveguide Heterostructures with HgTe/Cd0.7Hg0.3Te QWs Near 14 μm,” Semiconductors **53**(9), 1154–1157 (2019) [doi:10.1134/S1063782619090264].

127. V. V. Rumyantsev et al., “Effect of Features of the Band Spectrum on the Characteristics of Stimulated Emission in Narrow-Gap Heterostructures with HgCdTe Quantum Wells,” Semiconductors **52**(11), 1375–1379 (2018) [doi:10.1134/S1063782618110234].

128. V. Rumyantsev et al., “Terahertz Emission from HgCdTe QWs under Long-Wavelength Optical Pumping,” J. Infrared, Millimeter, Terahertz Waves **41**(7), 750–757, Journal of Infrared, Millimeter, and Terahertz Waves (2020) [doi:10.1007/s10762-020-00706-1].